

**Experimental Investigation and Analytical Modeling of
Solid-Particle Erosion Behavior of Stellite Alloys**

by

Sydney Nsoesie

**A thesis submitted to the Faculty of Graduate and Postdoctoral
Affairs in partial fulfillment of the requirements for the degree of**

Master of Applied Science

in

Mechanical Engineering

**Carleton University
Ottawa, Ontario**

© 2013, Sydney Nsoesie



Library and Archives
Canada

Published Heritage
Branch

395 Wellington Street
Ottawa ON K1A 0N4
Canada

Bibliothèque et
Archives Canada

Direction du
Patrimoine de l'édition

395, rue Wellington
Ottawa ON K1A 0N4
Canada

Your file Votre référence

ISBN: 978-0-494-94647-3

Our file Notre référence

ISBN: 978-0-494-94647-3

NOTICE:

The author has granted a non-exclusive license allowing Library and Archives Canada to reproduce, publish, archive, preserve, conserve, communicate to the public by telecommunication or on the Internet, loan, distribute and sell theses worldwide, for commercial or non-commercial purposes, in microform, paper, electronic and/or any other formats.

The author retains copyright ownership and moral rights in this thesis. Neither the thesis nor substantial extracts from it may be printed or otherwise reproduced without the author's permission.

AVIS:

L'auteur a accordé une licence non exclusive permettant à la Bibliothèque et Archives Canada de reproduire, publier, archiver, sauvegarder, conserver, transmettre au public par télécommunication ou par l'Internet, prêter, distribuer et vendre des thèses partout dans le monde, à des fins commerciales ou autres, sur support microforme, papier, électronique et/ou autres formats.

L'auteur conserve la propriété du droit d'auteur et des droits moraux qui protègent cette thèse. Ni la thèse ni des extraits substantiels de celle-ci ne doivent être imprimés ou autrement reproduits sans son autorisation.

In compliance with the Canadian Privacy Act some supporting forms may have been removed from this thesis.

While these forms may be included in the document page count, their removal does not represent any loss of content from the thesis.

Conformément à la loi canadienne sur la protection de la vie privée, quelques formulaires secondaires ont été enlevés de cette thèse.

Bien que ces formulaires aient inclus dans la pagination, il n'y aura aucun contenu manquant.

Canada

Abstract

Stellite alloys are a range of cobalt-chromium alloys, also containing tungsten or molybdenum and a small amount (< 3 wt%) of carbon. These alloys are designed mainly for severe corrosion, wear and erosion environments. In this research a group of Stellite alloys that are commonly employed or potentially materials for erosion resistance application are studied under solid-particle erosion test. Two particle impact velocities (84 m/s and 98 m/s) and two impingement angles (30 degree and 90 degree) are used in the test. It is demonstrated that Stellite alloys are more resistant to erosion at 90 degree impingement angle than at 30 degree impingement angle and the erosion damage of Stellite alloys increases with the particle impact velocity. The erosion resistance of Stellite alloys is controlled mainly by their carbon content, but the tungsten and molybdenum contents also play an important role, because these elements determine the volume fractions of carbides and intermetallics in Stellite alloys. The eroded surfaces are analyzed using SEM to further understand the erosion test results. An erosion model, originally developed by Sheldon and Kanhere (1972), known as S-K model, has been modified for use on Stellite alloys, with the support of experimental data. The significant contribution of this modification is that the effect of particle impingement angle has been included. With this modified S-K model, for a Stellite alloy that has a similar chemical composition to one of the alloys studied in this research, the erosion rate for a set particle impact velocity at an impingement angle between 30 degree and 90 degree can be estimated. This modified S-K model can be used for erosion characterization of existing Stellite alloys and in the designing of new Stellite alloys for erosion resistance application.

Acknowledgements

It is with great pleasure to take this opportunity to thank the many people who made this thesis possible.

First, I would like to thank my supervisor, Professor Rong Liu, for her guidance during my research and study at Carleton University. Her patience, flexibility and guidance have allowed me to complete my research successfully and on time. In addition, she was always accessible and willing to provide input.

As well, I would like to thank the many people at NRC specifically Dr. Kuiying Chen, Olga Lupandina, Dr. Qi Yang and David Chow. I appreciate their assistance in providing me with the instruments and technical experience during my experiments at NRC.

I would also like to thank Dr. Jianqun Wang of the Science Department at Carleton University for taking the time to lecture me on various microstructure analysis techniques. His help has enabled me to better understand and advance in my research accordingly.

In addition, I would like to thank Kennametal Stellite Inc. in Belleville for various supports. Dr. Matthew Yao and Rachael Collier provided significant assistance in getting my test specimens ready on time. They were also very helpful in guiding me to better understand Stellite alloys in the microstructure analysis stage. I greatly appreciate their help.

Lastly, I would like to thank both my family and Linda for their support and motivation.

Table of Contents

Abstract	i
Acknowledgements	ii
Table of Contents	iii
List of Tables	vii
List of Figures	ix
1 Chapter: Introduction	1
1.1 Background of Present Research.....	1
1.1.1 Fundamentals of Stellite alloys.....	1
1.1.2 Application of Stellite alloys	2
1.2 Introduction of Present Research	4
1.2.1 Significance and objectives	4
1.2.2 Tasks and methodologies.....	6
1.3 Organization of the Thesis	8
2 Chapter: Literature Review	11
2.1 Erosion of Materials.....	11
2.1.1 Definition of erosion.....	11
2.1.2 Solid-particle erosion.....	12
2.2 Parameters of Erosion	13
2.2.1 Impingement/impact angle	13
2.2.2 Erodent particle impact velocity	15
2.2.3 Erodent particle size.....	16
2.2.4 Erodent particle shape, hardness and particle flow rate.....	17
2.2.5 Target material	18
2.3 Methodologies of Erosion Research	19

2.3.1	Experimental investigation	19
2.3.2	Analytical modeling.....	25
2.4	Erosion of Stellite Alloys.....	36
2.4.1	Microstructure of Stellite alloys	36
2.4.2	Previous research in erosion of Stellite alloys	39
3	Chapter: Microstructural Characterization	42
3.1	Test Specimens.....	42
3.1.1	Alloy selection	42
3.1.2	Chemical compositions.....	44
3.2	Microstructural Analysis.....	45
3.2.1	Specimen preparation	45
3.2.2	Microstructure examination.....	50
3.2.3	SEM images of microstructure	51
4	Chapter: Erosion Test.....	74
4.1	Experimental Preparation.....	74
4.1.1	Testing specimens.....	74
4.1.2	Testing facilities.....	76
4.2	Experimental Procedures	81
4.2.1	Test parameters.....	81
4.2.2	Test steps	82
4.3	Experimental Results	89
4.3.1	Sand flow rate	89
4.3.2	Erosion rate.....	89
4.3.3	Comparison of erosion rates	94
4.3.4	Erosion rate expression in volume loss.....	98
4.4	Eroded Surface Analysis.....	99

4.4.1	Erosion at 30 degree impingement angle.....	99
4.4.2	Erosion at 90 degree impingement angle.....	106
5	Chapter: Analytical Modeling of Erosion	112
5.1	Model Development Details	112
5.1.1	Background of model development.....	112
5.1.2	S-K model concepts.....	113
5.1.3	Original S-K model formulation.....	115
5.2	Implementation of S-K Model	119
5.2.1	Test of S-K model.....	119
5.2.2	Verification of S-K model	120
5.3	Modification of the S-K Model.....	124
5.3.1	Statistical formulation.....	124
5.3.2	Determination of constants	126
6	Chapter: Discussion on Results and Correlations	129
6.1	Chemical Composition.....	129
6.1.1	Effects on microstructure.....	129
6.1.2	Relationship between microstructure and hardness.....	130
6.2	Correlations of Experimental Results	131
6.2.1	Erosion resistance versus microstructure.....	131
6.2.2	Erosion resistance versus hardness	134
6.3	Modeling of Erosion	135
6.3.1	Error analysis of the modified S-K model	135
6.3.2	Prediction of erosion rate.....	137
6.3.3	Experimental errors.....	139
7	Chapter: Conclusions and Further Work	141
7.1	Conclusions.....	141

7.2	Future Work.....	144
	References	145
	Appendix: Experimental Data Sheets	151

List of Tables

Table 2-1: Examples of components subjected to solid particle erosion [15]	13
Table 2-2: Particles and target materials in the erosion test of Oka <i>et al.</i> [8].....	20
Table 3-1: Chemical compositions (wt%, Co in balance) of Stellite alloys	45
Table 3-2: Metallic element table of location 1 for alloy A	59
Table 3-3: Metallic element table of location 2 for alloy A	60
Table 3-4: Metallic element table of location 1 for alloy B.....	62
Table 3-5: Metallic element table of location 2 for alloy B.....	63
Table 3-6: Metallic element table of location 3 for alloy B.....	64
Table 3-7: Metallic element table of location 1 for alloy C.....	66
Table 3-8: Metallic element table of location 2 for alloy C.....	67
Table 3-9: Metallic element table of location 1 for alloy D	69
Table 3-10: Metallic element table of location 2 for alloy D	70
Table 3-11: Metallic element table of location 1 for alloy E.....	72
Table 3-12: Metallic element table of location 2 for alloy E.....	73
Table 4-1: Erosion test process parameters	81
Table 4-2: Erosion test condition parameters	82
Table 4-3: Average erosion rates, ER ($\mu\text{g/g}$), at sand velocity of 84 (m/s).....	91
Table 4-4: Average erosion rates, ER ($\mu\text{g/g}$), at sand velocity of 98 (m/s).....	91
Table 4-5: Target material densities (kg/m^3)	98
Table 4-6: Erosion rates, ER expressed in volume loss, (m^3/g) $\times 10^{-11}$	98
Table 5-1: Summary of particle velocity exponents and diameter exponents [6]	114
Table 5-2: Properties of erodent particles [6].	114

Table 5-3: Predicted erosion rates by the S-K model	120
Table 5-4: Experimental erosion rates, ER, (kg/g) × 10 ⁻⁹	120
Table 5-5: Experimental erosion rates in volume loss, ER, (m ³ /g) × 10 ⁻¹¹	121
Table 5-6: Predicted erosion rates from S-K model after applying	122
Table 5-7: Values of constants and predicted erosion rates from the modified model...	128
Table 6-1: Hardness values of Stellite alloys.....	131
Table 6-2: Error analysis for the modified S-K model	137
Table A- 1: Test data at 84 m/s sand velocity for alloy A	151
Table A- 2: Test data at 98 m/s sand velocity for alloy A	152
Table A- 3: Test data at 84 m/s sand velocity for alloy B	153
Table A- 4: Test data at 98 m/s sand velocity for alloy B	154
Table A- 5: Test data at 84 m/s sand velocity for alloy C	155
Table A- 6: Test data at 98 m/s sand velocity for alloy C	156
Table A- 7: Test data at 84 m/s sand velocity for alloy D.....	157
Table A- 8: Test data at 98 m/s sand velocity for alloy D	158
Table A- 9: Test data at 84 m/s sand velocity for alloy E.....	159
Table A- 10: Test data at 98 m/s sand velocity for alloy E.....	160

List of Figures

Figure 2-1: Schematic diagram depicting the impingement/impact angle [8].....	13
Figure 2-2: Schematic diagram showing the influence of impact angle on erosion rate in the case of ductile and brittle materials [7].....	14
Figure 2-3: Variation of erosion rate of steel with particle size at different impact velocities [15].....	16
Figure 2-4: Effects of particle shape on erosion rate [15].	18
Figure 2-5: Schematic diagram of a sand blast type erosion test rig [8].....	21
Figure 2-6: Impact-angle dependence of normalized erosion using silicon carbide particles of 254 μm at 100 m/s [8].....	22
Figure 2-7: Steady-state erosion rate as a function of impact angle for (a) AC4C matrix alloy, (b) AC4C Al- $\text{Al}_{18}\text{B}_4\text{O}_3$ whisker composites [24].	24
Figure 2-8: The concept of erosion arising from repeated plastic deformation and cutting action [34].	32
Figure 2-9: SEM microstructure of Stellite 3.	38
Figure 2-10: SEM microstructure of Stellite 6.	38
Figure 2-11: Erosion curves of Stellite alloys [40].....	40
Figure 3-1: Secotom-10 cutting machine (Courtesy of Struers Co.).	46
Figure 3-2: LaboPress-3 mounting press (Courtesy of Struers Co.).....	47
Figure 3-3: Buehler Ecomet-IV semi-automatic grinder polisher.	48
Figure 3-4: Apparatus setup with the Buehler Electromet etcher.....	49
Figure 3-5: Hitachi Model S-570 Scanning Electron Microscope (SEM) with energy dispersive X-ray (EDX) spectrum.	50

Figure 3-6: TESCAN Scanning Electron Microscope..... 51

Figure 3-7: SEM microstructure of alloy A: (a) at low magnification and (b) at high magnification. 52

Figure 3-8: SEM microstructure of alloy B: (a) at low magnification and (b) at high magnification. 53

Figure 3-9: SEM microstructure of alloy C: (a) at low magnification and (b) at high magnification. 54

Figure 3-10: SEM microstructure of alloy D: (a) at low magnification and (b) at high magnification. 55

Figure 3-11: SEM microstructure of alloy E: (a) at low magnification and (b) at high magnification. 56

Figure 3-12: SEM microstructure of alloy A with phases indicated for EDX analysis.... 58

Figure 3-13: EDX spectrum of location 1 for alloy A. 58

Figure 3-14: EDX spectrum of location 2 for alloy A. 59

Figure 3-15: SEM microstructure of alloy B with phases indicated for EDX analysis. 61

Figure 3-16: EDX spectrum of location 1 for alloy B. 61

Figure 3-17: EDX spectrum of location 2 for alloy B. 62

Figure 3-18: EDX spectrum of location 3 for alloy B. 63

Figure 3-19: SEM microstructure of alloy C with phases indicated for EDX analysis. 65

Figure 3-20: EDX spectrum of location 1 for alloy C. 65

Figure 3-21: EDX spectrum of location 2 for alloy C. 66

Figure 3-22: SEM microstructure of alloy D with phases indicated for EDX analysis.... 68

Figure 3-23: EDX spectrum of location 1 for alloy D. 68

Figure 3-24: EDX spectrum of location 2 for alloy D.	69
Figure 3-25: SEM microstructure of alloy E with phases indicated for EDX analysis. ...	71
Figure 3-26: EDX spectrum of location 1 for alloy E.	71
Figure 3-27: EDX spectrum of location 2 for alloy E.	72
Figure 4-1: Specimen geometry of alloy A.....	74
Figure 4-2: Specimen geometry of alloy B, alloy C, alloy D and alloy E.	74
Figure 4-3: Compressed air unit used for specimen cleaning.....	75
Figure 4-4: Entire apparatus assembly of erosion test:(a) inert environment (Compressed nitrogen gas); S.S. WHITE Airbrasive 6500 erosion chamber; and S.S. WHITE Airbrasive Micro-Blasting Jet Machine; (b) specimen and nozzle holder; and nozzle (Courtesy of S.S. WHITE Technologies Inc.).	77
Figure 4-5: Specimen holder with screw responsible for impingement angle adjustment (Courtesy of S.S. WHITE Technologies Inc.).	78
Figure 4-6: S.S. WHITE Airbrasive Micro-Blasting Jet Machine with two major knobs (Courtesy of S.S. WHITE Technologies Inc.).	78
Figure 4-7: Compressed nitrogen storage tank with shut-off valve and pressure regulator.	79
Figure 4-8: Erodent particles - Angular AccuBRADE-50 blend #3 alpha alumina powder: (a) SEM morphology and (b) supplied product (Courtesy of S.S. WHITE Technologies Inc.).	80
Figure 4-9: Sartorius scale balance for specimen mass measurement.	82
Figure 4-10: Marking used for specimen positioning; (a) on specimen and (b) on specimen holder.	84

Figure 4-11: Nozzle mounting at an impingement angle of 30 degree.....	85
Figure 4-12: Nozzle mounting at an impingement angle of 90 degree.....	86
Figure 4-13: S.S. WHITE Airbrasive Micro-Blasting Jet Machine containing aluminum oxide particles placed on a Sartorius scale balance in the erosion test.	87
Figure 4-14: Eroded specimen surface; (a) before cleaning and (b) after cleaning.....	88
Figure 4-15: Erosion rates ($\mu\text{g/g}$) at 84 m/s sand velocity and at 30 degree	92
Figure 4-16: Erosion rates ($\mu\text{g/g}$) at 84 m/s sand velocity and at 90 degree	92
Figure 4-17: Erosion rates ($\mu\text{g/g}$) at 98 m/s sand velocity and at 30 degree	93
Figure 4-18: Erosion rates ($\mu\text{g/g}$) at 98 m/s sand velocity and at 90 degree	93
Figure 4-19: Comparison of erosion rates for different impingement angles; (a) at 84 m/s sand velocity and (b) at 98 m/s sand velocity.	95
Figure 4-20: Comparison of erosion rates for different sand velocities; (a) at 30 degree impingement angle and (b) at 90 degree impingement angle.	97
Figure 4-21: SEM images of eroded surface of alloy A tested at 98 m/s sand velocity and 30 degree impingement angle: (a) at low magnification and (b) at high magnification.	101
Figure 4-22: SEM images of eroded surface of alloy B tested at 98 m/s sand velocity and 30 degree impingement angle: (a) at low magnification and (b) at high magnification.	102
Figure 4-23: SEM images of eroded surface of alloy C tested at 98 m/s sand velocity and 30 degree impingement angle: (a) at low magnification and (b) at high magnification.	103
Figure 4-24: SEM images of eroded surface of alloy D tested at 98 m/s sand velocity and 30 degree impingement angle: (a) at low magnification and (b) at high magnification.	104
Figure 4-25: SEM images of eroded surface of alloy E tested at 98 m/s sand velocity and 30 degree impingement angle: (a) at low magnification and (b) at high magnification.	105

Figure 4-26: SEM images of eroded surface of alloy A tested at 98 m/s sand velocity and 90 degree impingement angle: (a) at low magnification and (b) at high magnification. 107

Figure 4-27: SEM images of eroded surface of alloy B tested at 98 m/s sand velocity and 90 degree impingement angle: (a) at low magnification and (b) at high magnification. 108

Figure 4-28: SEM images of eroded surface of alloy C tested at 98 m/s sand velocity and 90 degree impingement angle: (a) at low magnification and (b) at high magnification. 109

Figure 4-29: SEM images of eroded surface of alloy D tested at 98 m/s sand velocity and 90 degree impingement angle: (a) at low magnification and (b) at high magnification. 110

Figure 4-30: SEM images of eroded surface of alloy E tested at 98 m/s sand velocity and 90 degree impingement angle: (a) at low magnification and (b) at high magnification. 111

Figure 5-1: Logarithmic plot comparison of the hardness penetration theory with approximate average for normal impact test results [6]..... 118

Figure 5-2: Comparison of Erosion rates at sand impact velocity of 84 m/s..... 123

Figure 5-3: Comparison of erosion rates at sand impact velocity of 98 m/s. 123

Figure 6-1: Predicted erosion rates using the modified S-K model; (a) at 84 m/s particle impact velocity and (b) at 98 m/s particle impact velocity. 138

1 Chapter: Introduction

1.1 Background of Present Research

1.1.1 Fundamentals of Stellite alloys

Stellite alloys are one type of superalloys, which are cobalt-based, designed for use in various industries, primarily for wear resistance application involving unlubricated systems or at elevated temperatures [1]. They possess excellent adhesive and abrasive wear resistance, solid particle and cavitation erosion resistance, as well as corrosion resistance. They also display a unique combination of mechanical, tribological and high temperature properties [1].

A certain amount of tungsten or molybdenum, a large amount of chromium and a small amount of carbon (usually less than 3 weight percent, i.e., 3 wt%) are the common elements present in Stellite alloys, which lead to carbide precipitation in a cobalt solid solution matrix as the main strengthening mechanism of these alloys [1]. A combination of the crystallographic nature of cobalt, the solid-solution-strengthening effects of chromium, tungsten, and molybdenum, the formation of metal carbides, and the corrosion resistance imparted by chromium all govern the most properties of Stellite alloys [1]. Carbon content alone can be used to distinguish between different Stellite alloys with respect to wear resistance, making carbon a very important element and the carbide volume fraction in the material a critical parameter [1]. Stellite alloys are generally classified into three main categories: (1) high-carbon Stellite alloys designed for wear service; (2) medium-carbon Stellite alloys used for high temperature service; and (3) low-carbon Stellite alloys used against corrosion or simultaneous corrosion and wear [1].

The two principal roles of chromium in Stellite alloys are: (1) It is the predominant carbide former. (2) It provides additional strength, corrosion and oxidation resistance to the alloys [1]. Dislocation motion in Stellite alloys is prevented by solute atoms of tungsten and molybdenum owing to their large atomic sizes [1]. On the other hand, when tungsten is present in large amounts, it contributes to carbide formation [1]. In addition, when molybdenum is present in large amounts, it contributes to the formation of intermetallics formation [1]. These three mechanisms enhance the strength of Stellite alloys [1]. The overall corrosion resistance of Stellite alloys is also improved by these two elements (tungsten and molybdenum) [1].

1.1.2 Application of Stellite alloys

Superior tribological properties, excellent mechanical strength, outstanding resistance to loading under static, fatigue, and creep conditions, good surface stability, excellent oxidation and corrosion resistance, and good phase stability at high temperatures, are all distinctive properties of Stellite alloys [[1], [2]]. Processing techniques such as heat treatment or rationalization of constituent elements can be used to vary the properties of Stellite alloys [[2], [3]]. Solid-solution-strengthening (by solid solution hardening) is the strengthening mechanism of low carbon content Stellite alloys while precipitation-hardening (usually by a combination of carbide formation, precipitation, and solid solution hardening) is the strengthening mechanism of medium or high carbon content Stellite alloys [[1], [2]]. Because of their quite high chromium content, Stellite alloys maintain good hot corrosion, sulfidation, and oxidation resistance at elevated temperatures [3]. Due to these properties, they are known to possess high

wear resistance, high hardness and high corrosion resistance, at both room temperature and elevated temperatures [[3], [4]]. These alloys can be used in various forms such as casting, weld overlays and powder metallurgy (P/M) [2]. Stellite alloys are primarily employed for wear resistance application, in corrosive environments and are valued for their ability to operate in a range of elevated temperatures beyond the ability of conventional materials, such as steels [4].

Stellite alloys are employed in a wide range of industries, such as aerospace, nuclear, mining, oil and gas, and automotive industries [[3]-[5]]. Within these industries, they are utilized in harsh conditions that involve elevated temperatures, severe wear, erosion and corrosive environments or any combination of these [4]. For instance, Stellite 6B is commonly used for erosive wear resistance in coal conservation [5]. A variety of degradation problems exist in aircraft gas turbine engines as a result of metal-to-metal wear, fretting, hot corrosion, and solid particle erosion [3]. This degradation is accelerated due to the high-temperature conditions involved and the failure of such critical equipment can be catastrophic [3]. In this case, a Stellite alloy is the best option. Another case of Stellite alloy application involves machining tools, where conventional materials would result in decreased service life, compared to the Stellite alloy equivalents [3]. Stellite alloys have proven to be beneficial in the aforementioned industries [3]. As the use of Stellite alloys becomes more prominent, their application will expand into more industries.

1.2 Introduction of Present Research

1.2.1 Significance and objectives

In a variety of industries, erosion is the destruction of a material due to its impact with elements traveling at a high speed. It is a typical mode of component degradation in aircraft engines that could eventually lead to component failure [[5]-[7]]. The damage caused by erosion usually results in rapid failure with little or no warning because its effects are unevenly distributed within the component, as a consequence, regions of stress concentrations are generated [7]. For example, in turbomachinery erosion can be detected on the blades of turbines or compressors [[5], [7]]. Its occurrence is related to the presence of particles in the steam/air that move at a high speed colliding with the blades, causing destruction of the latter. Erosion causes loss of efficiency of the blades, and finally can cause complete destruction of the blades, which leads to severe damage of the machine [[4], [7]]. As mentioned earlier, one of the common applications of Stellite alloys is against wear in various erosion environments. In other words, erosion constitutes one of the most challenging issues limiting the service lifetime of Stellite alloys. This therefore calls for a good understanding of the behavior of these materials under erosion attack.

Although Stellite alloys have been extensively studied in various aspects such as corrosion, wear and mechanical properties, due to the limitation of testing facilities/methodologies and the complexity of analytical methods, very little research in erosion of Stellite alloys has been reported, in particular, the systematic investigation of erosion behaviour of these materials. Relationships between erosion resistance, chemical

compositions and microstructures for Stellite alloys have never been studied. Some of the other key issues that have not been addressed are summarized as:

- (1) Effects of constituents in the chemical composition of Stellite alloys on their erosion resistance and composition optimization for best erosion resistance.
- (2) Hardness is considered as an important material property for Stellite alloys because it is often used to correlate with erosion resistance of materials. It is generally accepted that the harder the material, the higher the erosion resistance is. This hypothesis needs to be verified for Stellite alloys as this correlation is useful to material engineers when designing the composition for Stellite alloys with respect to the influence of alloying elements on overall hardness and erosion resistance.
- (3) The impingement angle dependence on the erosion rate of Stellite alloys has not yet been investigated. However, these data help in understanding of the damage of these alloys under different erosion conditions. In particular, it is necessary to determine the “critical impingement angle” for these alloys at which the maximum erosion rate occurs.
- (4) Although many erosion models have been developed to predict the erosion rates of various materials, there is no specific model geared to predicting the erosion rate of Stellite alloys. Such a model will help save testing cost for industries as it could be used as a basis of first hand trial in determining erosion damage of Stellite alloys.

The lack of knowledge in these aspects is significantly limiting the application of Stellite alloys in erosive environments. It is more critical, as applications in increasingly severe environments push engineered materials to their limits, therefore a better understanding of these relationships involving chemical composition, microstructure,

hardness and erosion for Stellite alloys, together with a predictive erosion model, is crucially required, and hence it is the emphasis of this research.

The present research was aimed to investigate the erosion resistance and to develop an analytical model for predicting the erosion rate of Stellite alloys, with a focus on the effects of chemical composition on the microstructures, overall hardness and erosion resistance. The overall hardness of these alloys was determined and related with chemical composition and erosion resistance. The erosion rate was also related to microstructure, impingement angle and erodent particle impact velocity. The erosion model was developed by modifying an existing erosion model and implemented using experimental data for verification. These research results are not only beneficial for extending the application of existing Stellite alloys but also provide the scientific guidance for designing new Stellite alloys that will be used to combat against erosive environments.

1.2.2 Tasks and methodologies

A group of Stellite alloys either in cast state or in wrought state were selected in this study. These alloys contain various levels of carbon and hence are classified as low- (< 0.5 wt%), and medium- (0.5 ~ 1.6 wt%) Stellite alloys, respectively, which are commonly employed or are potentially materials for erosion resistance applications. As the main agent of carbide formation, chromium varies between 22 ~ 30 wt% in these alloys. They contain the main solid-solution-strengthening elements, tungsten, varying from zero up to 32 wt%, and molybdenum, varying from zero up to 11.8 wt%.

The microstructures of these alloys were analyzed utilizing a Hitachi Model S-570 Scanning Electron Microscope (SEM) with backscatter electron imaging (BEI) and energy dispersive X-ray (EDX) spectrum, and a TESCAN Scanning Electron microscope (SEM) with an EDAX energy dispersive X-ray (EDX) spectroscopy system. Each phase in the microstructures was identified.

The overall Rockwell C (HRC) hardness and Vickers hardness (HV) of each alloy were measured and used for the study of the correlations between material properties and also used in the erosion model development.

The erosion resistance of each alloy at room temperature ($\sim 22^{\circ}\text{C}$) was evaluated at two impingement angles of 30 degree and 90 degree and for two particle impact velocities of 84 m/s and 98 m/s, which led to four testing conditions for each alloy, according to the solid-particle impingement erosion test using an S.S. WHITE Airbrasive Micro-Blasting Jet Machine, with compressed nitrogen gas jets. The material eroded or loss of each alloy specimen was calculated and the erosion rate was expressed in two different forms. In one form, the erosion rate was expressed as the ratio of the mass loss of the target material to the mass of the erodent particle used with units ($\mu\text{g/g}$). In the other, the erosion rate was expressed as the ratio of the volume loss of the target material to the mass of the erodent particle used with units (m^3/g). The tribological behavior and erosion mechanism of these alloys at room temperature were studied, incorporating with the analyses of eroded surfaces using SEM, focusing on the surface morphology.

The analytical erosion model was developed by modifying the erosion model originally developed by Sheldon and Kanhere [6] for both single-particle erosion and multiple-particle erosion, with emphasis on incorporating an additional erosion parameter

(the impingement angle). This modified erosion model was implemented using the experimental erosion data for verification and then used to predict the erosion rates of these Stellite alloys at other impingement angles.

Based on the experimental and modeling results, the following relationships were discussed:

- (1) Microstructure versus chemical composition
- (2) Overall hardness versus chemical composition
- (3) Overall hardness versus erosion resistance
- (4) Microstructure versus erosion resistance
- (5) Erosion rate versus particle impingement angle
- (6) Erosion rate versus particle impact velocity
- (7) Original erosion model versus modified erosion model
- (9) Experimental data versus modified erosion model
- (10) Experimental error versus prediction accuracy of modified erosion model

1.3 Organization of the Thesis

This thesis is a summary of the present research. It consists of seven chapters that cover the introduction of this research; literature review of previous studies that are related to the present research; microstructural analysis and experimental investigation of erosion behaviour of Stellite alloys; analytical modeling of erosion of Stellite alloys; discussion on the experimental and modeling results and relationships between chemical composition, microstructure, hardness, erosion resistance and erosion model prediction

for Stellite alloys, as well as the conclusions drawn from this research along with the future work as expected. The details of the thesis structure are described below:

Chapter 1 is an introduction to the present research. In this chapter, the fundamentals, features, properties and application of Stellite alloys, are briefly introduced; the significance and objectives of this research are stated; and the tasks and methodologies of this research are described.

Chapter 2 is the literature review, which summarizes the main aspects of Stellite alloys, including chemical composition, classification, microstructure, features, and various properties, and previous research in these alloys with regard to the following aspects: mechanical properties, corrosion and erosion resistance, wear behaviour, etc. In addition, the numerical models previously developed by other investigators in relation to metal erosion have also been reviewed.

Chapter 3 is the microstructural analysis of the Stellite alloys being studied. In this chapter, the selection of these alloys for this research is explained; the detailed chemical compositions of each alloy are provided; the facilities and procedures for microstructural analysis of these alloys are described; and the results are discussed.

Chapter 4 is the description of the erosion experiment. The experimental details of the solid-particle impingement erosion using gas jets are described, including the apparatus, test parameters and procedure. The method for material eroded or loss calculation is detailed. The erosion mechanisms of Stellite alloys at room temperature are explored, incorporating with the eroded surface analyses using SEM.

Chapter 5 is the description of the erosion model development. The reasons for choosing the original model are explained, the original model is compared with the

experimental results and the drawbacks calling for modification are revealed. The model modification process is detailed and the modified model is obtained by fitting the experimental data and introducing an additional erosion parameter (impingement angle).

Chapter 6 is the discussion on the experimental and modeling results as well as the correlations of these results. This chapter can be considered as an integration of all results. The correlations between chemical composition, microstructure, hardness and erosion resistance, of Stellite alloys, are analyzed. The new fitting parameters introduced in the modified model are discussed and the modified model is used to predict the erosion rates of Stellite alloys at various particle impingement angles, with the limitation of the model discussed.

Chapter 7 concludes the present study and proposes the future work. The experimental and analytical results of this research are summarized, the conclusions drawn from these results are provided. The expected work that will provide further understanding of the room-temperature erosion behaviour and performance of Stellite alloys are proposed together with the suggestions on how to improve the modified erosion model in order to enable the erosion rate prediction at any particle impingement angle for Stellite alloys.

2 Chapter: Literature Review

2.1 Erosion of Materials

2.1.1 Definition of erosion

Wear of materials is generally grouped in three main classes namely: abrasive wear, sliding wear and erosive wear. When two hard surfaces in contact move relatively to each other, it causes abrasive wear [1]. Therefore the size and volume of hard phases in a material control the abrasive resistance of the material [4]. There are three main mechanisms involved in sliding wear namely: oxide control, contact stress and subsurface fatigue [1]. The resistance to sliding wear of a material depends on the overall hardness and strength of the material [[3], [4]]. Erosion is a complex process that is characterized by the progressive deterioration of materials [[8]-[10]]. The impact of particles or cavitation shocks against a surface result in erosive wear [11]. The time duration within which the impinging particle and the target surface are in contact, is very short (i.e., this erosive wear is not a continuous process) making it completely different from the other types of wear [1]. Solid-particle erosion, slurry or liquid-solid particle erosion, liquid-droplet erosion and cavitation erosion are the well-recognized types of erosive wear [[1], [11]]. When small, solid particles impact against a surface, the first or second type of erosive wear occurs [[1],[11]]. However, when gas bubbles generated on a surface due to a flowing liquid suddenly collapse, cavitation erosion occurs on the surface [[1],[11]]. With the complex mechanisms of erosion, it is hard to predict the erosion resistance of a material based on a single material property [1]. For example, hardness definitely affects the erosion resistance of a material, but ductility can also be a major parameter governing the erosion behavior of a material [[1],[8]].

2.1.2 Solid-particle erosion

The successive impact and removal of material by fast moving hard particles from the surface of components is known as solid-particle erosion [1]. It is different from the other forms of erosion like liquid impact erosion, slurry erosion, cavitation erosion, etc [1]. As mentioned earlier, the contact between the hard particles and the component surface is of a very short duration. Thus each particle impact on the target surface could be regarded as independent from one another in solid-particle erosion [1]. By adding up the effect from each impact, the overall material degradation can be estimated [7]. Another definition of solid-particle erosion could be proposed as material deterioration due to impacting particles transported via a fluid (liquid or gas) [11].

There are several impact parameters that influence the erosion rate of any particular material [[12]-[14]]. The extent to which each parameter contributes to the erosion rate would depend on the environmental conditions together with the type of material under investigation [[12]-[14]]. The main impact parameters are impact angle, particle velocity, particle size, shape and properties of both the abrasive particles and the target material under consideration [[7]-[22]].

In most industry applications, erosion is caused by a stream of particles [[15], [17]]. Degradation of materials due to solid particle erosion, either at room temperature or at elevated temperatures, is encountered in a large variety of engineering industries, as described in Table 2-1. On the other hand, applications such as sand blasting of castings, shot peening of rotating components and many others have benefited from the material deterioration effect of erosion [7]. Therefore it is very beneficial to investigate both the technological and commercial aspects of erosion.

Table 2-1: Examples of components subjected to solid particle erosion [15]

System	Components
Chemical plant	Transport tubes carrying abrasive materials in an air stream
Hydraulic mining machinery	Pumps and valves
Propellant system	Rocket motor's tail nozzle, gun barrel
Combustion system	Burner nozzle, reheater, super heater and economiser tube banks
Fluidized bed combustor	Boiler heat exchanger tubes in bed tubes, tube banks and expander turbine
Coal gasification	Turbine, lock hopper valves
Coal liquifaction	Valve to throttle the flow of product steam
Aircraft engine	Compressor and turbine blades
Helicopter engine	Rotor and gas turbine blades

2.2 Parameters of Erosion

2.2.1 Impingement/impact angle

The angle between the path followed by the abrasive particles and the target material is known as the impact angle [8]. This is demonstrated in Figure 2-1.

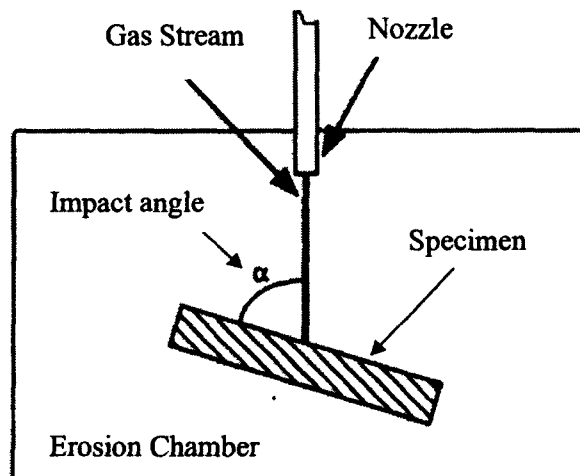


Figure 2-1: Schematic diagram depicting the impingement/impact angle [8].

For every material, there exists a “critical impingement angle” at which the maximum erosion rate occurs. For metals and alloys, i.e., ductile materials, this angle occurs between 15 degree and 30 degree while for ceramics and glass, i.e., brittle materials, this angle occurs around 90 degree as illustrated in Figure 2-2 [[7], [15]]. The erosion degradation of a material varies with particle impact angle, but sometimes it is impossible to determine the critical angle experimentally in industry due to equipment and time limitation [[8], [15]]. As mentioned earlier, the nature of the target material greatly influences the effect of the impact angle on the erosion rate [1]. Also, the erosion rate-impact angle behavior is significantly controlled by erodent particle shape [9]. It was reported that when spherical particles were used to erode mild steel and copper (ductile materials), a maximum in the erosion rate occurred at 90 degree instead of at an intermediate angle close to 30 degree [[9], [10]]. In addition, the critical angle changes with particle impact velocity for some materials [8].

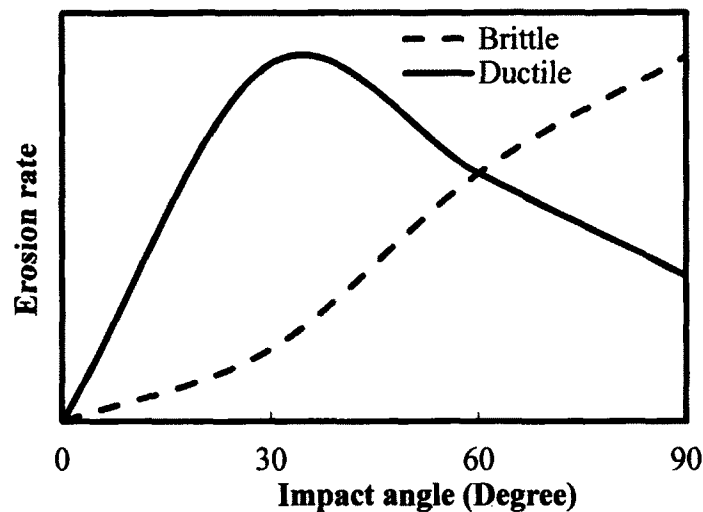


Figure 2-2: Schematic diagram showing the influence of impact angle on erosion rate in the case of ductile and brittle materials [7].

2.2.2 Erodent particle impact velocity

In general, erosion rate is mostly affected by particle impact velocity [8]. The erosion rate of a material could be defined as the ratio of the mass loss of the target material to the amount of erodent particles used [15]. Some researchers have suggested that the erosion rate, E , can be expressed as a function of impact velocity, V , as follows [6]:

$$E = E_0 V^p \quad (1)$$

where E_0 is a constant; and p is velocity exponent.

A lot of experimental data on erodent particle impact velocity have been collected for metallic materials under oblique impact conditions by some investigators and they found that the mean velocity exponent was between 2.4 and 2.55 [[12],[13]]. This velocity exponent could go up to 5 for polymer matrix composites [15]. Other parameters such as impact angle, particle size, erodent particle shape, and so on, may also affect the velocity exponent [15]. A decrease in the velocity exponent with decreasing particle size was also reported [14]. In general, the higher the erodent particle velocity, the higher the material removal rate (erosion rate) and vice versa, as shown in Figure 2-3.

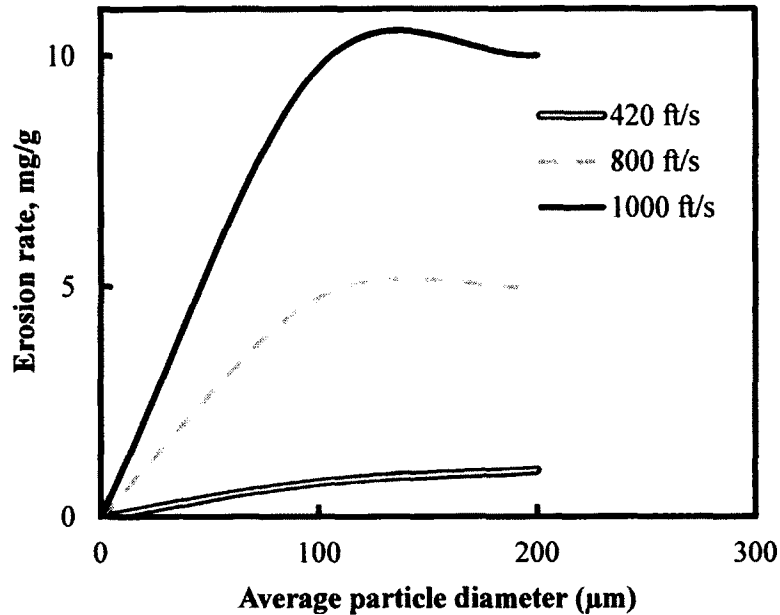


Figure 2-3: Variation of erosion rate of steel with particle size at different impact velocities [15].

2.2.3 Erodent particle size

The erosion degradation of a material may also be influenced by the size of the sand particle (erodent) [[15],[19]]. An increase in the erosion rate with particle size has been reported by previous researchers [[16]-[18]]. However, they observed little or no change in erosion rate once the size of the particle was greater than a threshold value in the range of 50 ~ 100 μm, as shown in Figure 2-3. Both an increase in erosion rate and a decrease in erosion rate with particle size were observed for some erodent particles in previous research [[16]-[18]]. Although a few suggestions have been proposed to explain the ‘size effect’, no general conclusion has been attained [[16]-[18]].

2.2.4 Erodent particle shape, hardness and particle flow rate

Another parameter that affects the erosion behavior of materials is erodent particle shape [[9], [15]]. Angular particles were observed to produce higher erosion rates when used as the erodent on many metallic materials than spherical erodent particles [[10],[19]]. A shift in the critical impingement angle from 30 degree to 90 degree was found in erosion test on some Cu alloys when eroded by spherical particles [[10],[19]]. When a spherical steel shot was used to erode Cu and some Cu based alloys, a maximum in the erosion rate occurred at 90 degree impact angle [[10],[19]]. The reverse behavior was observed on these same Cu alloys when eroded by angular SiC particles, where a ductile response with regard to erosion damage was revealed [[10],[19]]. This can be seen in Figure 2-4, where the effects of angular and spherical particles on Cu alloys were investigated. In conclusion, the angle-dependence of erosion rate shifts more towards a ductile mode as the angularity of the erodent particle increases [15]. In addition, the increase in angularity also leads to an increase in the erosion rate [15].

Another parameter of interest is the hardness of the erodent particle [15]. The erosion rate of steel was found to be independent of the particle hardness once the hardness of the erodent particles was at least twice that of the target material [20]. Up to date, no general trend for the 'erodent particle hardness effect' has yet been obtained [15].

Particle flux rate should also be considered [15]. The erosion rate of metallic materials is barely influenced by erodent particle flux rate [[6], [8]]. This is because some

rebounding of erodent particles against one another at very high flux rates can cause the erosion rate to decrease and this decrease could follow an exponential trend [15].

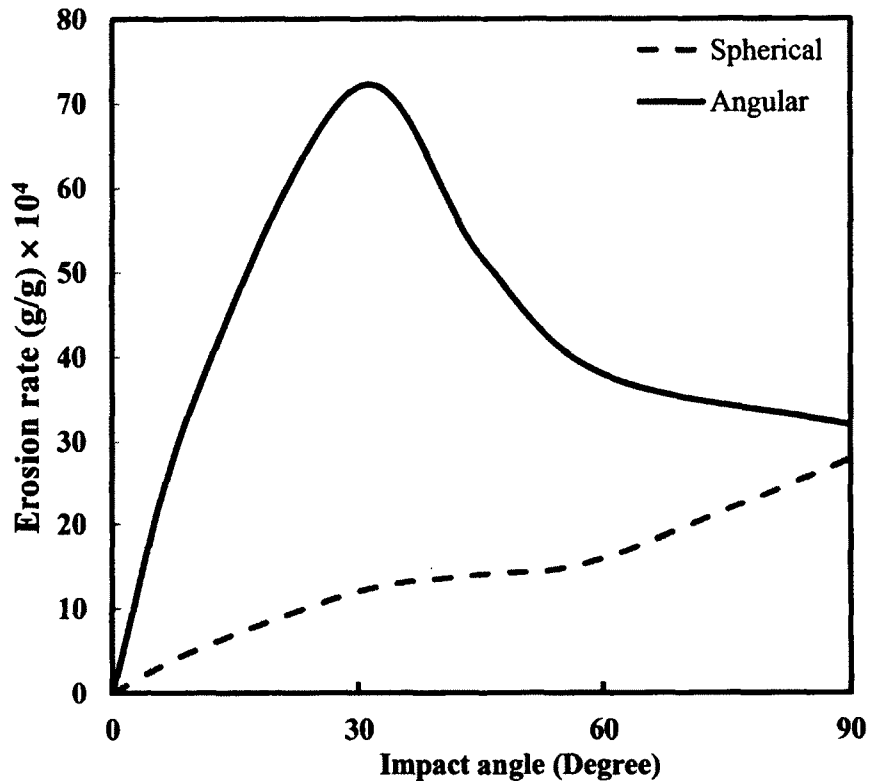


Figure 2-4: Effects of particle shape on erosion rate [15].

2.2.5 Target material

The erosion behavior of a material can be greatly influenced by its mechanical properties [1]. In most situations, the material hardness tends to be representative of its mechanical properties [[10],[11],[15]].

For single-phase metals and alloys, their erosion resistance is immensely improved by various strengthening mechanisms such as cold work or solid solution strengthening [15]. Although addition of other elements in solid solution strengthening

generally increases the hardness/strength of the material, there are exceptions [15]. For example, the addition of solutes like Zn and Al into Cu increases the hardness/strength but not the erosion resistance [21].

On the other hand, for multiphase metals, the erosion behavior of carbon steels having different carbon contents was studied and a lower erosion resistance was observed for the steel having higher carbon content [[15],[22]]. Higher erosion rate is often found on dispersion-strengthened alloys than on the same alloy without the dispersion [15].

It should be noted however that within metallic materials, there is always a slight variation in the sensitivity of the above-mentioned parameters that are used to predict the severity of erosion damage [[23],[24]]. This thus leads to a case-by-case analysis, which is very time-consuming and makes erosion damage investigation difficult.

More often, a combined erosion-corrosion wear process occurs when erosion takes place in a corrosive medium [20]. This adds even more complexity to the erosion damage investigation and calls for more rigorous research techniques.

2.3 Methodologies of Erosion Research

2.3.1 Experimental investigation

A number of experimental research has been conducted in the field of erosion damage for different materials. Oka *et al.* [8] estimated the erosion damage to ceramic materials caused by solid particle impact using different erodent particles such as angular silica sand (SiO_2), silicon carbide (SiC) and round zirconia (ZrO_2) having mean particle sizes of 194 or 254 to 428 and 200 μm respectively. In their research, they used silicon carbide, two types of alumina (Al_2O_3 -1 and Al_2O_3 -2), zirconia and magnesia (MgO) as

the target materials, at impingement angles between 10 degree and 90 degree [8].

Table 2-2 provides more details about the mechanical properties of the above materials.

Figure 2-5 shows a schematic diagram of the sand blast type erosion test rig used in their investigation.

Table 2-2: Particles and target materials in the erosion test of Oka *et al.* [8]

Particle	Shape	Diameter (μm)	Material hardness HV (GPa)	
SiO ₂	Angular	194-428	ca. 20	
SiC	Angular	254-428	ca. 30	
ZrO ₂	Round	200	ca. 20	
Material	Density (g/cm ³)	Grain size (μm)	HV (GPa)	Fracture toughness (MPam ^{1/2})
SiC	2.9	-	23	3.6
Al ₂ O ₃ -1	3.4	10	15	3.7
ZrO ₂	6	0.2	13	6
Al ₂ O ₃ -2	3.6	3	11	3.1
MgO	3.5	35	7	3

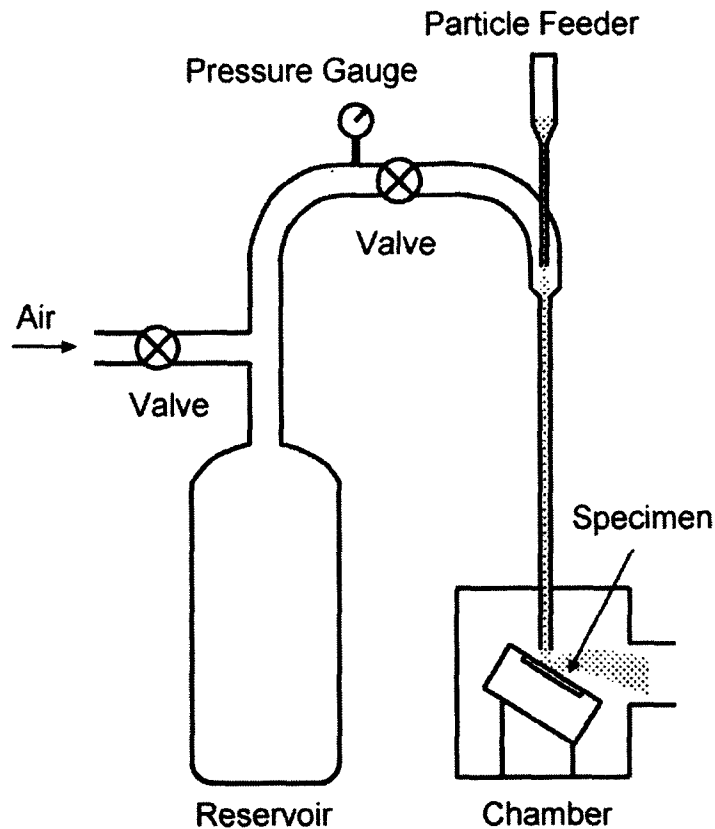


Figure 2-5: Schematic diagram of a sand blast type erosion test rig [8].

The solid-particle erosion resistance of ceramic materials is generally much higher than that of metallic materials [8]. Impact parameters such as particle type and size were noted to influence the erosion behavior of ceramic materials significantly, which resulted in a shift in the impact angle-erosion rate dependence [8]. The material removal mechanisms of primary ceramic grains were different from those of secondary ceramic grains [8]. The impact-angle dependence for normalized erosion of different target materials eroded by 254 μm angular SiC particles is illustrated in Figure 2-6. At lower impact angles, the erosion damage caused by SiC the abrasive particles was found to be much less on SiC target material than on the other target materials [8].

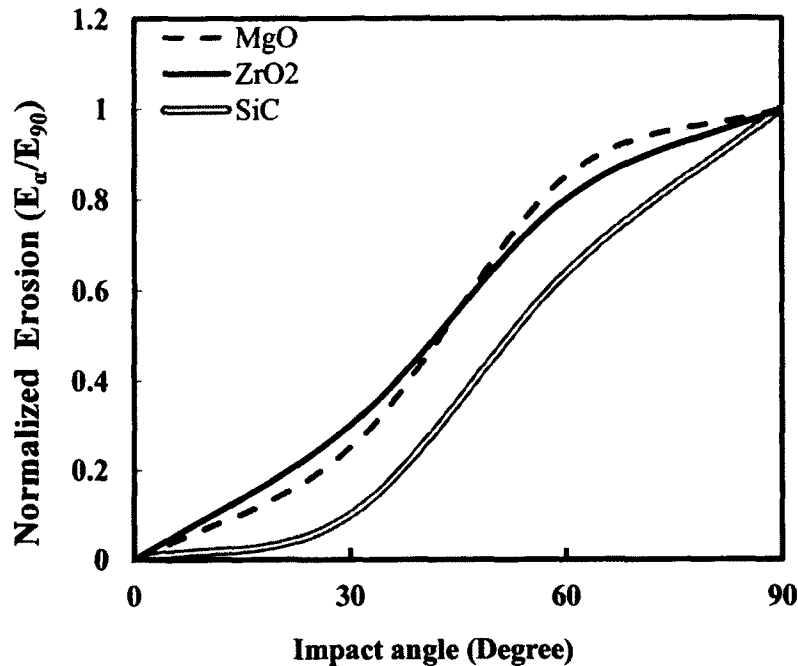


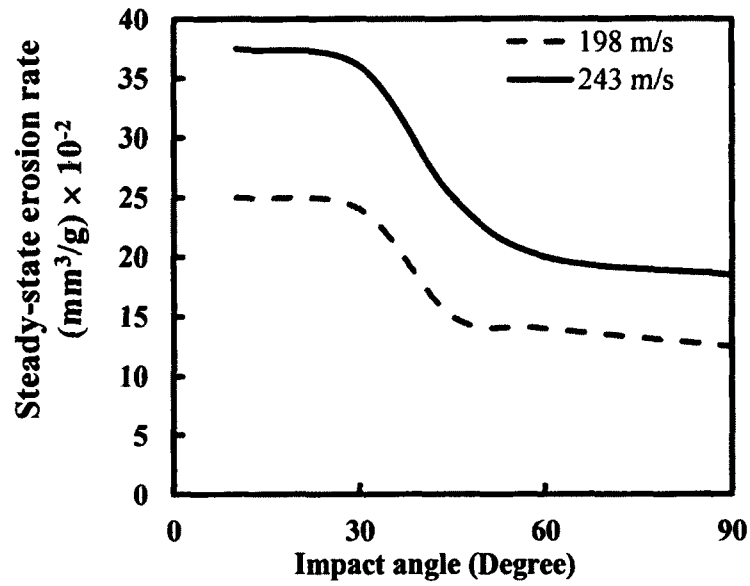
Figure 2-6: Impact-angle dependence of normalized erosion using silicon carbide particles of 254 μm at 100 m/s [8].

McCabe *et al.* [22] performed erosion experiments to verify the effect of microstructure on the solid particle erosion behavior of steels. They used AISI-SAE 1078 and 10105 steels as the target materials. In their experiments, 240 grit Al_2O_3 particles were used as erodent particles and the experiments were conducted at impingement angles between 10 degree to 90 degree at impact velocities of 40 ~ 100 m/s [22]. Spheroidite, pearlite, martensite and tempered martensite microstructures for these steels were investigated [22]. The critical impingement angle for spheroidite and pearlite microstructures occurred at 40 degree at all particle velocities, which is an indication of ductile mode of erosion [[7],[22]]. Their results also showed a drift in the erosion mode for martensite and tempered martensite towards a brittle mode of erosion with increasing

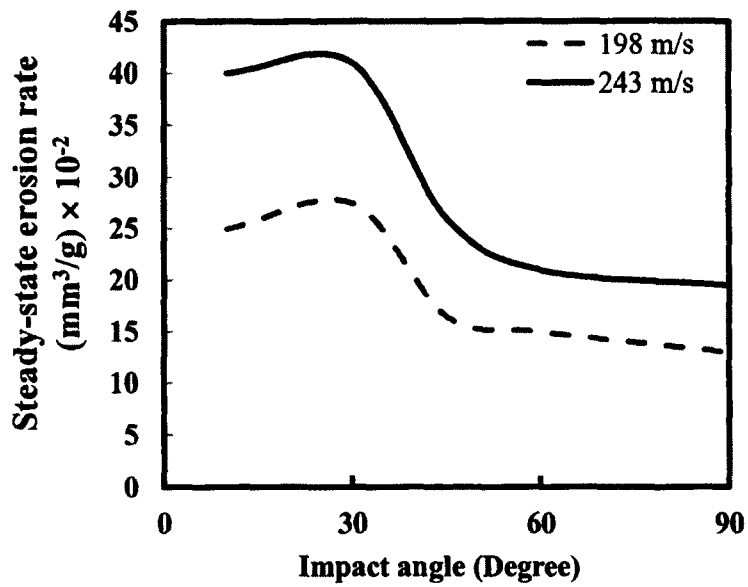
velocity [22]. However, this drift was not consistent at some particle velocities [22]. Finally after comparing the erosion rates between the eutectoid and hypereutectoid microstructures, a wider deviation in the values of the erosion rate was observed at the highest velocity of 99 m/s than at the lowest velocity of 42 m/s [22].

Levy [23] found that by decreasing the hardness or equivalently increasing the ductility of pearlite and spheroidite microstructures led to a decrease in the erosion rate. In order to explain this observation, Levy used the fact that plastic deformation of the target material picks up most of the kinetic energy of the impacting particles leaving a small amount available for surface fracture [23]. Thus brittle (harder) materials could erode faster than softer (ductile) materials depending on the impingement angle under consideration [23].

Tu *et al.* [24] investigated the solid particle erosion behavior of $\text{Al}_{18}\text{B}_4\text{O}_{33}$ whisker-reinforced AC4C Al alloy matrix composites at room temperature. They used angular silica sand as erodent particle at four different impact velocities of 55, 140, 198 and 243 m/s [24]. Impingement angles between 15 degree and 90 degree were used in their investigation. This was carried out on AC4C Al alloy in a squeeze-cast state containing 19.5 vol% $\text{Al}_{18}\text{B}_4\text{O}_3$ whisker as the target material [24]. At high particle velocities and large impact angles, they observed an increase in the steady-state erosion rate of the whisker reinforced matrix alloy, as demonstrated in Figure 2-7. During the erosion process, the introduction of the whisker into the matrix rendered the overall composite less ductile leading to limited plasticity but rather more fragmentation of $\text{Al}_{18}\text{B}_4\text{O}_3$ whisker resulting in an increase in the erosion rate [24]. This is also in agreement with Levy's observation [23].



(a)



(b)

Figure 2-7: Steady-state erosion rate as a function of impact angle for (a) AC4C matrix alloy, (b) AC4C Al- Al₁₈B₄O₃ whisker composites [24].

Although a huge number of experiments have been performed concerning erosion damage of various materials [[20]-[24]], the results obtained are often case by case and therefore more experimental investigation needs to be carried out in order to better understand the material removal mechanisms involved in material erosion degradation.

2.3.2 Analytical modeling

Due to the high capital cost and long duration involved in erosion testing, physics-based and statistics-based erosion models have been developed to predict/reveal the erosion resistance/mechanisms of materials [[25]-[38]]. These models could also be used to predict the service life of materials in erosive environments [7].

A number of studies have proposed a variety of correlative equations between impact parameters and erosion damage caused by solid particle impact [[25]-[38]]. The earliest report on erosion investigation was attributed to Reynolds [25]. He also performed some in-depth studies in erosion and since then, a substantial number of specialized studies in the field erosion damage have been reported [25].

The erosion process was assumed to be a micro-machining process during the development of the first erosion model on ductile materials by Finnie [26]. His model was based on an ideal ductile, non-work hardening solid target material eroded by rigid particles [26]. He then proposed that the volume loss, Q , removed by a single abrasive grain of mass to be [26]:

$$Q = \frac{mV^2}{\sigma_f \psi K} \left(\sin 2\alpha - \frac{6}{K} \sin^2 \alpha \right) \quad \text{if } \tan \alpha \leq \frac{K}{6} \quad (2)$$

$$Q = \frac{mV^2}{\sigma_f \psi K} \left(\frac{K \cos^2 \alpha}{6} \right) \quad \text{if } \tan \alpha \geq \frac{K}{6} \quad (3)$$

where α is impingement angle; V is particle impact velocity; K is the ratio of the vertical to horizontal force on the particle at impact; σ_f is plastic flow stress; and finally ψ is the ratio of the length to the depth of the cut material whose value is assumed to be constant.

Finnie [27] further expanded his original model and proposed another formulation for single particle erosion. At the beginning of his derivation, he made three major assumptions as follows [27]: (1) Plastic deformation of the material is the unique factor causing surface cutting. (2) Surface cracking is ignored. (3) Only the motion of the impacting particle on the target surface leads to material removal.

By applying Newton's second law of motion to the single particle impacting a ductile surface, erosion rate was determined [27]. The volume of surface material displaced by the particle was estimated by using the particle trajectory through the material [27]. He then proposed a single particle impact erosion model as follows [27]:

$$w = \left(\frac{\rho m V^2}{p \psi K} \right) F(\alpha) \quad (4)$$

where

$$F(\alpha) = \begin{cases} \sin 2\alpha - \frac{6}{K} \sin^2 \alpha & \text{for } \tan(\alpha) < \frac{K}{6} \\ \frac{K \cos^2 \alpha}{6} & \text{for } \tan(\alpha) > \frac{K}{6} \end{cases}$$

w is the mass loss of the material from the single particle impact; ρ is target material density and m is erodent particle mass; the parameter p is the horizontal component of the contact stress also known as plastic flow stress which is assumed to attain a constant value immediately upon contact. α is impingement angle; V is particle impact velocity; K is the ratio of the vertical to horizontal force on the particle at impact; Experiments on

ductile materials have determined K to lie between 1.6 ~ 2.4 with a maximum value up to 6 [[7],[27]]. ψ is the ratio of the length over which the abrasive particle contacts the surface to the depth of the cut made by the particle which is also assumed to attain a constant value immediately upon contact. Experiments at different impact angles have revealed ψ to lie between 2 ~ 10 [[7],[27]].

Equations (2), (3) and (4) predict high erosion rates at impact angles between 15 degree and 30 degree for ductile materials, which agree with experimental data [[7],[27]]. At impingement angles 60 degree and above, these equations however contradict experimental results [[7],[27]]. In addition, at impingement angles close to 90 degree, the predicted erosion rates are approximately zero [[7],[27]]. The high velocity exponent found in this model was attempted to be corrected by Finnie *et al.* However, an inverse relationship between erosion rate and yield stress or material hardness was predicted by the original Finnie model [27]. This relationship was not observed experimentally and has become a huge drawback to this model [7].

Studies in the erosion behavior of ductile materials were conducted by Tilly [28]. Material scrapping and extrusion (forming ridges) were proposed as the material removal mechanism involved in erosion of ductile materials [28]. These ridges became vulnerable when attacked by particles moving at a high velocity [28]. Tilly [29] further developed a two-stage model of the erosion process for ductile materials. At the first stage, chips are removed and some material is gouged and extruded around the scar as the erodent particles impact the target surface [29]. At the second stage, fragmentation of the particles occurs upon impact and these fragments are projected radially from the

surface [29]. At acute impingement angles, the first stage prevails while at normal impact, the second stage predominates [29].

Bitter [30] developed a model for single-particle erosion of metals. He assumed that both material cutting and material plastic deformation occurred simultaneously but further assumed that “deformation wear” governed at normal impact while “cutting wear” prevailed at acute angles [30]. Empirically determined deformation wear and cutting wear factors as well as target material and erodent particle properties were utilized during the model development [30]. An erosion model of the following form was proposed [30]:

$$w_i = (w_i)_d + (w_i)_c \quad (5)$$

where the contribution from the deformation wear is given by [30]:

$$(w_i)_d = \frac{\rho_w m_p (g \sin \alpha - K_1)^2}{2 \varepsilon_d} \quad (6)$$

The deformation wear factor, ε_d , represents the amount of energy needed to remove a unit volume of surface material through deformation [30]. The contribution from the cutting wear is defined by [30]:

$$(w_i)_c = \left\{ \begin{array}{l} \frac{2 \rho_w K_3 m_p (g \sin \alpha - K_1)^2}{\sqrt{g \sin \alpha}} \left[g \cos \alpha - \frac{K_3 (g \sin \alpha - K_1)^2 \varepsilon_c}{\sqrt{g \sin \alpha}} \right] \text{ for } \alpha \leq \alpha_0 \\ \frac{\rho_w m_p \left[g^2 \cos^2 \alpha - K_2 (g \sin \alpha - K_1)^2 \right]}{2 \varepsilon_c} \text{ for } \alpha \geq \alpha_0 \end{array} \right\} \quad (7)$$

The cutting wear factor, ε_c , represents the amount of energy needed to remove a unit volume of surface material by cutting action [30]. α_0 is the angle of impingement when the horizontal component of g becomes zero and can be deduced by solving the equation below [30]:

$$\frac{0.576 \rho_s^{\frac{1}{4}} g^{\frac{1}{2}} \varepsilon_c}{\gamma_{el}^{\frac{5}{4}}} = \frac{\cos \alpha_0}{\sin^{\frac{3}{2}} \alpha_0} \quad (7)$$

where y_{el} is elastic load limit and K_1 , K_2 and K_3 are material constants given by [30]:

$$K_1 = \frac{\pi^2 y_{el}^{\frac{5}{2}}}{2\sqrt{10}} \sqrt{\frac{1}{\rho_s} \left[\frac{1 - q_1^2}{E_1} + \frac{1 - q_2^2}{E_2} \right]^2} \quad (8)$$

$$K_2 = 0.82 y_{el}^2 \left(\frac{y_{el}}{\rho_s} \right)^{\frac{1}{4}} \left[\frac{1 - q_1^2}{E_1} + \frac{1 - q_2^2}{E_2} \right]^2 \quad (9)$$

and

$$K_3 = \frac{0.288}{y_{el}} \left(\frac{\rho_s}{y_{el}} \right)^{\frac{1}{4}} \quad (10)$$

where the Poisson's ratios of the particle and target surface material are given by q_1 and q_2 respectively; the Young's moduli of the particle and target surface material are given by E_1 and E_2 respectively. This model agreed with his experimental erosion data and gives a better description of the impact angle dependence on wear damage [30]. However, the significant drawback of this model is the fact that little justification to the assumptions made during the model development process has been presented [7].

The expression in equation (7) for the cutting wear component proposed by Bitter was simplified by Neilson and Gilchrist [31], yielding the following form:

$$(w_i)_c = \left\{ \begin{array}{ll} \frac{\rho_w m_p g^2 \cos^2 \alpha \sin \eta \alpha}{2 \epsilon_c} & \text{for } \alpha \leq \alpha_0 \\ \frac{\bar{n}_w m_p g^2 \cos^2 \alpha}{2 \epsilon_c} & \text{for } \alpha \geq \alpha_0 \end{array} \right\} \quad (11)$$

where

$$\alpha_0 = \frac{\pi}{2\eta} \quad (12)$$

The parameter η is an empirical constant and the deformation wear component is the same as in the original Bitter model given by equation (6) [[30], [31]].

As mentioned earlier, the original Finnie model was developed based on an ideal ductile, non-work hardening solid target material [26]. Hutchings and Winter [32] studied

the work hardening and annealing effects on the erosion mechanism of ductile materials. A large-size steel sphere of 3 mm in diameter was used as the single particle erodent and an aluminum surface as the target material in their investigation [32]. They postulated that the material removal mechanism was the shearing of the surface layer of the ductile material in the direction of motion the projectile and an overhanging lip would be formed and removed during the erosion process [32]. They suggested that material removal of this nature could be as a result of either adhesion between the lip and ball or from extrusion of the lip material at the interface between the deformed metal and the ball [32]. Finally, material loss occurred more heavily from the fully work-hardened metals than from the annealed metals indicating that work hardening affected the lip formation [32]. Plastic flow was concentrated in the surface layers and intense localized shearing occurred to form the lip in work-hardened metals [32].

Using spherical particles, Hutchings [33] developed a model for multiple-particle erosion of metals. Their experiments were performed at 90 degree impingement angle and the erosion rate was expressed as the mass loss of the target material per unit mass of erodent particles used [33]. The formation and detachment of platelets of the target material were postulated as the material removal mechanism [33]. Once the plastic strain in the material attained a critical strain, only at this point was this detachment assumed to occur [33]. This critical strain was also called ‘erosion ductility’ of the material [33].

By using the same criterion of a critical strain needed for material removal to occur as Hutchings used [33], Sundararajan and Shewmon [13] developed a model for multiple-particle erosion of metals. They conducted erosion experiments at 90 degree impact angle [13]. However, compared to Hutching’s model, their findings agreed more

closely with their experimental erosion data [13]. They postulated that material removal along the rim of the indentation crater produced by the formation of an extruded lip of material was the main degradation mechanism [13].

A solid-particle erosion model that could be used to estimate the erosion damage of a variety of metals under different erosion conditions was proposed by Oka *et al.* [34]. The impact angle-erosion rate dependence was investigated by developing an erosion damage equation at an arbitrary angle $E(\alpha)$, of the form [34]:

$$E(\alpha) = g(\alpha)E_{90} \quad (13)$$

where E_{90} is the erosion damage at an impact angle of 90 degree with units (mm^3/kg) and $g(\alpha)$ denotes the ratio of erosion damage at arbitrary angles to that at 90 degree, E_{90} . The Vickers hardness of the target material H_V with unit (GPa) together with two trigonometric functions were used to expressed $g(\alpha)$, as given below [34]:

$$g(\alpha) = (\sin\alpha)^{n_1}(1 + H_V(1 - \sin\alpha))^{n_2} \quad (14)$$

where the material hardness and other erosion parameters are used to determine the exponents n_1 and n_2 . In equation (15) repeated plastic deformation is accounted for by the first term [34]. At acute impact angles the second term, which accounts for the cutting action, is more predominant [34]. After performing numerous experiments on different types of materials, the exponents n_1 and n_2 were found to be related to the material hardness [34]. When $n_1 = 2$, the erosion damage could be related to the vertical component of the particle impact energy [34]. For all these different materials, they found n_2 to lie in the range between 0.15 and 15 [34]. Figure 2-8 shows a plot of $g(\alpha)$ versus impact angle and also includes the mechanisms occurring during the material removal process. They concluded that the impact angle dependence for an unknown material

could be estimated from its initial hardness; and further added that particle properties and target material hardness influenced the impact velocity-erosion rate dependence with this characteristic being independent of particle size [34]. One drawback of this erosion model is the fact that there is a significant deviation in the value of the experimental erosion rate from the predicted value [7].

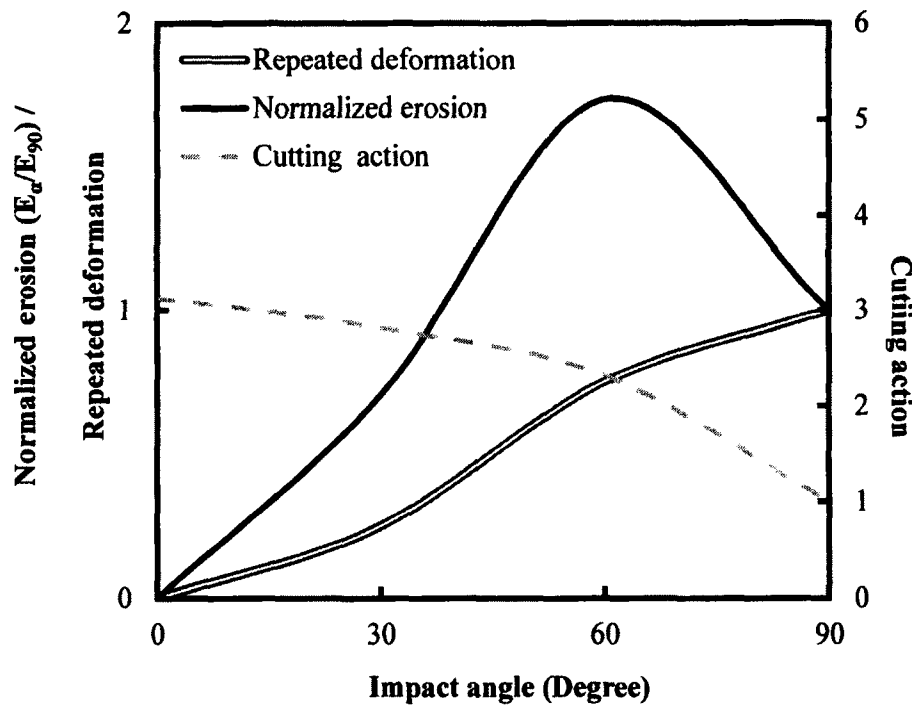


Figure 2-8: The concept of erosion arising from repeated plastic deformation and cutting action [34].

The above predictive equation was further expanded to ceramic materials [8]. In this work, a comparison of erosion rate between the tested commercial ceramic materials and industrial metallic materials was made [8].

Fundamental analyses in solid-particle erosion have been performed by many researchers [[26], [30]], leading to a number of estimative or predictive equations [35], but the development of a practical and effective equation for the degradation of materials in industrial plants remained inadequate [[26]-[35]]. Some models have taken into account both normal impact and oblique impact [[27],[34]]. Moreover, some researchers have developed an expression for predicting the diameter of the crater formed after erosion of a passive film on pure metals [36]. In their investigation, they equated the energy needed to remove a crater volume from the oxide layer to the kinetic energy of the impacting particles [36]. Spherical erodent particles were used in their study and they assumed that the direction of motion of these particles during impact coincided with the direction of all crater shape relaxation [36]. However, depending on the nature of the alloy being studied (ductile or brittle), the deformation mechanism varied [36]. Other researchers performed a similar investigation using both sharp edged and conical particles [[36]-[38]]. The crater diameter expression developed was applicable to both ductile and brittle layers when eroded at 90 degree. Their models also neglected the energy spent in elastic work during the erosion process [[36]-[38]]. In general, material hardness tends to be a representative of the mechanical properties of the target material that affects the erosion mechanisms [[10],[11],[15]]. Researchers reported that material hardness was one of the key parameters required in predicting the impact angle-erosion rate dependence [8].

Unfortunately, the situation becomes more complex, when the abrasives such as salts and sand particles are ingested by the target material, since at high enough temperatures, they can chemically react with the oxygen present in the environment [7].

As mentioned earlier, a combined erosion-corrosion wear process occurred when erosion took place in a corrosive medium [20]. Erosion-corrosion wear has been encountered in coal gasification and liquefaction plants [20]. These complications have motivated many researchers to study the wear behavior and mechanisms of materials to a new dimension.

It should be noted that the effects of the above-mentioned parameters on erosion damage vary with target material [[23],[24]], which leads to a case-by-case analysis. All the above mentioned factors add even more complexity to the erosion damage investigation and calls for more rigorous research techniques. In general, estimative or predictive equations are often difficult to establish because of a wide range of impact conditions, many effective impact parameters such as velocity, angle and particle properties, and a wide variety of metallic materials, material compositions and physical and mechanical properties [[26]-[38]].

In recent years, the introduction of computers to erosion investigation has influenced researchers to advance in a whole new dimension with their studies [7]. Erosion damages have been investigated using computer simulation and numerical methods [7]. The results of these theoretical approaches are promising and indicative of the importance of computer simulation in predicting the damage incurred due to various types of erosive wear [7]. The use of computer simulation and numerical methods has led to a deeper and more comprehensive investigation of erosion [7].

Sheldon and Kanhere [6] have developed an erosion model known as the “S-K model”, in the investigation of the effect of large single particle impact on a 6061-T0 aluminum surface. In the model development, the indentation hardness theory was used to derive a particle penetration equation [6]. The erosion rate w , expressed as a function

of the impacting particle velocity V , and the particle diameter D , has been suggested by a number of investigators and takes the form [6]:

$$w = K V^A D^B \quad (15)$$

where w is erosion wear per erodent particle; A is the velocity exponent; and B is the diameter exponent.

The S-K model [6] uses the erodent particle diameter D (m), the erodent particle impact velocity V (m/s), the erodent particle density ρ_p (kg/m^3) and the Vickers hardness of the target material H_V (Pa) to predict the erosion rate.

The present research selected this model as the basis for analytical modeling, because all the impact parameters required to test the validity of the model were measurable in the present research. Also, 6061-TO aluminum and Stellite alloys are all metallic materials, in a same material domain in regard to erosion [[8],[15]]. Also, an added advantage to this model is that although it was developed based on single-particle erosion, it can be applicable without any restrictions to multiple-particle erosion [6]. This model was then modified by including the effect of particle impact angle and using a statistical method to best fit the experimental erosion data obtained from the present research on Stellite alloys. Up to date, no general, practical, predictive equations for the actual degradation of a variety of types of materials have yet been developed due to the large number of impact parameters involved for consideration [[15],[26]-[38]]. One of the main focuses in the model modification of the present research was to introduce the particle impact angle to the original S-K model [6], which is angle independent.

2.4 Erosion of Stellite Alloys

2.4.1 Microstructure of Stellite alloys

Stellite alloys are cobalt-based, consisting of a high level of chromium, a certain amount of tungsten or molybdenum, and a small amount of carbon [2]. They may also contain other minor elements such as nickel, iron, aluminum, boron, manganese, phosphorus, sulphur, silicon, titanium, and so on [1]. Most Stellite alloys contain about four to six of the listed elements in different proportions [1]. During solidification these elements control the amount and type of carbide formed in the microstructure [1]. There is a strong relationship between carbon content and carbide volume fraction in a Stellite alloy [1]. For example, the carbides in Stellite 3 (with 2.4 wt% C) constitute approximately 30 wt% of the alloy [1]. The two major types of carbides formed in Stellite alloys are: (1) chromium-rich primary carbides designated as M_7C_3 ; and (2) tungsten-rich eutectic carbides designated as M_6C ; where M represents the metal components [1]. The majority of the carbides present in Stellite 6 (with 1 wt% C), for example, are the chromium-rich eutectic carbides; with the overall weight of carbides about 13 wt% of this alloy [1].

The general microstructure of Stellite alloys consists of a tougher and more ductile cobalt solid solution matrix (mainly containing chromium and tungsten or chromium and molybdenum) tangling around dispersed wear-resistant carbides [[1],[2]]. For the microstructures of Stellite alloys, a network of eutectic M_7C_3 carbides surrounds primary face-centred cubic (fcc) cobalt dendrites, in a hypo-eutectic alloy crystal structure at carbon content levels below 2 wt%; while an interdendritic eutectic matrix sandwiches primary M_7C_3 carbides, in a hyper-eutectic alloy crystal structure at carbon

content levels above 2.5 wt% [39]. Solid-solution strengthened alloys are Stellite alloys having very low carbon content of about 0.1 wt% [1].

The carbides in Co-Cr-W-based Stellite alloys are generally of the Cr-rich M_7C_3 type, although in high-tungsten alloys, such as Stellite 3 (30.5%Cr, 12.5%W, 2.4%C, in weight), tungsten-rich M_6C carbides are usually present as well, as shown by the SEM image in Figure 2-9. Superb wear resistance is exhibited by Stellite 3 because its microstructure contains the two types of carbides mentioned above, i.e., primary Cr_7C_3 (in dark) and eutectic $(W,Co)_6C$ (in light). Furthermore, its improved abrasion and solid particle erosion resistance is also associated to its increased carbide volume fraction [2]. Although the high tungsten content makes this alloy very brittle, as found in hardfacing applications, its high-temperature properties are greatly ameliorated. For example, galling was not detected when Stellite 3 was mated with other Stellite alloys at high temperatures [39]. Stellite 3 also exhibited excellent metal-to-metal wear resistance [3]. The microstructure of Stellite 6 (29%Cr, 4.5%W, 1%C, in weight) is shown in Figure 2-10; Cr_7C_3 (dark) carbides having a laminar shape are dispersed in the Co solution matrix. No tungsten-rich M_6C carbides are present in this alloy owing to the lower W content.

In addition, in low-carbon Stellite alloys, the intermetallic compounds of Co_3Mo and $CoMo_6$ may form when Mo content is high, for example, in Stellite 22 and Stellite 28.

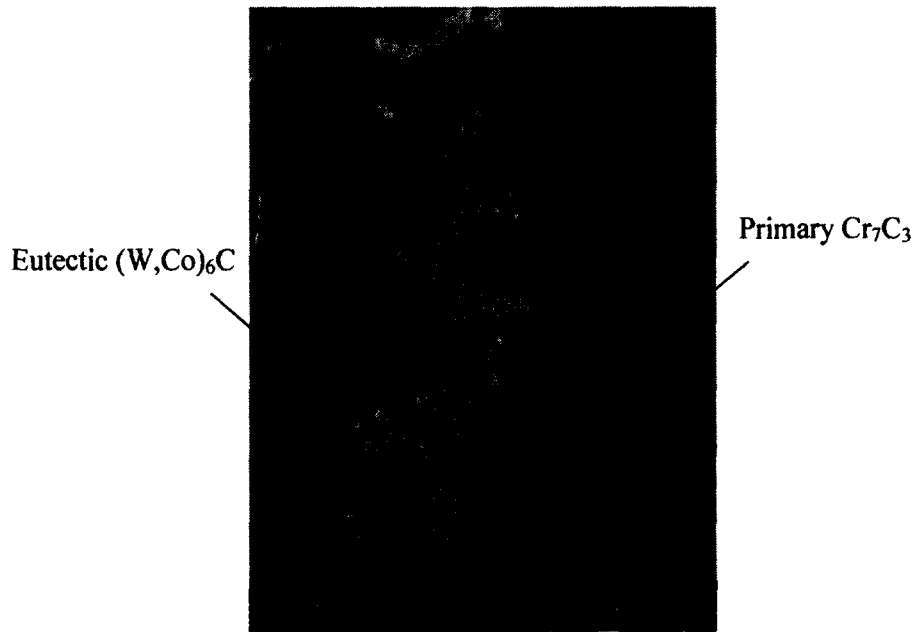


Figure 2-9: SEM microstructure of Stellite 3.

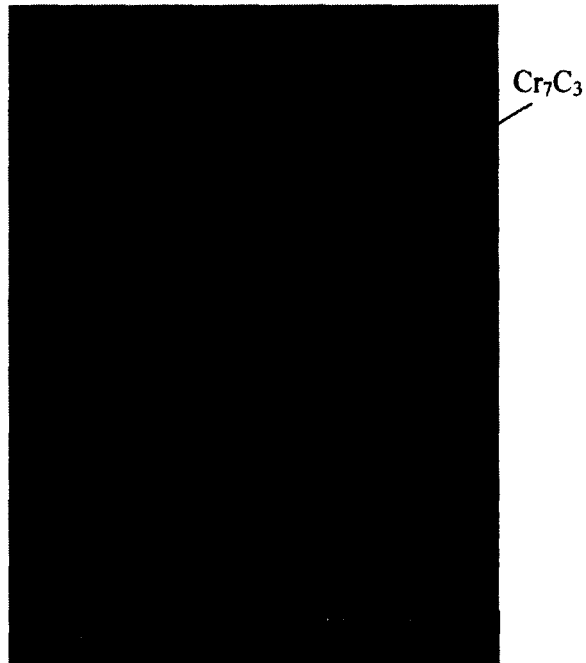


Figure 2-10: SEM microstructure of Stellite 6.

As mentioned earlier, because of the high chromium content, Stellite alloys maintain superior hot corrosion, sulfidation, and oxidation resistance at elevated temperatures [1]. The integration of the crystallographic features of cobalt, the solid-solution-strengthening effects of chromium, tungsten, and molybdenum; the formation of metal carbides, and the corrosion resistance provided by chromium, control the main properties of Stellite alloys [[1],[2],[39]]. Although Stellite alloys are mostly used for wear control, some of them have been encountered in high-temperature applications [3]. For example, Stellite 21 and Stellite 25 possess remarkable sulfidation and hot corrosion resistance in addition to their high strength, and consequently have been employed in high-temperature environments [2]. Finally, the wear resistance of other ferrous or nonferrous alloys is generally lower than that of Stellite alloys [1].

2.4.2 Previous research in erosion of Stellite alloys

With the complex mechanisms of erosion, it is hard to predict the erosion resistance of Stellite alloys, simply based on their chemical composition or single property such as hardness [[5],[6],[15]]. For example, ductility, for Stellite alloys, can also be a major parameter governing their solid-particle erosion behavior [2]. As reported in literature, most studies in the erosion behavior of Stellite alloys were experiment-based [5]. For instance, cavitation erosion behaviour of Stellite 3, Stellite 6 and Stellite 20 was investigated by Heathcock *et al.* [40]. The experimental results showed that Stellite 3 had the highest resistance to erosion; Stellite 6 had the lowest and Stellite 20 had a similar erosion resistance to Stellite 6, as illustrated in Figure 2-11. The studies of erosion behaviour and mechanisms of various superalloys were also

reported [[41]-[50]]. In these studies, the solid particle erosion of nickel-based Inconel 625 and Inconel 600 at elevated temperatures was investigated; two heat-treated alloys, namely cobalt-based Haynes 188 and nickel-based Waspaloy were also studied in a vertical sand-blast type of test rig with specimen temperature changed in steps [[41]-[50]]. The influences of various erosion parameters including particle velocity, impact angle, particle size and particle concentration etc., were investigated or analyzed [[41]-[50]]. Analytical simulation of erosion process was performed and the mechanism was examined with emphasis on the interaction of oxidation and erosion of superalloys at high temperatures [[41]-[50]].

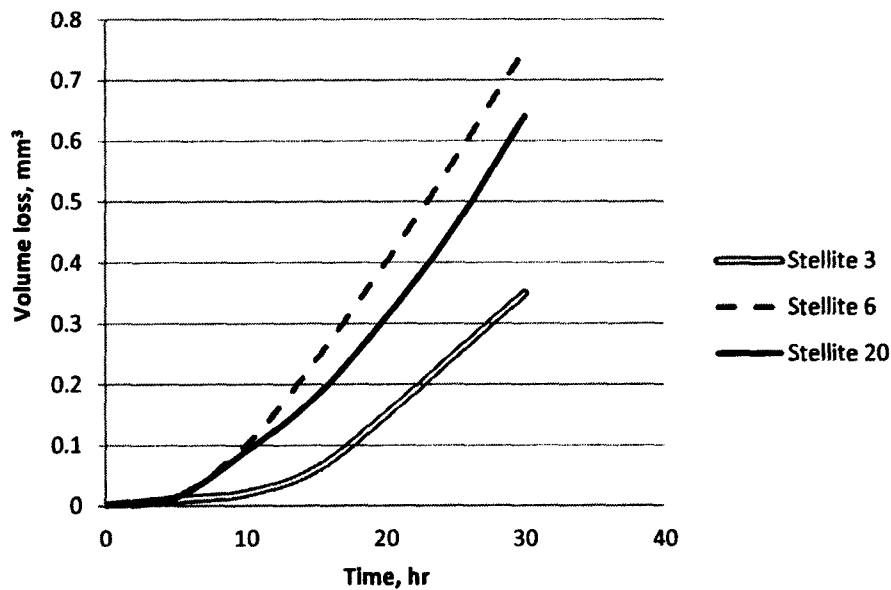


Figure 2-11: Erosion curves of Stellite alloys [40].

However, due to the complexity of testing procedures and the multiplicity of affecting factors, as well as long testing duration, the studies of erosion

resistance/mechanisms for Stellite alloys have been very limited [[5],[40]-[50]]. The results obtained tend to be very sensitive to the operating conditions, which have limited the application, improvement and design of Stellite alloys [[5],[40]-[50]]. Therefore it is necessary to further perform erosion evaluation experimentally and analytically on these alloys, from which the mechanisms that govern the erosion process can be identified to mitigate or reduce the material degradation due to erosion.

3 Chapter: Microstructural Characterization

3.1 Test Specimens

3.1.1 Alloy selection

Stellite alloys are generally classified into three main categories: (1) high-carbon Stellite alloys designed for wear service; (2) medium-carbon Stellite alloys used for high temperature service; and (3) low-carbon Stellite alloys used against corrosion or simultaneous corrosion and wear [1]. Therefore, the alloys studied in this research were carefully selected to broadly cover the last two categories, according to the application of Stellite alloys for erosion resistance. Five Stellite alloys were selected purposefully in consideration of chemical compositions. Understanding the function of the elements involved in Stellite alloys is an initial important or fundamental step to understand the basis of material properties. Carbon, in steels and alloys, increases hardness while increasing brittleness [1]. Carbon increases hardness normally by forming carbides, which through dispersion and solid solution strengthening, prevent slipping in the atomic crystal lattice [[1],[22]]. Three important alloying elements that need to be specifically addressed are molybdenum, tungsten and chromium as these elements play important roles in governing the material properties; and their contents vary among Stellite alloys. Molybdenum has half the atomic mass of tungsten, thus for the same weight percentage, there will be an excessive atomic concentration of molybdenum compared to tungsten [4]. Because of this, the tendency for molybdenum-rich carbides to form is higher [4]. As discussed previously, the main role of both tungsten and molybdenum in Stellite alloys is attributed to their solid-solution strengthening [1]. The overall corrosion resistance of Stellite alloys is also improved by these two elements (tungsten and

molybdenum) [1]. When tungsten is present in large amounts, it contributes to carbide formation [1], as in the case of Stellite 1 and Stellite 3, where $(W,Co)_6C$ carbide is formed. Similarly, when present in large quantities, molybdenum participates and promotes the formation of two inter-metallic compounds of Co_3Mo and $CoMo_6$, for example, in Stellite 22 and Stellite 28. Chromium improves the resistance to corrosion and oxidation and is also the main carbide former [1]. As hardness and erosion resistance are major considerations for the Stellite alloys being studied in this research, the performance of these elements is certainly a major concern in the alloy selection.

Firstly considering carbon, it is a very important element, making the carbide volume fraction in Stellite alloys a critical parameter [1]. These alloys contain different levels of carbon and are identified as low-, and medium-carbon Stellite alloy. The reason why high-carbon Stellite alloys were not selected for this research is that, as explained previously in Chapter 2, in solid-particle erosion, ductility, for Stellite alloys, can also be a major parameter governing their solid-particle erosion behavior [2]. High-carbon Stellite alloys are more brittle and less ductile, which are generally not used for erosion resistance but for abrasive wear and sliding wear resistance [4]. Secondly, considering the main strengthening element in solid solution, tungsten, these alloys were selected to contain varying levels of tungsten, from zero up to a maximum of 30 wt%. Thirdly, considering another strengthening element in solid solution, molybdenum, these alloys were selected to contain varying levels of molybdenum, from zero up to a maximum of 11 wt%. Finally, as the main element of carbide formation, chromium, takes 20 ~ 30 wt% in Stellite alloys. Other elements such as nickel, iron, silicon, and so on were also taken into account. From these considerations of chemical composition, the effects of main

constituents of Stellite alloys on the hardness and erosion resistance of these alloys would be investigated in this research, in particular, on the hardness and erosion resistance of Stellite alloys at room temperature.

3.1.2 Chemical compositions

The chemical compositions (wt%) of the five alloys being studied are detailed in Table 3-1. For convenience, the selected five alloys were designated as alloy A, alloy B, alloy C, alloy D, and alloy E, respectively. These alloys have a carbon content between 0.25 ~ 1.6%, chromium content between 22 ~ 30%, tungsten content between 4 ~ 32% except alloy D and alloy E which do not contain tungsten. These two alloys contain the least carbon contents of 0.35% and 0.25% and the highest molybdenum contents of 11.8% and 11%, respectively. This group of Stellite alloys also contain small amounts of nickel between 2.5 ~ 3.8%, iron between 1 ~ 3%, silicon between 0.45 ~ 2%, and manganese between 0.52 ~ 2%, except alloy B. Alloy A, alloy B and alloy C belong to medium-carbon Stellite alloys while alloy D and alloy E fall into low-carbon Stellite alloys. Alloy A contains the highest amount of carbon, followed by an order of alloy B, alloy C, alloy D and alloy E. Alloy D further contains an additional 2.07% of niobium used to improve the high temperature performance [4]. Among these alloys, alloy A and alloy C are conventional wrought Stellite alloys, known as Stellite 6K and Stellite 6B, respectively, which have been widely applied in various industries involving wear and erosion environments. Stellite 6B, for instance, has been used for erosive wear resistance in the ongoing efforts in coal conservation. The remaining three alloys were newly developed at Kennametal Stellite Inc. Alloy B is designated as Stellite 300; alloy D and

alloy E are Stellite 28 and Stellite 22, respectively. Stellite 300, Stellite 28 and Stellite 22 are cast products.

Table 3-1: Chemical compositions (wt%, Co in balance) of Stellite alloys

Element Specimen	Cr	W	Mo	C	Fe	Ni	Si	Mn	Others
Alloy A	30	4.5	1.5	1.6	3	3	2	2	
Alloy B	22	32	0	1.5	0	0	0	0	
Alloy C	30	4	1.5	1	3	2.5	0.7	1.4	
Alloy D	24.2	0	11.8	0.35	1	3.8	0.45	0.52	2.07Nb
Alloy E	27	0	11	0.25	3	2.75	1	1	

3.2 Microstructural Analysis

3.2.1 Specimen preparation

To study the hardness and erosion performance of Stellite alloys, especially, the effects of their chemical compositions on these properties, it is necessary to understand their microstructures first, because chemical composition determines the microstructure of a material. Definitely, the fabrication process also plays an important role in controlling the microstructure which would eventually affect the final properties of the material or product. Therefore, the microstructures of the five alloys being studied were investigated prior to hardness and erosion tests.

The preparation of the specimens for microstructural analysis followed the steps below:

- (1) Cut the metallographic specimens from the main body of the cast materials to approximate dimensions of $45 \times 60 \times 5$ mm using a cutting machine of Struers Co. (Secotom-10), shown in Figure 3-1, with an Al_2O_3 abrasive cut-off blade. The dimensions stated above are not a fixed standard; they could be altered depending on the mounting press and purpose. Care was taken to minimize excessive heating by employing cutting parameters of 1500 rpm spindle speed and 0.03 mm/s specimen advancing speed and also by following the usual precautions such as proper cooling conditions to avoid any microstructure alteration.

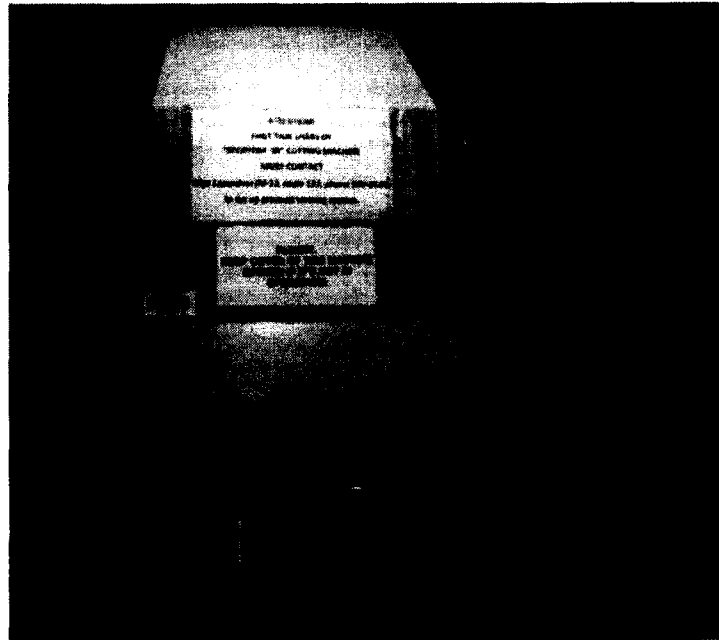


Figure 3-1: Secotom-10 cutting machine (Courtesy of Struers Co.).

- (2) The specimens were mounted by encapsulating into a compression mounting compound. The compound was a phenolic plastic. The hot mounting press of Struers Co. (laboPress-3), shown in Figure 3-2, with adjustable pressing parameters such as

heating temperature, heating time, cooling time, and force, was used to provide heat (150°C ~ 180°C) and force (~ 50 MPa) for mounting.

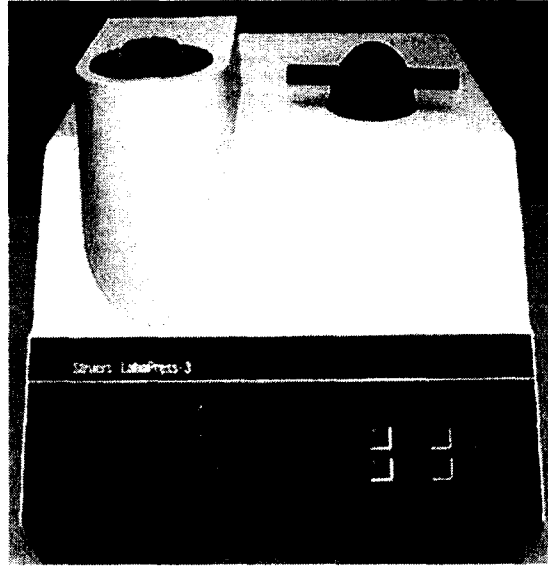


Figure 3-2: LaboPress-3 mounting press (Courtesy of Struers Co.).

- (3) Grind the surfaces of the specimens. The operations were performed automatically by a Buehler Ecomet-IV semi-automatic grinder, shown in Figure 3-3. The specimen holder of the machine is a fixed frame in which the pressure is applied on the specimens via the central column of the holder. Therefore, it is necessary to place the specimens symmetrically in order to obtain flat surfaces after grinding operation. Grinding operation was required to remove the surface layer of the cast products and also reduce the surface damage caused by cutting. A 320 standard grit size of silicon carbide (SiC) abrasive paper was used with the operation parameters: a contact head pressure of 20 psi and a spindle speed of 200 rpm. The selection of these parameters

depended on the hardness of materials. Water was used as the coolant to reduce the generated friction heat during grinding.

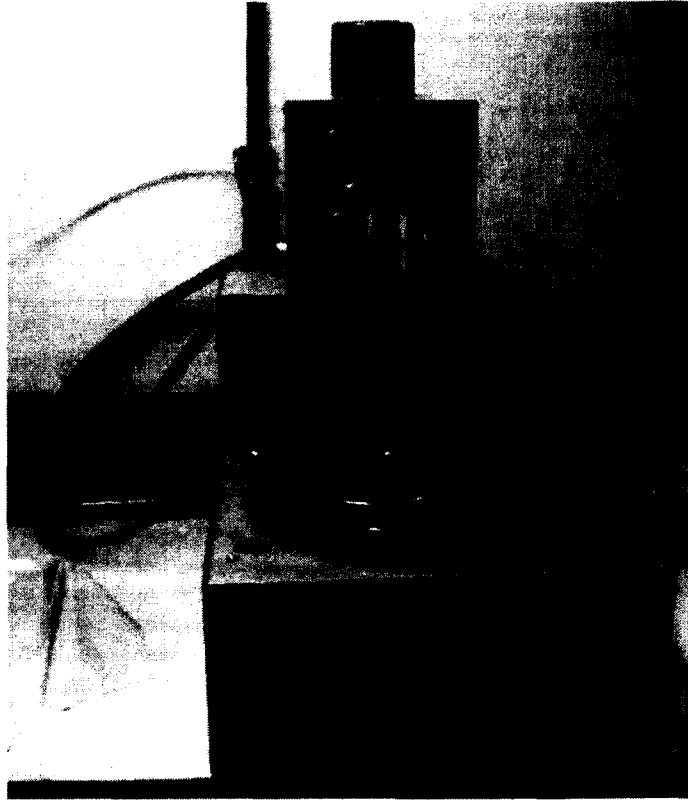


Figure 3-3: Buehler Ecomet-IV semi-automatic grinder polisher.

- (4) Polish the surfaces of the specimens. The purpose of polishing operation was to produce a specularly reflecting or bright mirror-like surface. The polishing operation included rough and final polishing steps. Rough polishing was performed to remove the damage produced during planar grinding. The specimens were roughly polished with sequentially decreasing abrasive paper grit sizes. In the next stage, the specimen surfaces were lightly polished with 3 μm diamond suspension and 1 μm alumina suspension on two specific polishing pads. For the final polishing stage, colloidal

silica suspension was used on a third specific polishing pad for 15 min. This helps to better reveal the microstructure of the specimens. The specimens were thoroughly cleaned in an ultrasonic bath, prior and after each step of the final polishing since surface quality could be degraded by abrasion from the debris produced during polishing.

- (5) Etch the specimen surfaces. After polishing, the specimen surfaces were subjected to electrolytic and immersion etching with the solution mixture of 2 ~ 10 g CrO_3 in 100 ml H_2O . The etching operations were performed using a Buehler Electromet etcher and the apparatus setup is shown in Figure 3-4.

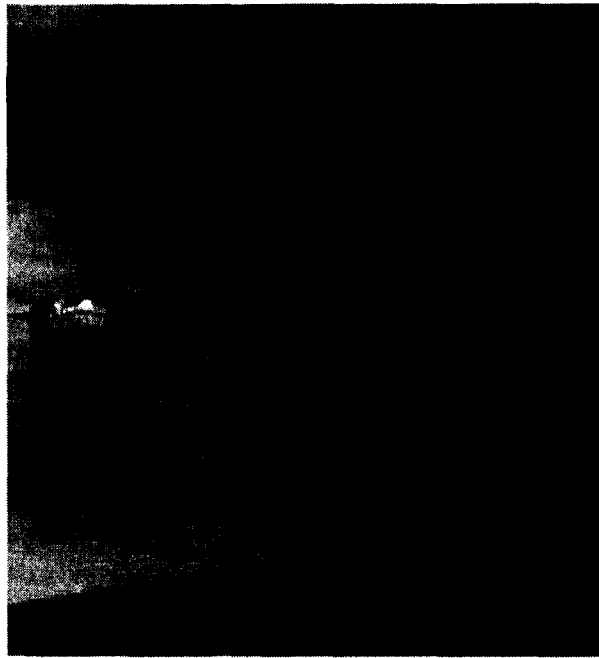


Figure 3-4: Apparatus setup with the Buehler Electromet etcher.

3.2.2 Microstructure examination

The microstructure analysis of the alloy specimens was performed on a Hitachi Model S-570 Scanning Electron Microscope (SEM) with backscatter electron imaging (BEI) and energy dispersive X-ray (EDX) spectrum, shown in Figure 3-5 and on a TESCAN Scanning Electron Microscope (SEM) with an EDAX energy dispersive X-ray (EDX) spectroscopy system, shown in Figure 3-6. These two SEM systems are similar, but the latter is able to identify nonmetallic elements such as carbon, silicon, boron, etc. in the EDX analysis, providing more accurate analysis for phases present in a microstructure. However, the detection of carbon is inaccurate by this instrument; therefore the tables presented below contain only the metallic elements for each phase.

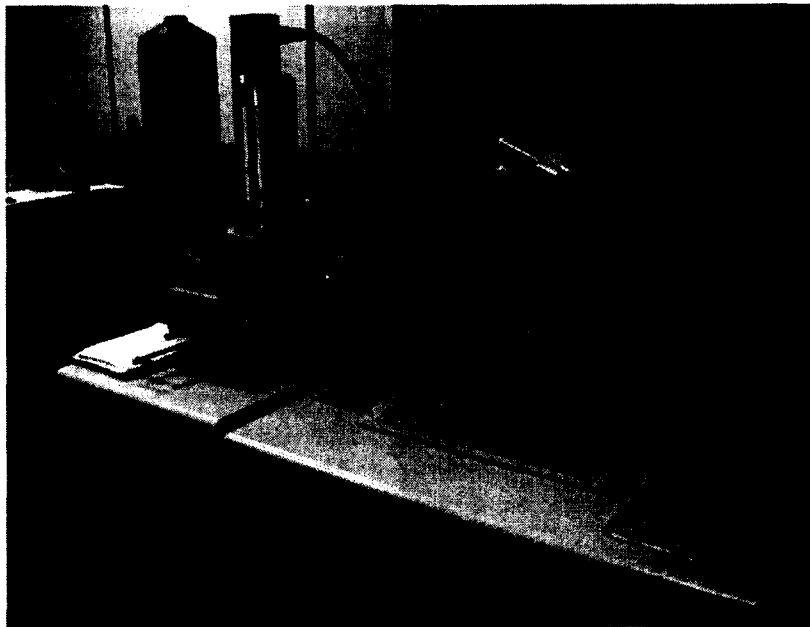


Figure 3-5: Hitachi Model S-570 Scanning Electron Microscope (SEM) with energy dispersive X-ray (EDX) spectrum.

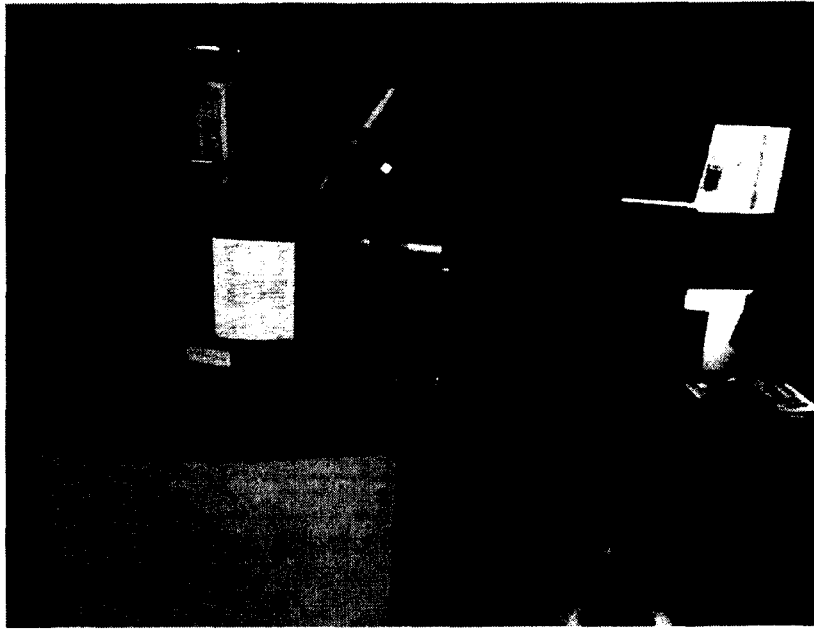
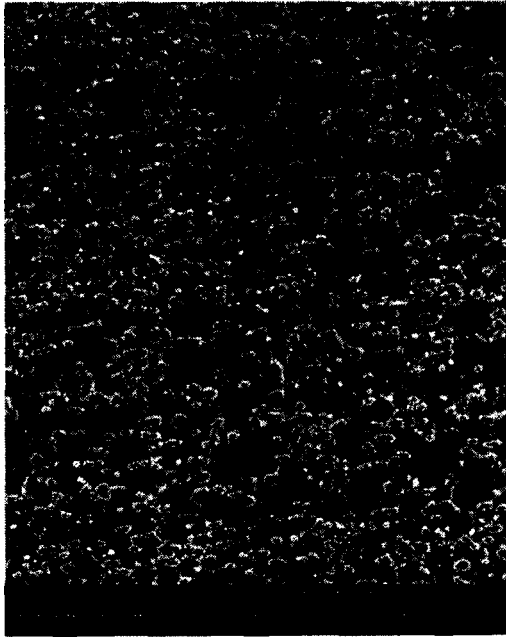


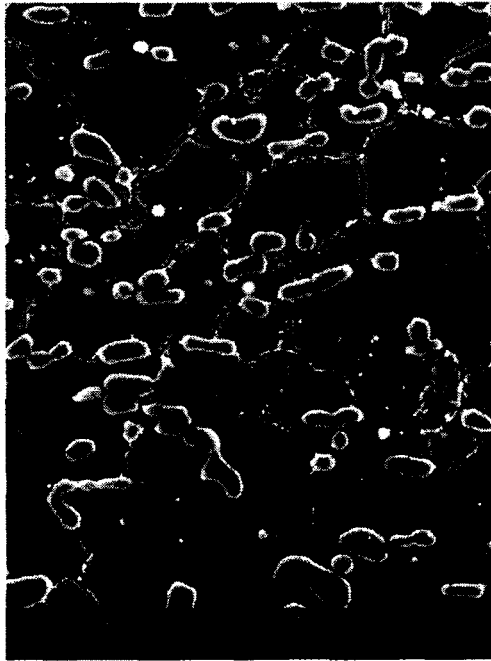
Figure 3-6: TESCAN Scanning Electron Microscope.

3.2.3 SEM images of microstructure

The SEM images of microstructures of the five alloys at low and high magnifications are presented in Figure 3-7 to Figure 3-11. Stellite alloys have a microstructure typically consisting of complex hard carbides (mostly chromium-rich carbides) dispersed in a tough cobalt solid solution matrix mainly containing chromium and tungsten or chromium and molybdenum. Carbon is a very important element, making the carbide volume fraction in Stellite alloys a critical parameter [1]. Due to the presence of carbides, Stellite alloys are generally brittle. However, low carbon content may improve the ductility of Stellite alloys. Although other constituents such as tungsten or molybdenum affect the microstructure of Stellite alloys, the carbon content generally determines the microstructure being either hypo-eutectic or hyper-eutectic [1].



(a)

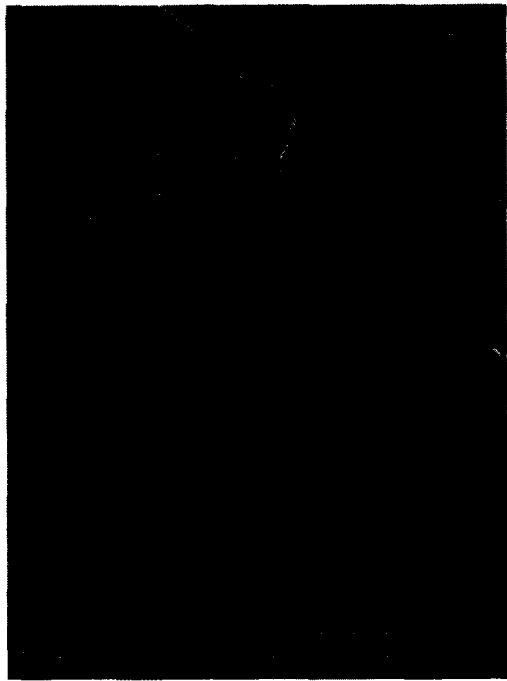


(b)

Figure 3-7: SEM microstructure of alloy A: (a) at low magnification and (b) at high magnification.



(a)



(b)

Figure 3-8: SEM microstructure of alloy B: (a) at low magnification and (b) at high magnification.

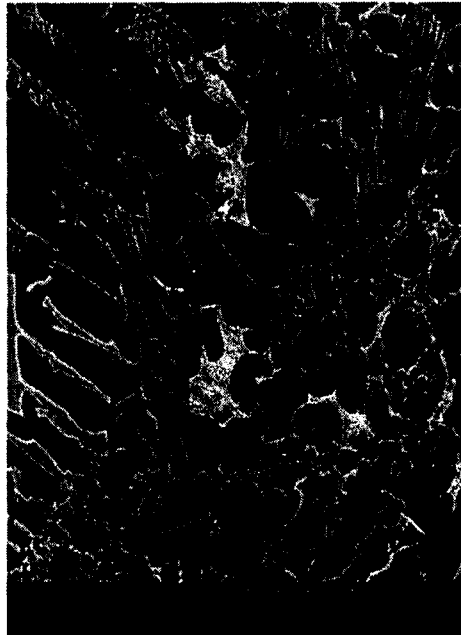


(a)



(b)

Figure 3-9: SEM microstructure of alloy C: (a) at low magnification and (b) at high magnification.

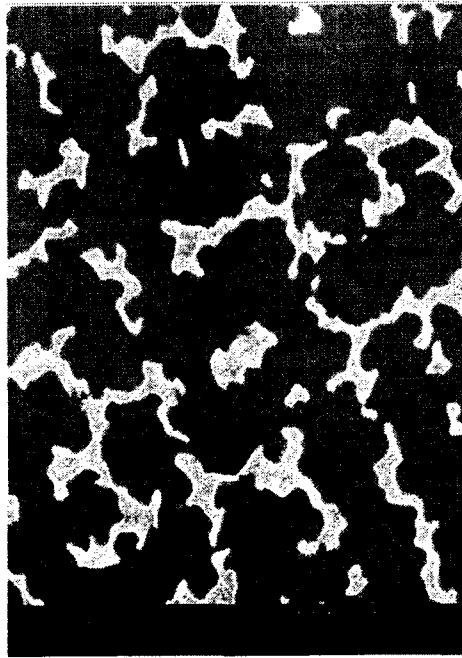


(a)



(b)

Figure 3-10: SEM microstructure of alloy D: (a) at low magnification and (b) at high magnification.



(a)



(b)

Figure 3-11: SEM microstructure of alloy E: (a) at low magnification and (b) at high magnification.

The microstructures of each alloy are discussed in details as follows, according to the EDX results in Figure 3-12 to Figure 3-27. The unusual black spots on some images are merely defects from the polishing stage. These spots are very visible in Figure 3-22 and Figure 3-25. In Table 3-2 to Table 3-12, Wt % and At % stand for weight percent and atomic percent respectively.

Alloy A

This alloy has a microstructure consisting of two phases, as shown in Figure 3-12. It contains a medium carbon content that increases the volume fraction of carbides. The primary Co solid solution (location 1, grey) contains very high Co and also high Cr, as illustrated in Figure 3-13 and Table 3-2. The eutectic carbide phase Cr_7C_3 (location 2, dark) is dispersed in the Co solid solution matrix. The EDX results in Figure 3-14 and Table 3-3 show that the Cr_7C_3 carbide phase contains very high Cr. The tungsten which is detected in Table 3-2 and Table 3-3 enhances the strength of this alloy; it also improves the high-temperature properties [1].

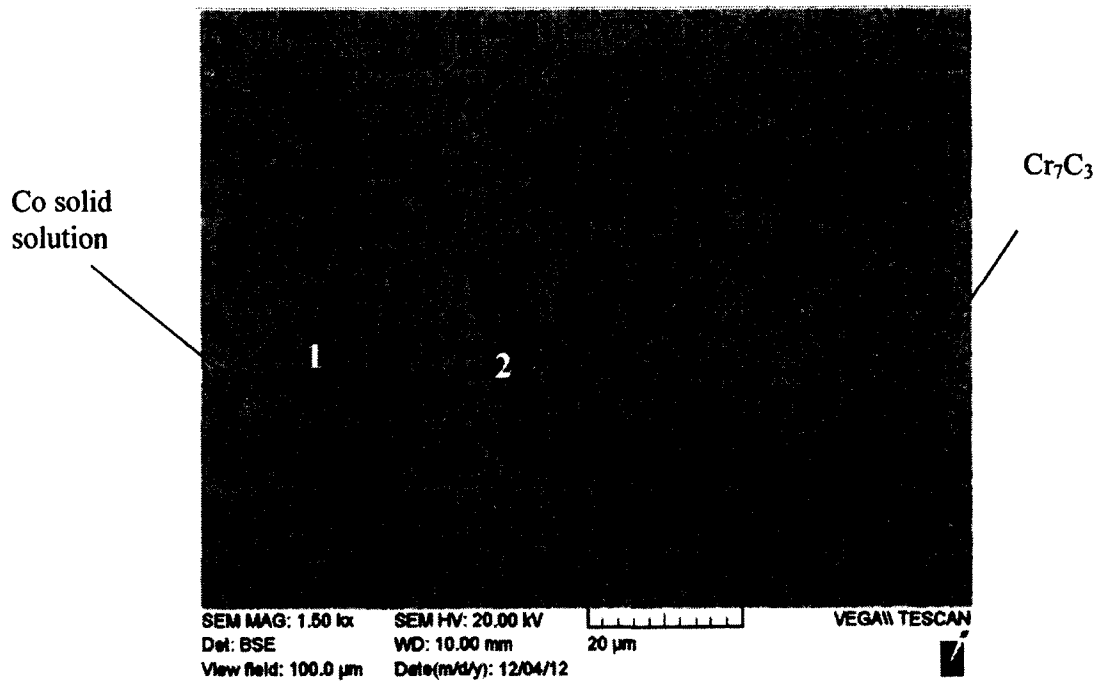


Figure 3-12: SEM microstructure of alloy A with phases indicated for EDX analysis.

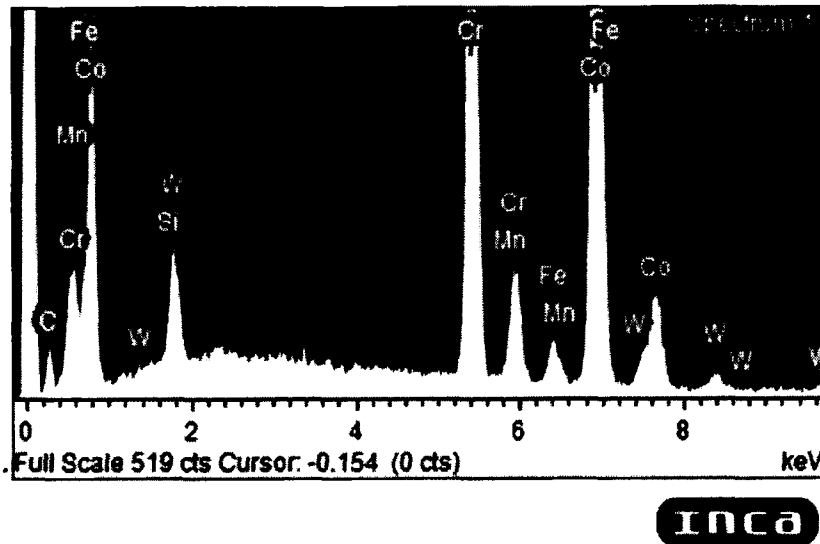


Figure 3-13: EDX spectrum of location 1 for alloy A.

Table 3-2: Metallic element table of location 1 for alloy A

Element	Wt %	At %
Si K	0.87	1.79
Cr K	30.90	34.28
Mn K	1.48	1.55
Fe K	2.68	2.76
Co K	59.43	58.17
W M	4.65	1.45
Total	100	100

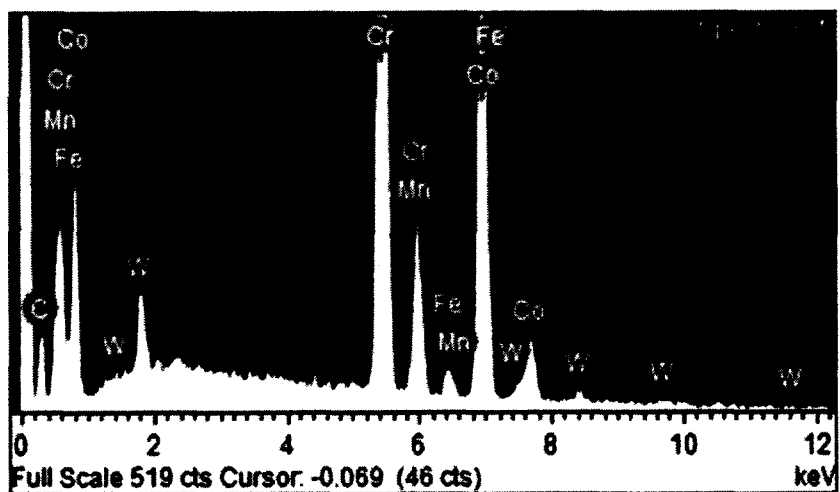


Figure 3-14: EDX spectrum of location 2 for alloy A.

Table 3-3: Metallic element table of location 2 for alloy A

Element	Wt %	At %
Cr K	53.39	57.99
Mn K	1.53	1.57
Fe K	2.06	2.08
Co K	38.64	37.02
W M	4.39	1.35
Total	100	100

Alloy B

This alloy has a microstructure containing three phases, as shown in Figure 3-15. It also has a medium carbon content that increases the volume fraction of carbides. Due to the high content of W, this alloy has primary $(W,Co)_6C$ carbide (location 1, light) that contains very high W and also high Co, as illustrated in Figure 3-16 and Table 3-4. The eutectic Co solid solution (location 2, grey) and carbide phase Cr_7C_3 (location 3, dark) contain very high Co and Cr, respectively, as shown by the EDX results in Figure 3-17, Figure 3-18, Table 3-5 and Table 3-6.

Tungsten enhances the strength of Stellite alloys and when tungsten is present in large amounts, it contributes to $(W,Co)_6C$ carbide formation. This microstructure is hyper-eutectic.

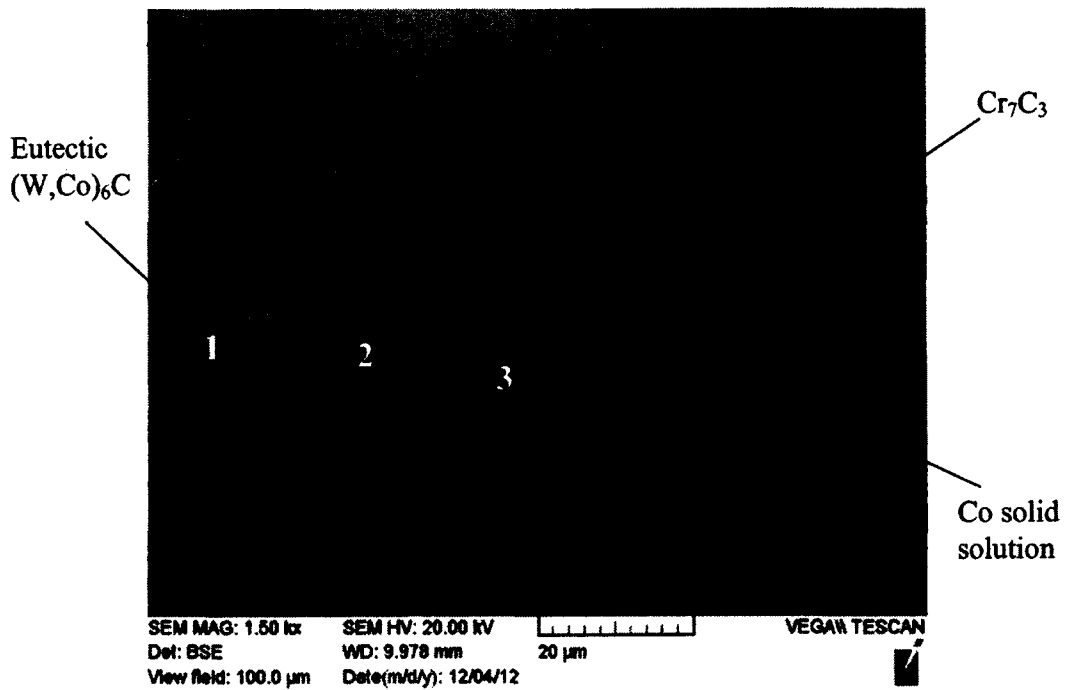


Figure 3-15: SEM microstructure of alloy B with phases indicated for EDX analysis.

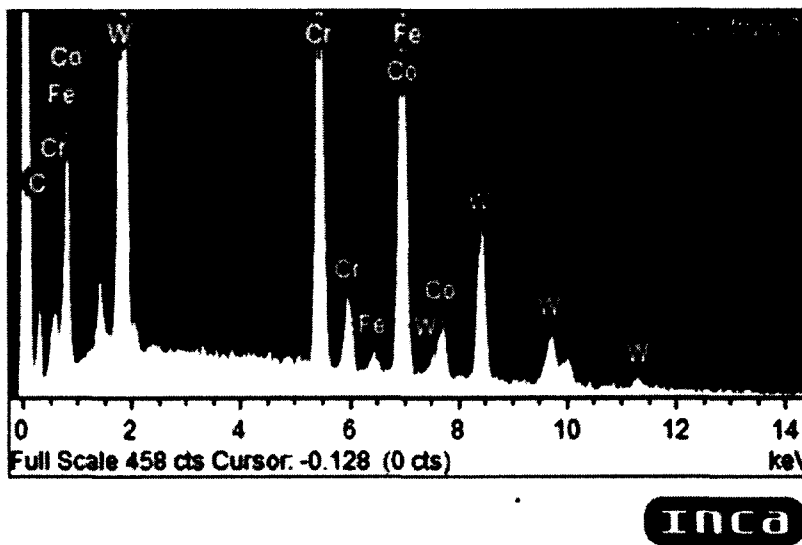


Figure 3-16: EDX spectrum of location 1 for alloy B.

Table 3-4: Metallic element table of location 1 for alloy B

Element	Wt %	At %
Cr K	21.48	34.44
Fe K	1.01	1.51
Co K	30.07	42.54
W M	47.44	21.50
Total	100	100

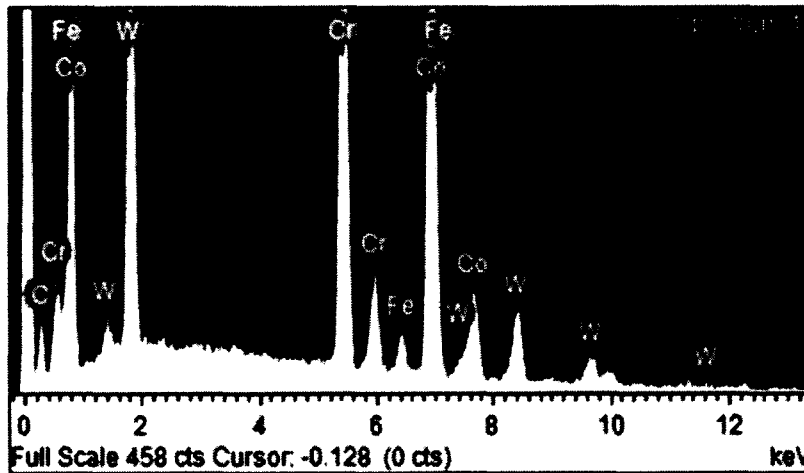


Figure 3-17: EDX spectrum of location 2 for alloy B.

Table 3-5: Metallic element table of location 2 for alloy B

Element	Wt %	At %
Cr K	25.36	33.17
Fe K	2.20	2.68
Co K	47.62	54.96
W M	24.82	9.19
Total	100	100

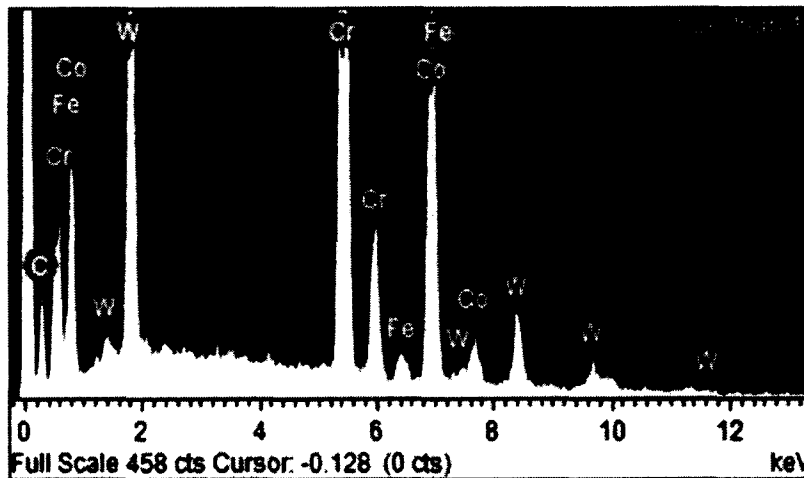


Figure 3-18: EDX spectrum of location 3 for alloy B.

Table 3-6: Metallic element table of location 3 for alloy B

Element	Wt %	At %
Cr K	45.52	56.83
Fe K	1.51	1.76
Co K	30.35	33.42
W M	22.62	8.00
Total	100	100

Alloy C

Similar to alloy A, this alloy also has a microstructure consisting of two phases, as shown in Figure 3-19. But it contains much less carbon content than alloy A thus a lower volume fraction of carbides. Same as alloy A, the primary Co solid solution (location 1, grey) contains very high Co and also high Cr, as illustrated in Figure 3-20 and Table 3-7. The eutectic carbide phase Cr_7C_3 (location 2, dark) is dispersed in the Co solid solution matrix. The EDX results in Figure 3-21 and Table 3-8 show that the Cr_7C_3 carbide phase contains very high Cr. The tungsten which is detected in Table 3-7 and Table 3-8 enhances the strength of this alloy [1]. Comparing the microstructures of these two wrought Stellite alloys in Figure 3-7 and Figure 3-9, the carbide size of alloy C is larger.

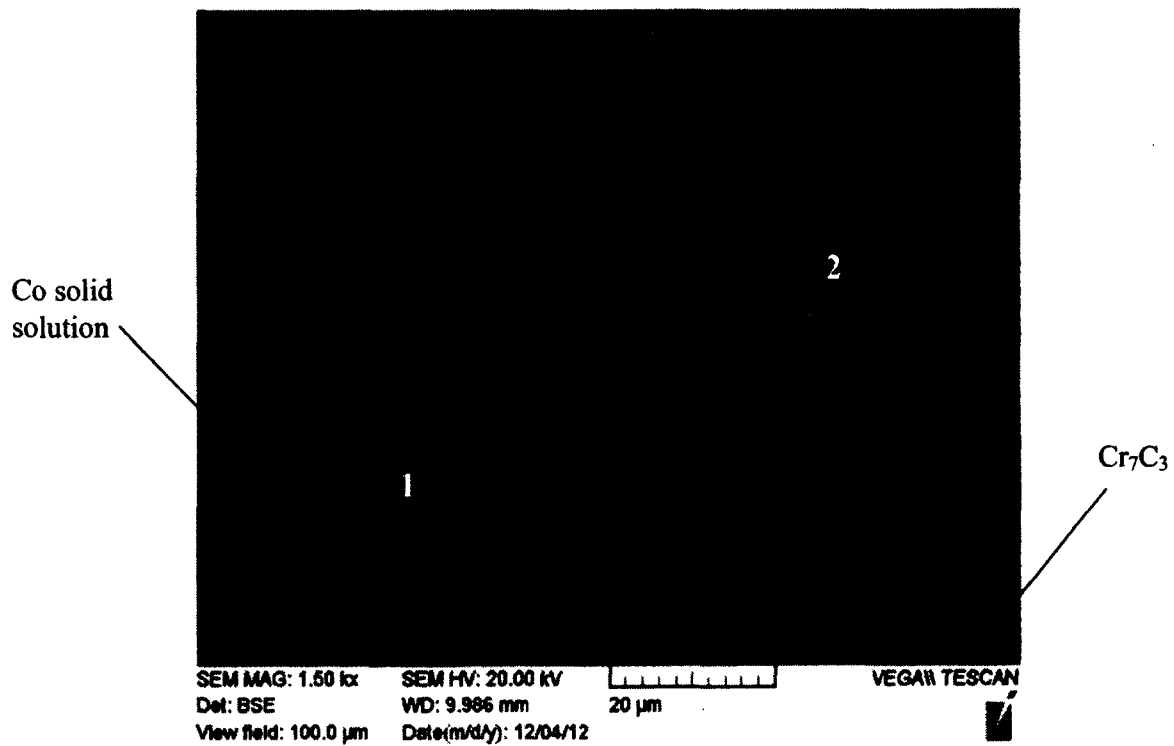


Figure 3-19: SEM microstructure of alloy C with phases indicated for EDX analysis.

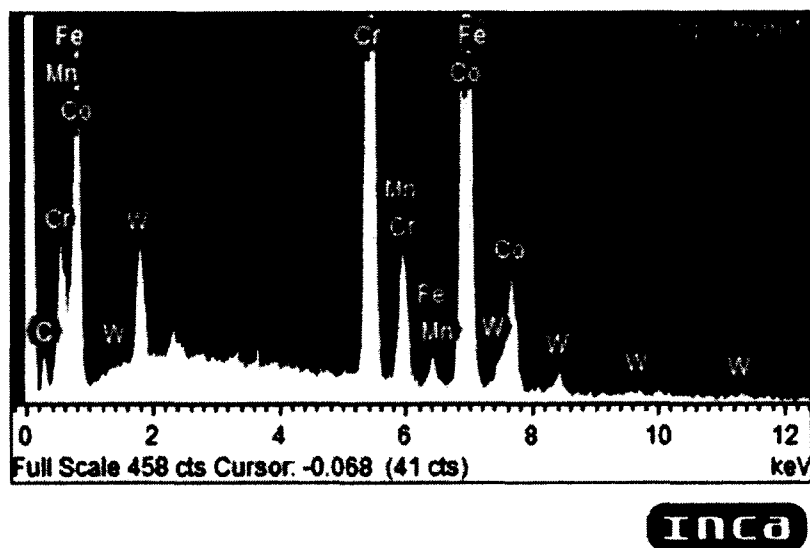


Figure 3-20: EDX spectrum of location 1 for alloy C.

Table 3-7: Metallic element table of location 1 for alloy C

Element	Wt %	At %
Cr K	30.19	34.08
Mn K	1.86	1.99
Fe K	1.53	1.61
Co K	60.78	60.53
W M	5.64	1.80
Total	100	100

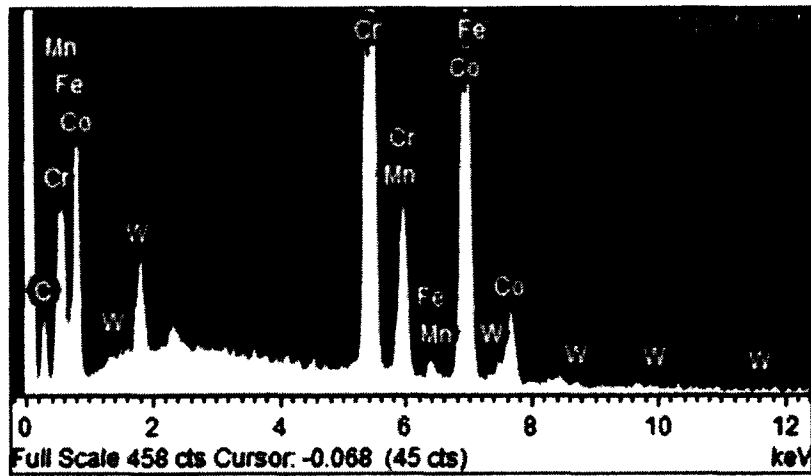


Figure 3-21: EDX spectrum of location 2 for alloy C.

Table 3-8: Metallic element table of location 2 for alloy C

Element	Wt %	At %
Cr K	52.78	57.30
Mn K	1.35	1.39
Fe K	1.12	1.15
Co K	40.59	38.89
W M	4.16	1.28
Total	100	100

Alloy D

This alloy contains a very low level of C thus a small volume fraction of carbides. According to the SEM images, this alloy has a microstructure consisting of two phases, as labeled in Figure 3-22. Molybdenum enhances the strength of Stellite alloys, but when present in large quantities, it participates and promotes the formation of two inter-metallic compounds of Co_3Mo and CoMo_6 . This microstructure is hypo-eutectic. From the EDX spectrum and the associated metallic element contents in Figure 3-23 and Table 3-9, location 1 (grey) is the primary Co solid solution, containing very high Co and also high Cr. Location 2 (light) is the mixture of Cr_7C_3 carbide and the intermetallic compounds of Co_3Mo and CoMo_6 , because this area has a high concentration of Cr, Co and Mo, as demonstrated by the EDX results in Figure 3-24 and Table 3-10.

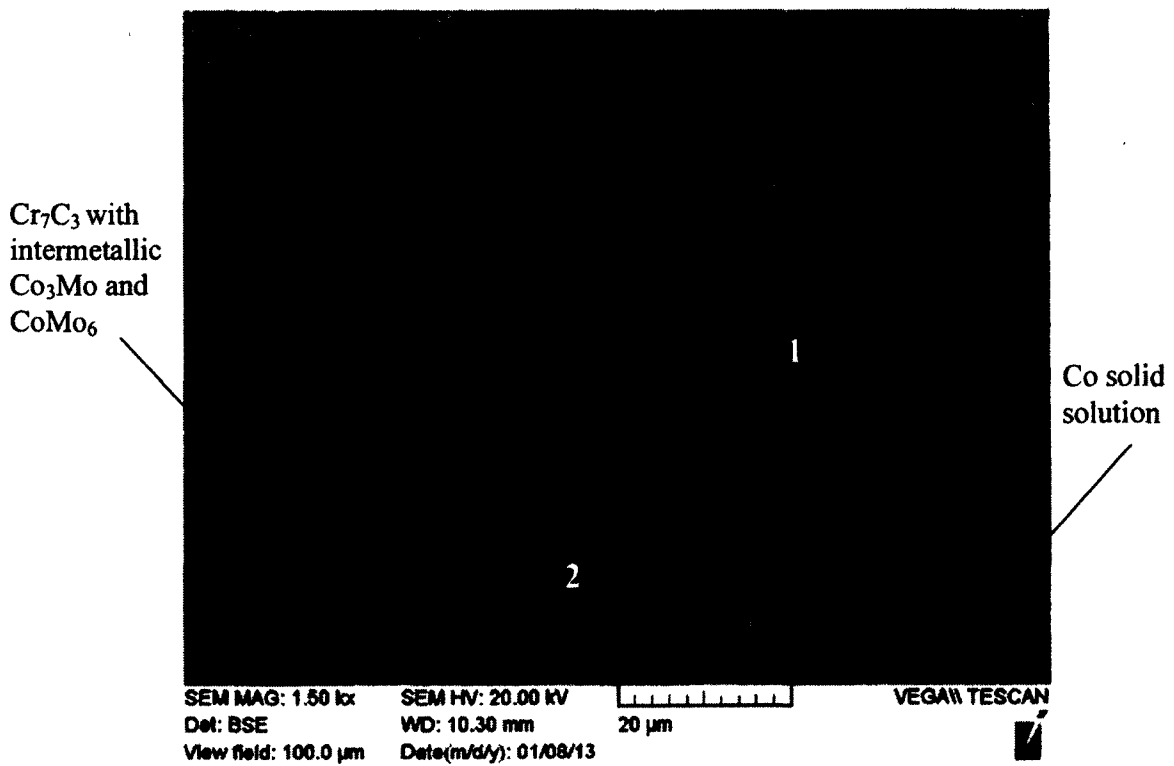


Figure 3-22: SEM microstructure of alloy D with phases indicated for EDX analysis.

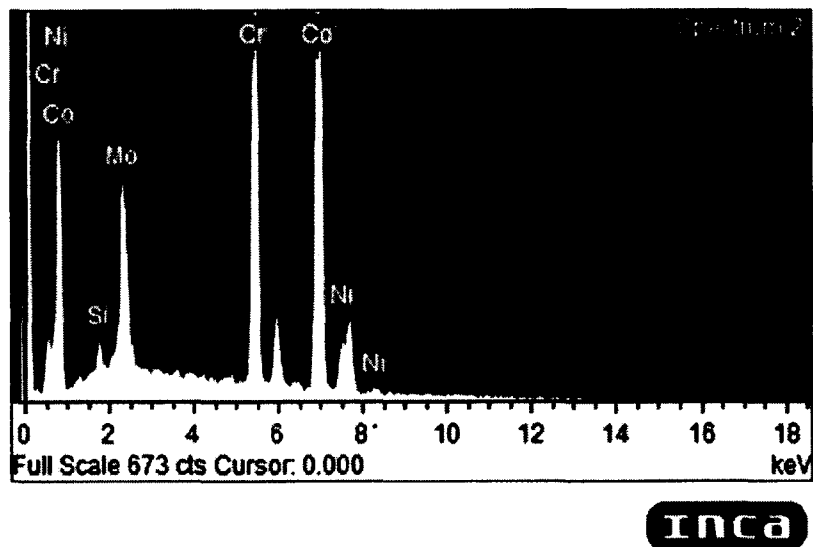


Figure 3-23: EDX spectrum of location 1 for alloy D.

Table 3-9: Metallic element table of location 1 for alloy D

Element	Wt %	At %
Si K	0.87	1.83
Cr K	26.65	30.13
Co K	56.67	56.53
Ni K	4.69	4.70
Mo L	11.12	6.81
Total	100	100

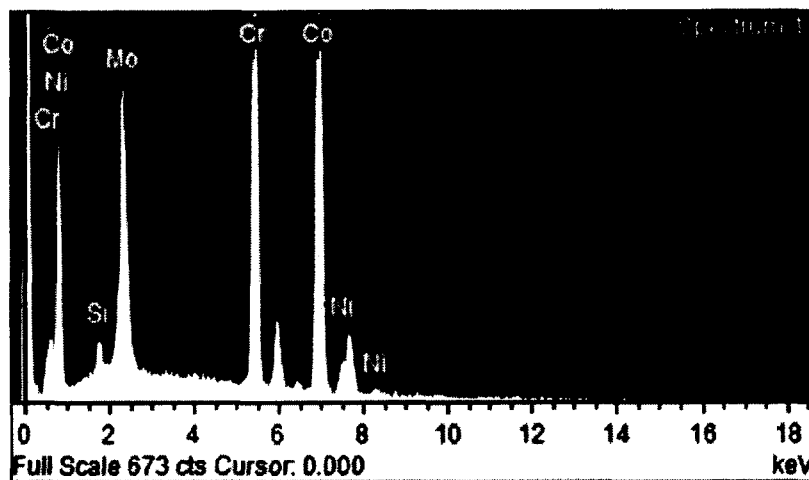


Figure 3-24: EDX spectrum of location 2 for alloy D.

Table 3-10: Metallic element table of location 2 for alloy D

Element	Wt %	At %
Si K	1.04	2.22
Cr K	27.62	31.73
Co K	51.40	52.11
Ni K	3.83	3.90
Mo L	16.11	10.04
Total	100	100

Alloy E

Since alloy E has a similar chemical composition to alloy D, these two alloys have a similar microstructure. They both contain a very low level of C thus a small volume fraction of carbides, but the latter contains less C. According to the SEM images, this alloy has a microstructure consisting of two phases, as labeled in Figure 3-25. Molybdenum enhances the strength of Stellite alloys, but when present in large quantities, it participates and promotes the formation of two intermetallic compounds of Co_3Mo and CoMo_6 . This microstructure is hypo-eutectic. From the EDX spectrum and the associated metallic element contents in Figure 3-26 and Table 3-11, location 1 (grey) is the primary Co solid solution, containing very high Co and also high Cr. Location 2 (light) is the mixture of Cr_7C_3 carbide and the inter-metallic compounds of Co_3Mo and CoMo_6 , because this area has high concentrations of Cr, Co and Mo, as demonstrated by the EDX results in Figure 3-27 and Table 3-12.

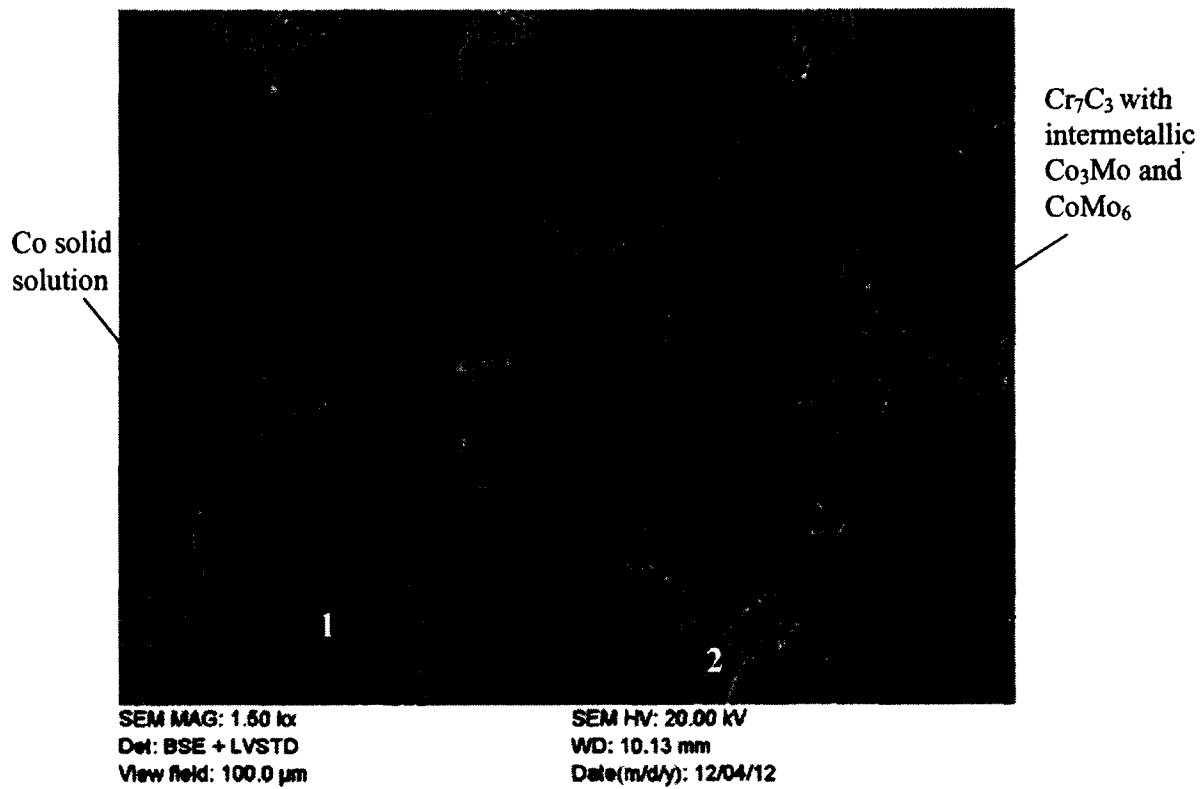


Figure 3-25: SEM microstructure of alloy E with phases indicated for EDX analysis.

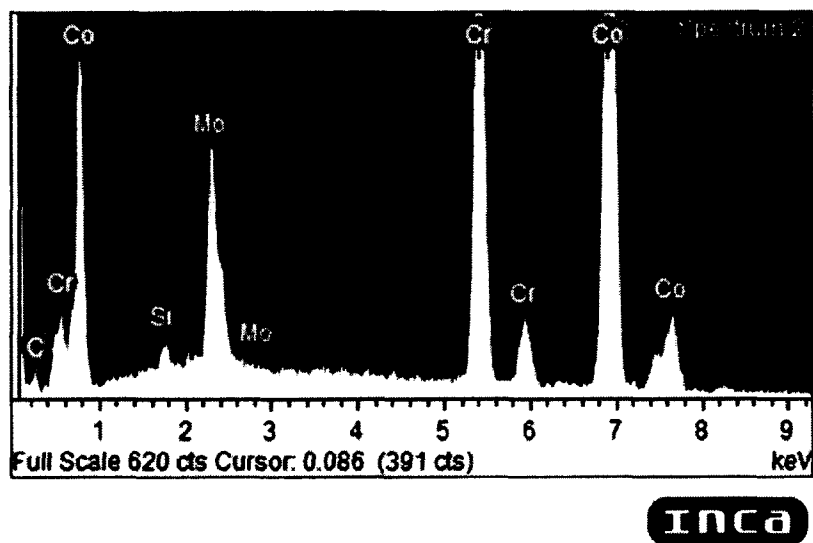


Figure 3-26: EDX spectrum of location 1 for alloy E.

Table 3-11: Metallic element table of location 1 for alloy E

Element	Wt %	At %
Si K	0.57	1.21
Cr K	27.37	31.24
Co K	59.08	59.51
Mo L	12.98	8.04
Total	100	100

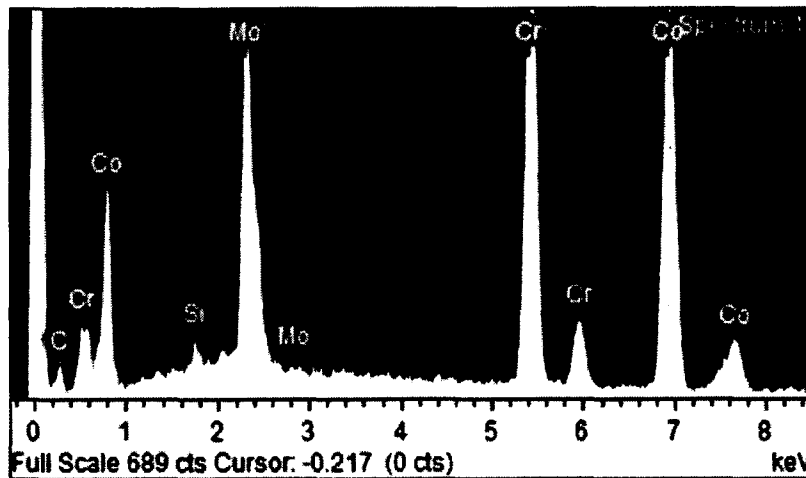


Figure 3-27: EDX spectrum of location 2 for alloy E.

Table 3-12: Metallic element table of location 2 for alloy E

Element	Wt %	At %
Si K	0.54	1.18
Cr K	31.42	37.04
Co K	45.63	47.46
Mo L	22.40	14.32
Total	100	100

4 Chapter: Erosion Test

4.1 Experimental Preparation

4.1.1 Testing specimens

The testing specimens of the five Stellite alloys, designated as alloy A, alloy B, alloy C, alloy D and alloy E, were supplied by Kennametal Stellite Inc. The specimen of Alloy A was a rectangular block of $3 \times 1 \times 0.125$ in, as shown in Figure 4-1; and specimens of alloy B, alloy C, alloy D and alloy E were a rectangular block of $2 \times 1 \times 0.25$ in, as shown in Figure 4-2.



Figure 4-1: Specimen geometry of alloy A.

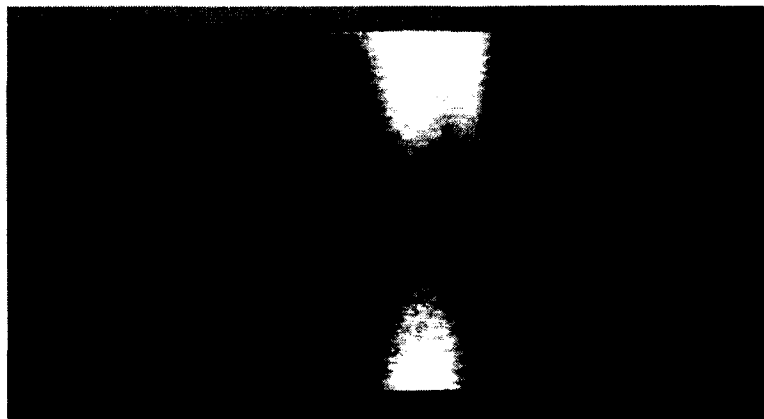


Figure 4-2: Specimen geometry of alloy B, alloy C, alloy D and alloy E.

The surface preparation of the specimens for erosion test followed the steps below:

- (1) The specimens were first cleaned with warm water by gently rubbing each specimen surface with cotton to remove any debris stuck onto the surface. This was then followed by an application of acetone to remove any grease or oil on the surface. The presence of grease or any impurities on the surface of the specimen will greatly influence the erosion result.
- (2) The cleaned specimens were then air-dried with the compressed air unit, shown in Figure 4-3. A wet surface could lead to the erodent particles adhering to the surface, eventually producing erroneous results.



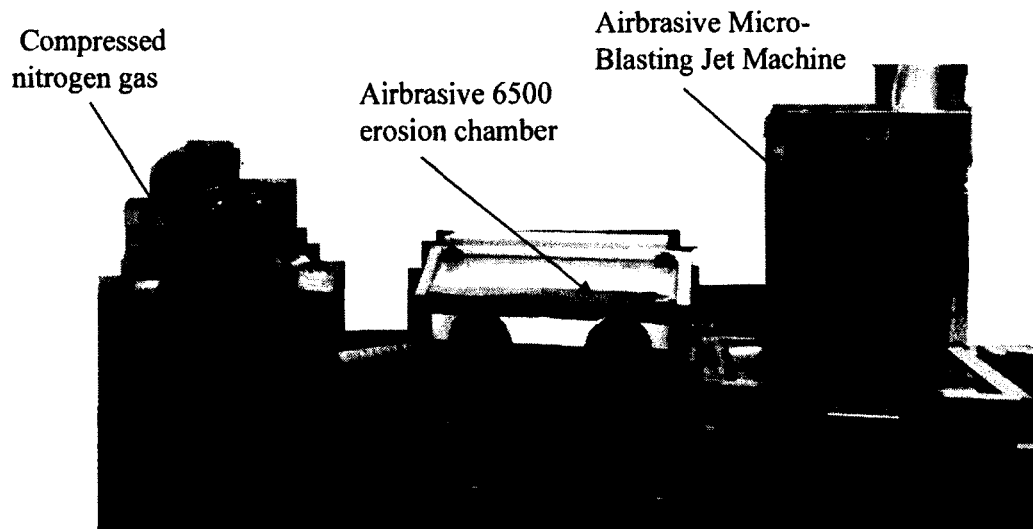
Figure 4-3: Compressed air unit used for specimen cleaning.

4.1.2 Testing facilities

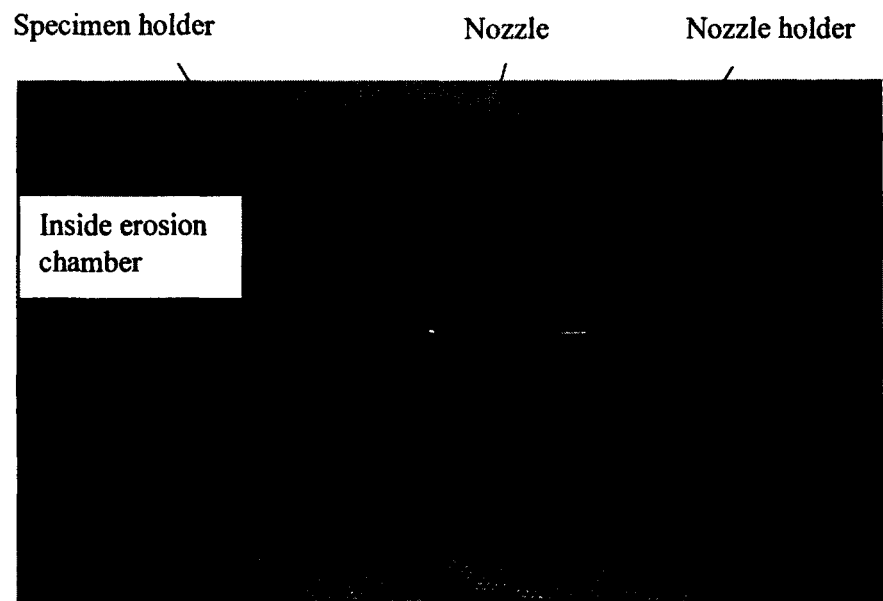
The equipment used for the solid-particle erosion test in this research was an S.S. WHITE Airbrasive Unit. The test was conducted in an inert environment at room temperature, according to the ASTM Standard G76-02. The entire apparatus is made up of five different sections: an S.S. WHITE Airbrasive Micro-Blasting Jet Machine; an S.S. WHITE Airbrasive 6500 erosion chamber; a specimen and nozzle holder; an inert environment used to accelerate the erodent (abrasive) particles; and finally a nozzle, shown in Figure 4-4.

The specimen holder contains a screw that allows for the specimens to be adjusted and rotated at various angles so as to correspond to the different impingement angles in the test, as shown in Figure 4-5. Compressed nitrogen gas (inert environment) was used as the propellant to accelerate the abrasive particles. The erodent particle feed rate could not be controlled directly on the S.S. WHITE Airbrasive Micro-Blasting Jet Machine. The S.S. WHITE Airbrasive Micro-Blasting Jet Machine contains two knobs; one controls the duct opening of the erodent particle storage tank; the other controls the voltage to the vibrator of the erodent particle storage tank, as shown in Figure 4-6.

In order to achieve a desired particle flow rate, the latter knob is regulated in conjunction with the shut-off valve on the compressed nitrogen storage tank. In some cases, the pressure regulator on the compressed nitrogen storage tank, shown in Figure 4-7, can also be moved around accordingly with the purpose of helping to adjust the particle flow rate. The former knob is used to set the particle impact velocity. It should be noted however that during the test there would always be a slight deviation from the desired particle flow rate as given in the tables in Appendix.



(a)



(b)

Figure 4-4: Entire apparatus assembly of erosion test:(a) inert environment (Compressed nitrogen gas); S.S. WHITE Airbrasive 6500 erosion chamber; and S.S. WHITE Airbrasive Micro-Blasting Jet Machine; (b) specimen and nozzle holder; and nozzle (Courtesy of S.S. WHITE Technologies Inc.).

Impingement angle controller

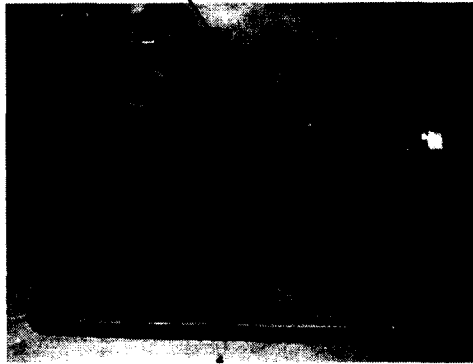


Figure 4-5: Specimen holder with screw responsible for impingement angle adjustment

(Courtesy of S.S. WHITE Technologies Inc.).

Knob responsible for erodent particle storage tank opening



Knob controlling voltage to erodent particle storage tank vibrator

Figure 4-6: S.S. WHITE Airbrasive Micro-Blasting Jet Machine with two major knobs

(Courtesy of S.S. WHITE Technologies Inc.).

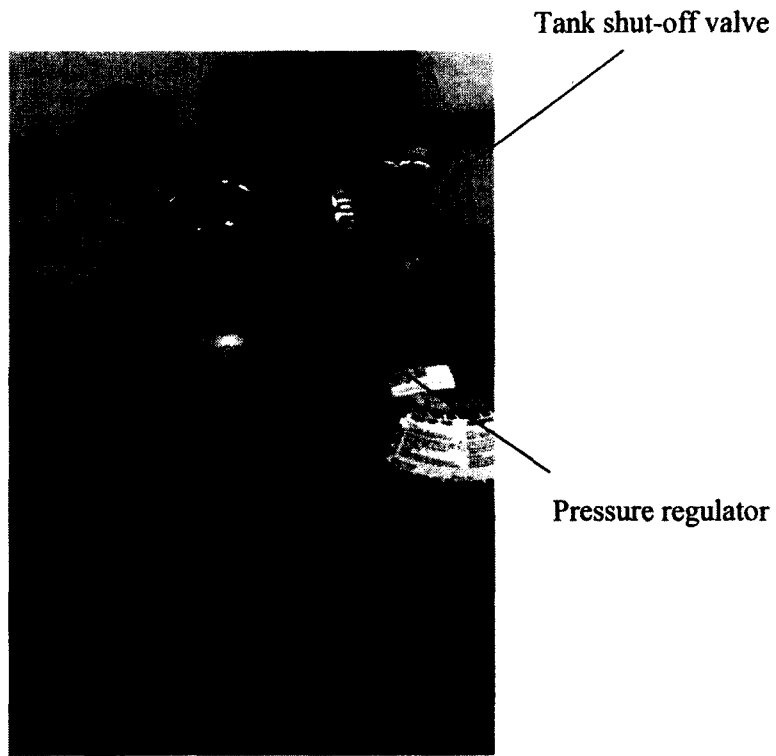
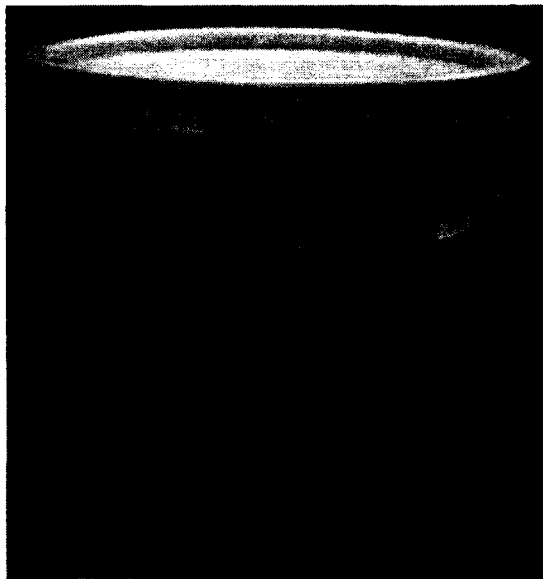


Figure 4-7: Compressed nitrogen storage tank with shut-off valve and pressure regulator.

The sand (erodent particles) used for the test were angular in shape, as shown in the SEM image in Figure 4-8(a). The product was commercial AccuBRADE-50 blend #3 alpha alumina powder with an average particle size of 50 μm , supplied by S.S. WHITE Technologies Inc, as shown in Figure 4-8(b).



(a)



(b)

Figure 4-8: Erodent particles - Angular AccuBRADE-50 blend #3 alpha alumina powder: (a) SEM morphology and (b) supplied product (Courtesy of S.S. WHITE Technologies Inc.).

4.2 Experimental Procedures

4.2.1 Test parameters

The erosion test was conducted according to the ASTM G76-02 Standard Test Method for Conducting Erosion Tests by Solid Particle Impingement Using Gas Jets, with the distance between the nozzle head and the tested specimen surface set to 5 mm, since Stellite alloys are generally very hard. At this shorter distance, reasonable damage could be observed on the specimen surface. This distance was determined through iterative trials. Two typical impingement angles, 30 degree and 90 degree, were used for each alloy at each particle impact velocity, in order to investigate the change of erosion behavior of these alloys at different particle impingement angles, because the erosion of Stellite alloys at these two angles may be controlled by different material removal mechanisms. The duration time of each test was set to 10 min, which was measured via a stopwatch. The sand flow rate was then calculated. During testing, the voltage controller was adjusted to a values between 4 ~ 6 V, which could achieve a particle flow rate between 0.70 ~ 1.28 g/min at two particle impact velocities of 84 m/s and 98 m/s. All the test parameters used in this test are summarized in Table 4-1 and Table 4-2.

Table 4-1: Erosion test process parameters

Alloy	Test Time (min)	Velocity (m/s)	Velocity (m/s)	Angle (degree)	Angle (degree)
Alloy A	10	84	98	30	90
Alloy B	10	84	98	30	90
Alloy C	10	84	98	30	90
Alloy D	10	84	98	30	90
Alloy E	10	84	98	30	90

Table 4-2: Erosion test condition parameters

Erodent Particle	Average Particle size (μm)	Nozzle Distance (mm)	Temperature (degree C)	Transport Medium
Aluminum oxide	50	5	20	Compressed nitrogen

4.2.2 Test steps

Before and after every erosion test each, specimen was weighed on a Sartorius scale balance with a resolution of 10^{-5} g, shown in Figure 4-9. The mass loss of the specimen was then computed by taking the difference between the values of the specimen's mass before and after erosion testing.

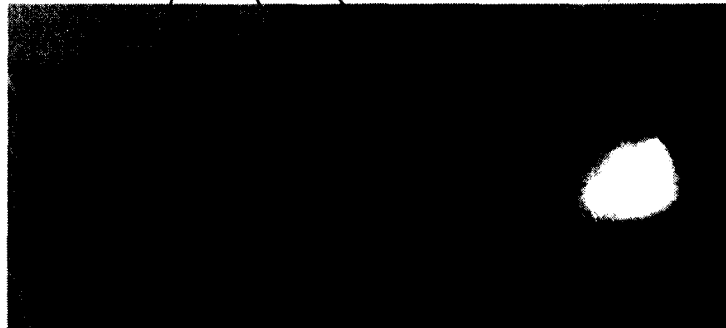


Figure 4-9: Sartorius scale balance for specimen mass measurement.

During the erosion test setup, the specimen holder was first adjusted to achieve the desired impingement angle and the specimen was then mounted onto the holder. Care should be taken when mounting the specimen onto the specimen holder to ensure that all the projected sand particles will hit the targeted surface without any overflow. Any sand particle overflow occurring will produce faulty results. The mounting procedure could be aided by marking-off some strategic placement locations with a permanent marker on both the specimen and the specimen holder, as shown in Figure 4-10.

The nozzle was mounted with the nozzle head set to a distance of 5 mm from the specimen surface, as shown in Figure 4-11 for an impingement angle of 30 degree and Figure 4-12 for an impingement angle of 90 degree. The S.S. WHITE Airbrasive Micro-Blasting Jet Machine containing aluminum oxide particles (sand) was placed on a Sartorius scale balance throughout the test process, as shown in Figure 4-13. The mass of this unit was recorded before and after running each test. The amount of sand used in each test was computed by taking the difference between these two values.

Markings on specimen



(a)

Markings on specimen holder



(b)

Figure 4-10: Marking used for specimen positioning; (a) on specimen and (b) on specimen holder.

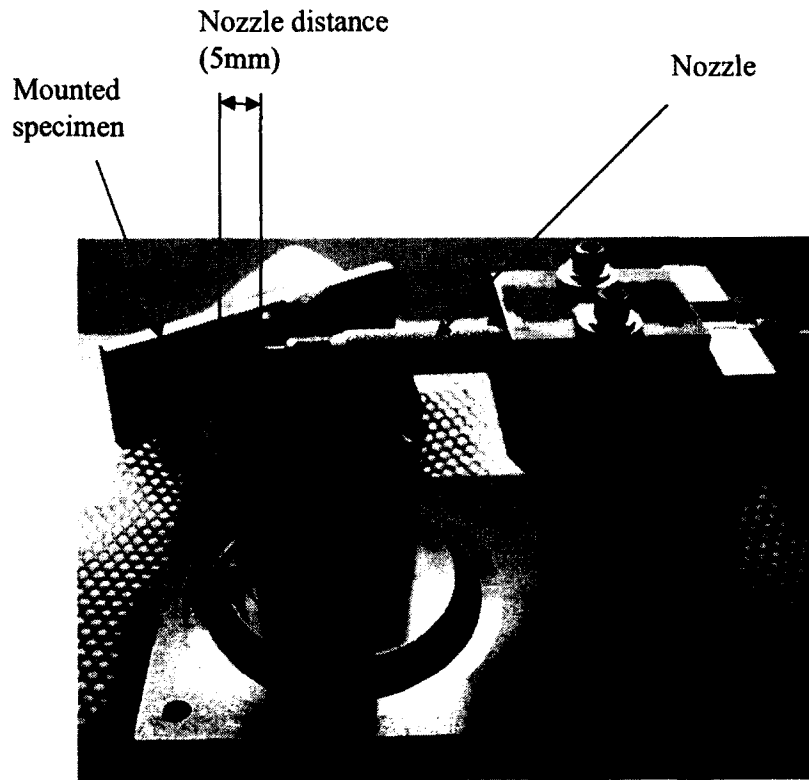


Figure 4-11: Nozzle mounting at an impingement angle of 30 degree.

To achieve a desired particle flow rate and particle impact velocity, the two knobs on the S.S. WHITE Airbrasive Micro-Blasting Jet Machine shown in Figure 4-6, in addition to the shut-off valve on the compressed nitrogen storage tank were adjusted at the start of each experiment. Each test was terminated after the sand impinged the specimen surface for 10 min.

Some alumina particles were found to adhere onto the surface of the specimen during testing. To avoid erroneous mass values, before reweighing the specimen, compressed air was used once again to clean and remove any debris on the specimen surface. Figure 4-14 shows the difference of the eroded surface before and after cleaning.

Each specimen was weighed and reweighed three times and the average mass was then computed. This was done to minimize both human error and instrumentation error involved when taking each individual measurement.

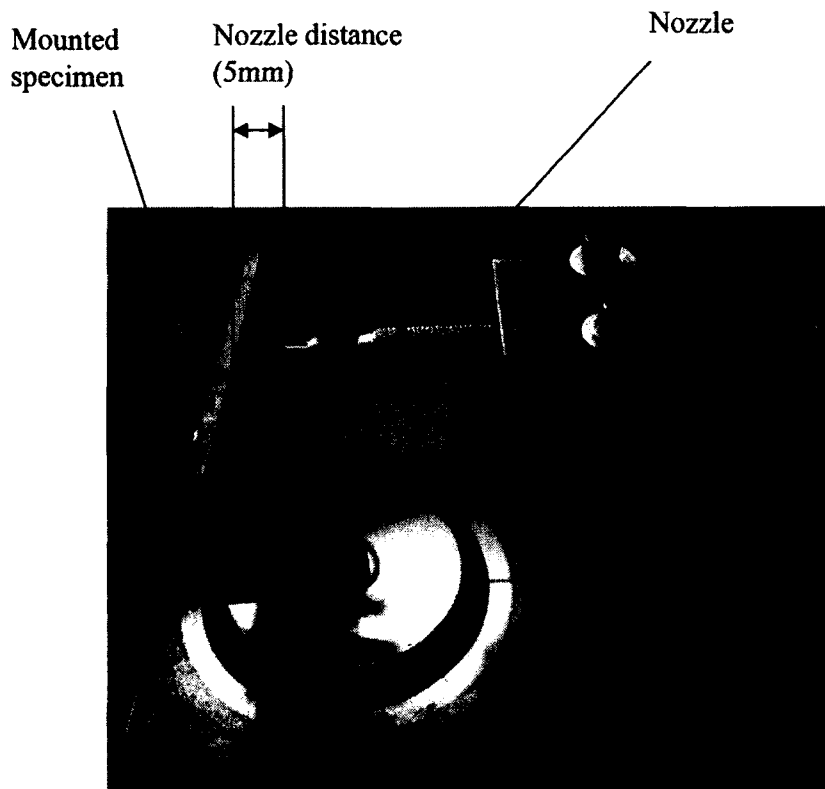
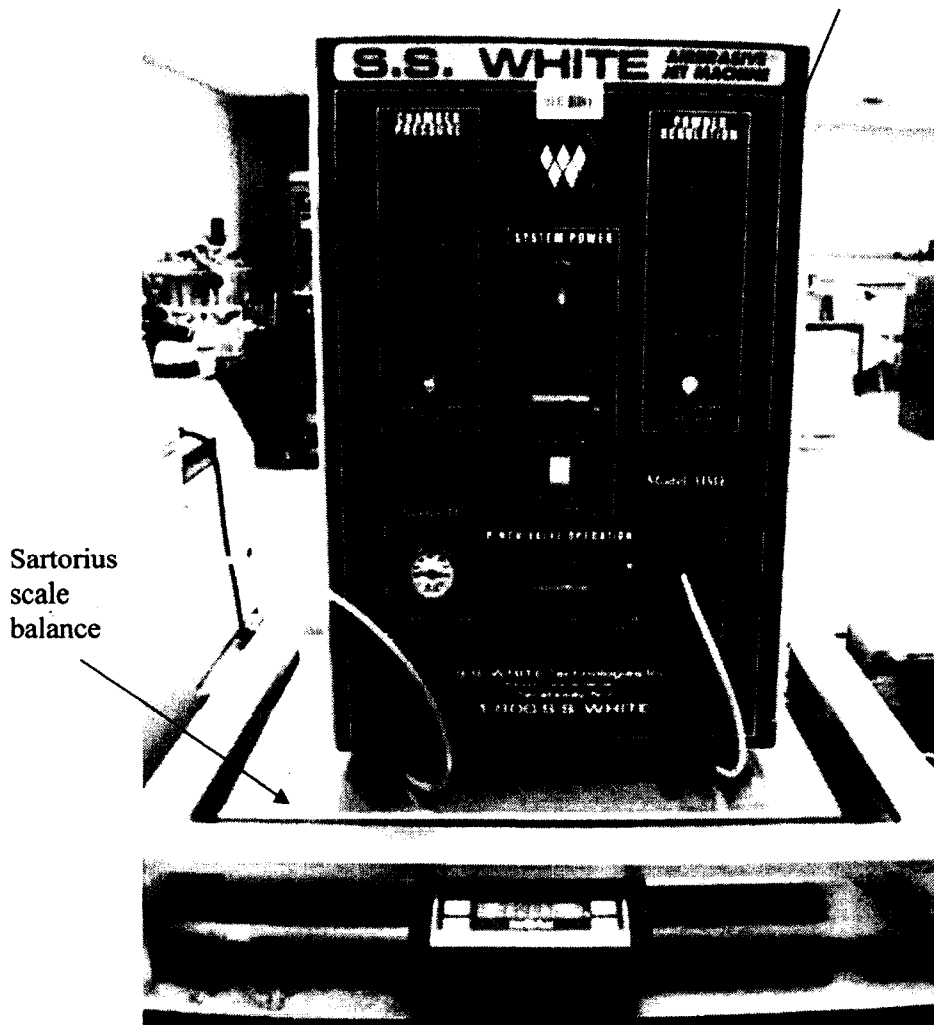


Figure 4-12: Nozzle mounting at an impingement angle of 90 degree.

Airbrasive
Micro-Blasting Jet
Machine



Sartorius
scale
balance

Figure 4-13: S.S. WHITE Airbrasive Micro-Blasting Jet Machine containing aluminum oxide particles placed on a Sartorius scale balance in the erosion test.

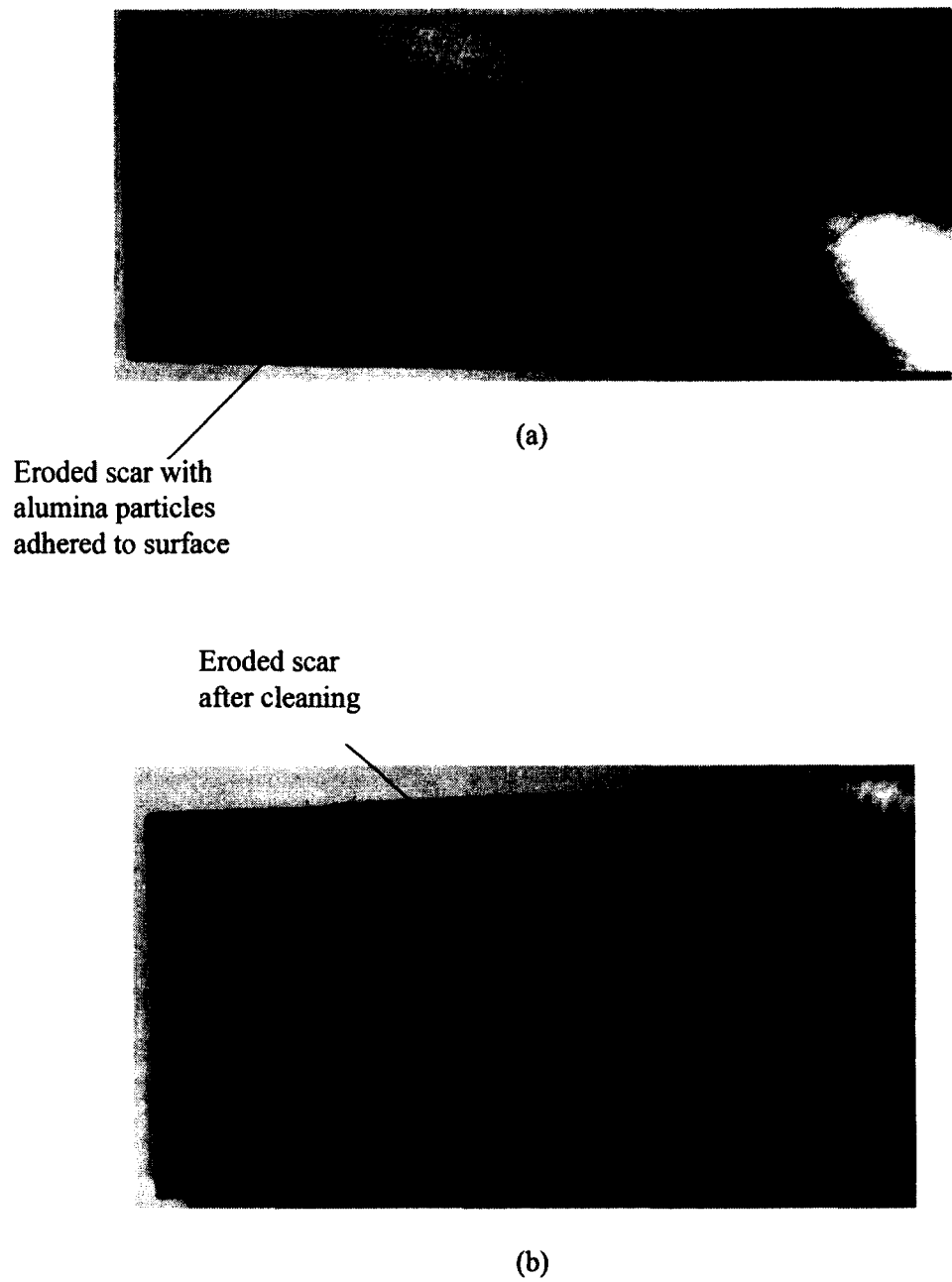


Figure 4-14: Eroded specimen surface; (a) before cleaning and (b) after cleaning

The material erosion rate was then computed. The same process was repeated four different times on the same testing spot of the specimen being tested. This is to simulate the real-world scenario as in the case of turbine blades, the dust particles would always

impact the blade randomly once the engine is turned on, thus leading to repeated impact. Finally the average material erosion rate was calculated by averaging these values.

4.3 Experimental Results

4.3.1 Sand flow rate

Once the amount of sand used during each test was computed from the mass difference of the test unit containing aluminum oxide particles (sand) before and after testing, this value was used together with the erosion time recorded (10 min) to calculate the sand (erodent particle) flow rate with units (g/min). The alumina particle flow rate was then obtained by the equation as follows:

$$\begin{aligned} \text{Sand flow rate } \left(\frac{g}{\text{min}}\right) &= \frac{\text{Mass of sand used (g)}}{\text{Erosion test time (min)}} \end{aligned} \quad (16)$$

Using alloy C at a particle impact velocity of 84 m/s and an impingement angle of 30 degree as an example, where the mass of sand used is 10 g and erosion time is 10 min, inserting these values into equation (17) yields a sand flow rate of 1 g/min.

4.3.2 Erosion rate

The averages of mass loss for each specimen were calculated. The amount of sand used per test was introduced once again together with the recorded specimen mass loss to calculate the material erosion rate with units ($\mu\text{g/g}$). The erosion rate is expressed as the ratio of the mass loss of the target material to the mass of the erodent particle used as follows:

$$\text{Erosion rate, } ER \left(\frac{\mu\text{g}}{\text{g}} \right) = \frac{\text{Specimen mass loss } (\mu\text{g})}{\text{Mass of sand used } (\text{g})} \quad (17)$$

Using alloy C at a particle impact velocity of 84 m/s and an impingement angle of 30 degree as an example, where specimen mass loss is 2650 μg and the mass of sand used is 10 g, inserting these value into equation (18) yields a value for ER of 270 $\mu\text{g/g}$.

To further minimize the experimental error, each sample point was repeated five or more times and the mean value was obtained. For example, the erosion rate of alloy C at 30 degree impingement angle and 84 m/s impact velocity was repeated five times as shown in Table A- 5 in the appendix. As a statistics analysis the standard deviation, σ , was also computed. A full summary of the erosion rates and standard deviations at the respective velocities and angles for the five alloys are given in Table A- 1 to Table A- 10 in the Appendix.

The average erosion rates with units ($\mu\text{g/g}$) at impact velocities of 84 (m/s) and 98 (m/s) for the five alloys are given in Table 4-3 and Table 4-4 respectively. These data were further accompanied with plots corresponding to individual testing conditions within 99.73% confidence interval (mean value $\mu \pm 3\sigma$), as shown in Figure 4-15 to Figure 4-18, assuming a normal distribution of the data.

As shown in Figure 4-15 at 84 m/s sand velocity and at the impingement angle of 30 degree, alloy A exhibited the lowest erosion rate of about 200 ± 110 ($\mu\text{g/g}$) while alloy E had the highest erosion rate of about 330 ± 90 ($\mu\text{g/g}$). The figure shows an increasing trend of erosion rate following an order of alloy A, followed by alloy B, alloy C, alloy D, and finally alloy E, which is the trend of C content in the alloys in decreasing order. For instance, alloy A with the highest carbon content is the most

erosion resistant while alloy E having the lowest carbon content is the least erosion resistant.

In Figure 4-16, regarding the erosion rates at 84 m/s sand velocity and at the impingement angle of 90 degree, alloy A exhibited once again the lowest erosion rate about 120 ± 81 ($\mu\text{g/g}$) while alloy D had the highest erosion rate about 240 ± 160 ($\mu\text{g/g}$). The difference in the trend of erosion rate at the impingement angle of 90 degree from that at 30 degree is that alloy C and alloy E have swap places with alloy B and alloy D respectively.

Table 4-3: Average erosion rates, ER ($\mu\text{g/g}$), at sand velocity of 84 (m/s)

Alloy	Average ER ($\mu\text{g/g}$) at 30 degree	3σ	Average ER ($\mu\text{g/g}$) at 90 degree	3σ
Alloy A	200	110	120	81
Alloy B	240	90	210	100
Alloy C	270	120	180	96
Alloy D	290	120	240	160
Alloy E	330	90	210	81

Table 4-4: Average erosion rates, ER ($\mu\text{g/g}$), at sand velocity of 98 (m/s)

Alloy	Average ER ($\mu\text{g/g}$) at 30 degree	3σ	Average ER ($\mu\text{g/g}$) at 90 degree	3σ
Alloy A	330	190	220	110
Alloy B	350	110	300	180
Alloy C	360	130	250	110
Alloy D	430	96	270	81
Alloy E	380	140	230	96

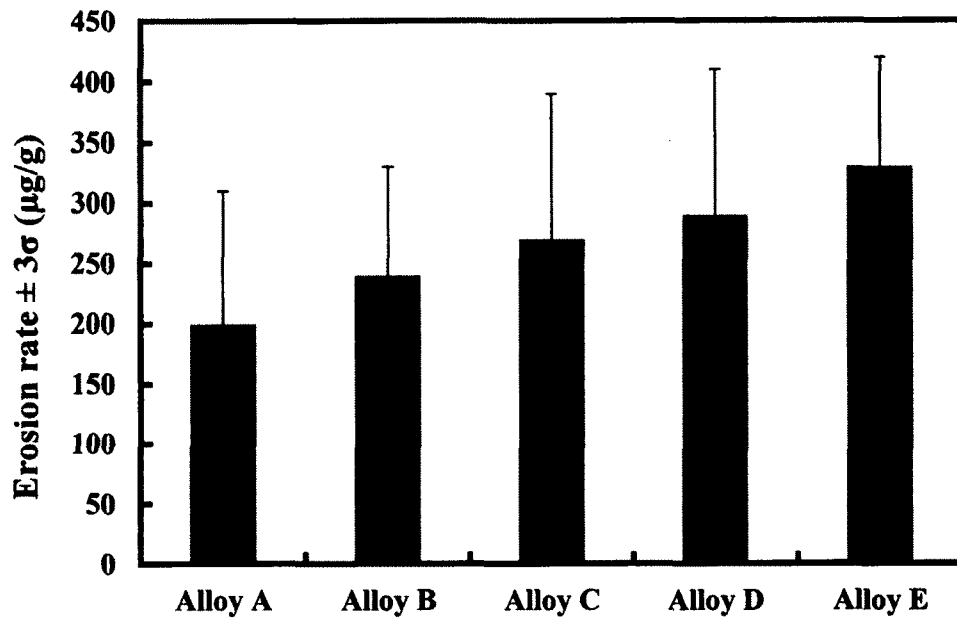


Figure 4-15: Erosion rates ($\mu\text{g/g}$) at 84 m/s sand velocity and at 30 degree impingement angle.

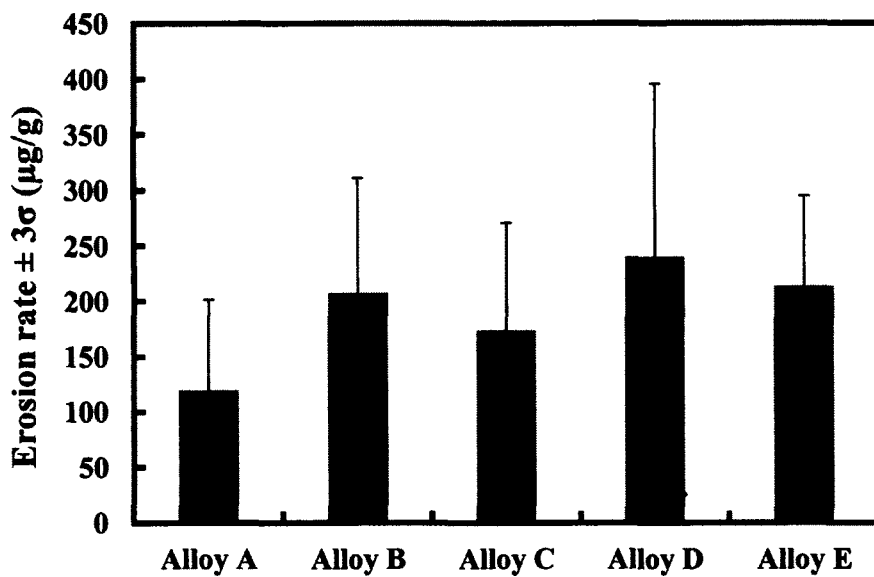


Figure 4-16: Erosion rates ($\mu\text{g/g}$) at 84 m/s sand velocity and at 90 degree impingement angle.

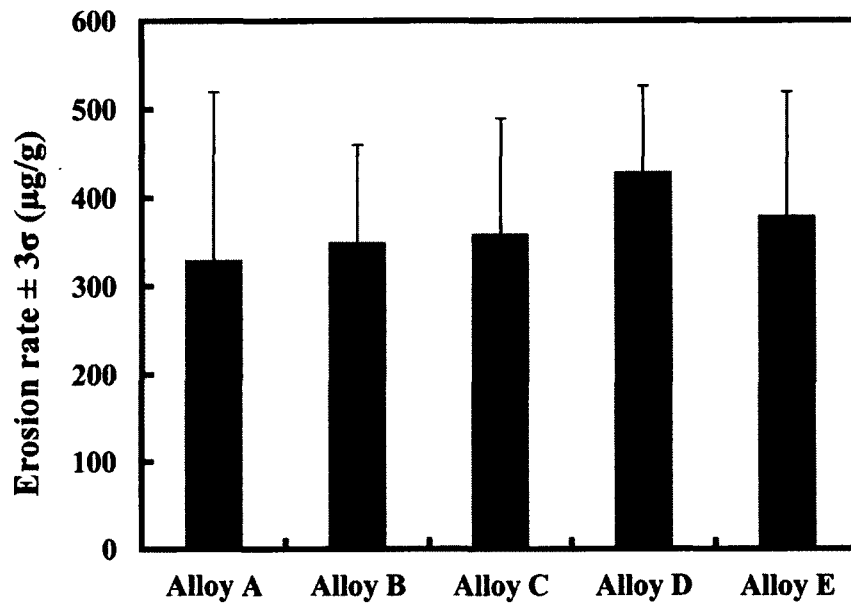


Figure 4-17: Erosion rates ($\mu\text{g/g}$) at 98 m/s sand velocity and at 30 degree impingement angle.

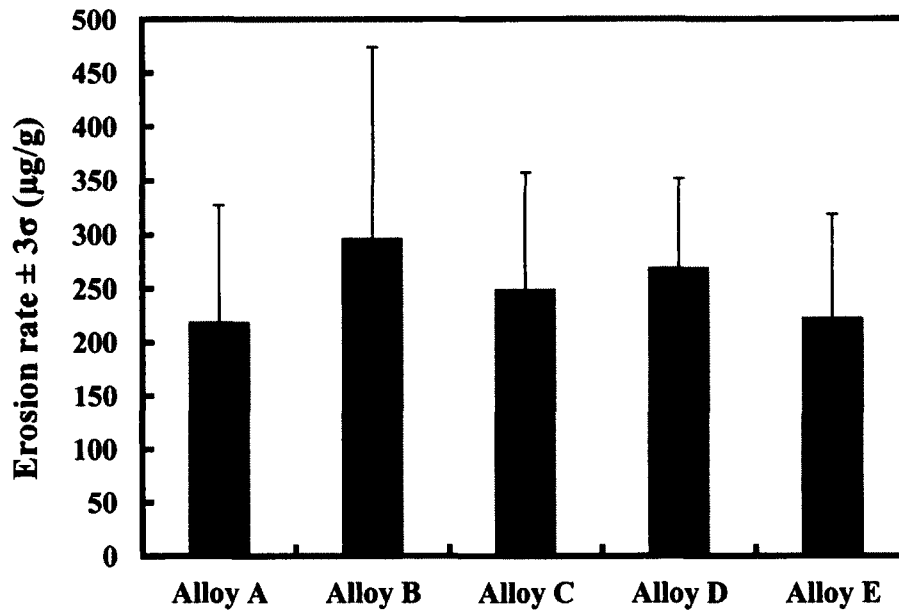


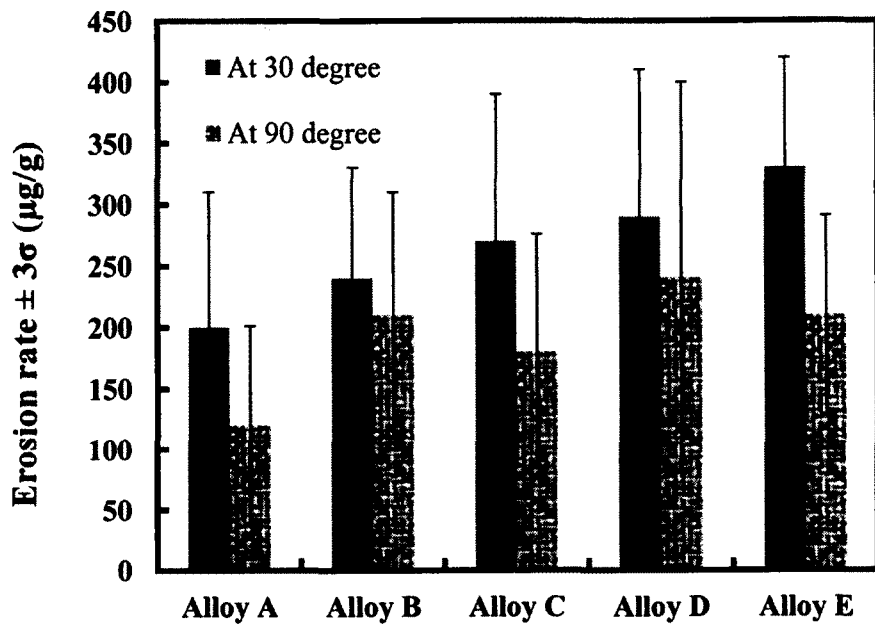
Figure 4-18: Erosion rates ($\mu\text{g/g}$) at 98 m/s sand velocity and at 90 degree impingement angle.

From Figure 4-17 at the sand velocity of 98 m/s and at the impingement angle of 30 degree, alloy A also exhibited the lowest erosion rate of about 330 ± 190 ($\mu\text{g/g}$) while alloy D had once again the highest erosion rate of about 430 ± 96 ($\mu\text{g/g}$). The trend of erosion rate is similar to the case of 84 m/s sand velocity, except alloy D. It is also noted that the difference in erosion rate between the alloys became less, compared with the lower sand velocity case.

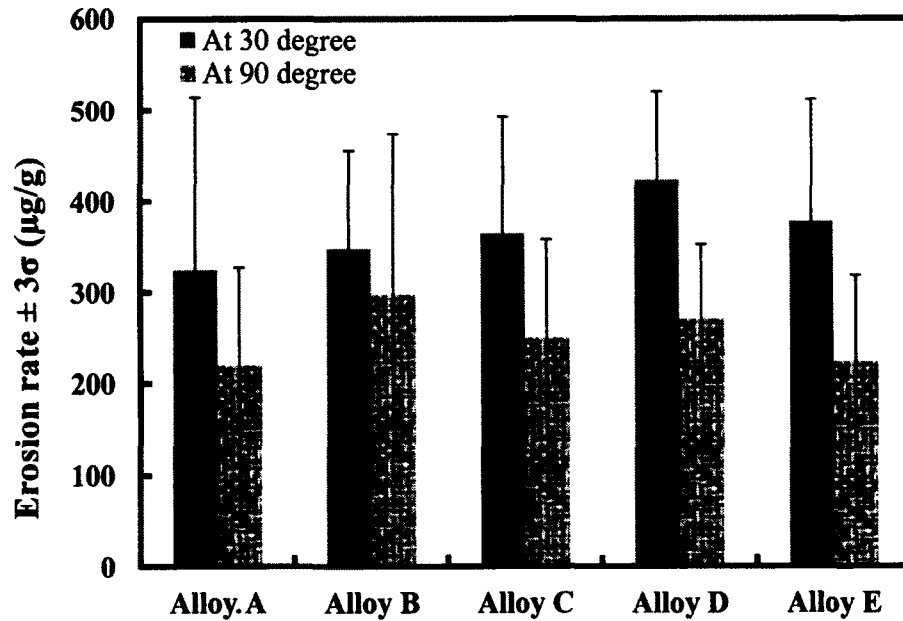
The trend of erosion rate between the alloys at the sand velocity of 98 m/s and at the impingement angle of 90 degree is similar to the case of 84 m/s sand velocity and 90 degree impingement angle, as illustrated in Figure 4-18. Alloy A showed the lowest erosion rate of about 220 ± 110 ($\mu\text{g/g}$) while alloy B had the highest erosion rate of about 300 ± 180 ($\mu\text{g/g}$). In the lower sand velocity, alloy D had the highest erosion rate.

4.3.3 Comparison of erosion rates

Firstly, comparing the erosion rates of the five alloys between the two different impingement angles, as illustrated in Figure 4-19, it is clear that the erosion at 30 degree impingement angle resulted in higher erosion rate for all the alloys at the two different sand velocities. Among these alloys, the erosion rate of alloy B (the most brittle) is the least affected by the impingement angle while the erosion rate of alloy E (which is the most ductile) is greatly influenced by the impingement angle.



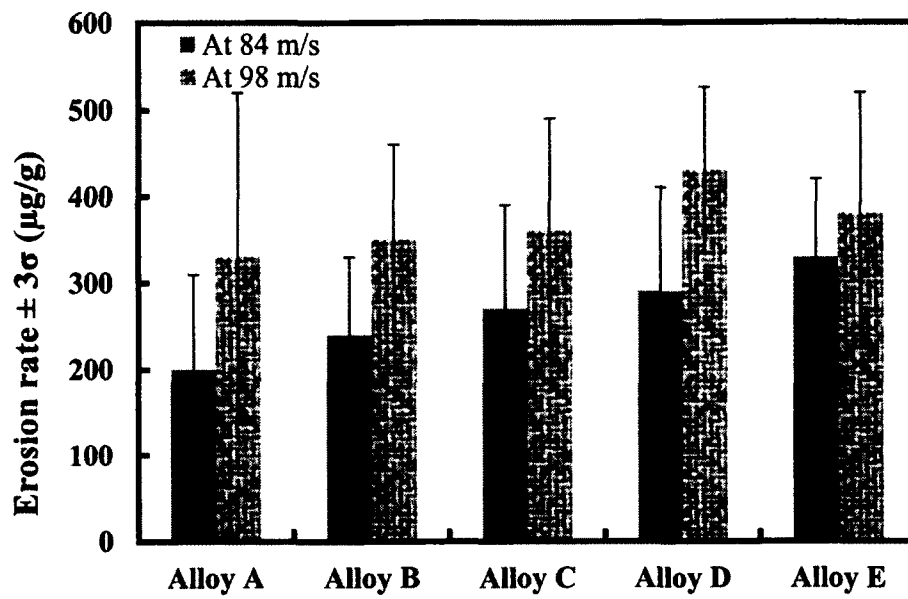
(a)



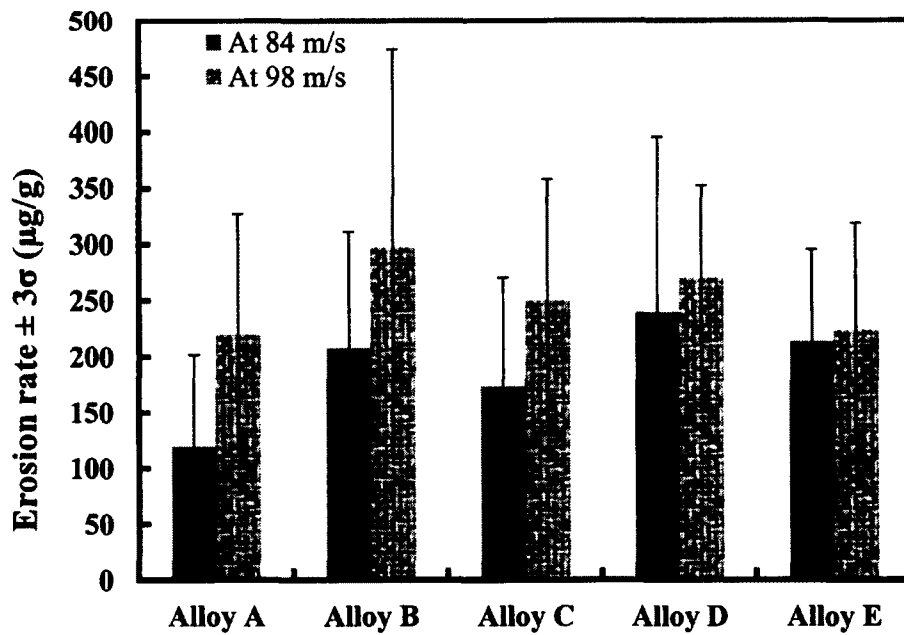
(b)

Figure 4-19: Comparison of erosion rates for different impingement angles;
 (a) at 84 m/s sand velocity and (b) at 98 m/s sand velocity.

Secondly, comparing the erosion rates of the five alloys between the two different sand velocities, as illustrated in Figure 4-20, it is evident that the erosion at the higher sand velocity resulted in higher erosion rate for all the alloys at the two different impingement angles. This is in accordance with previous results observed by other researchers [15]. However, depending on the materials there could be a threshold velocity above which the erosion rate becomes independent of impact velocity [15]. Among these alloys, the effect of sand velocity on the erosion rate for alloy E is the least significant. In particular, at the impingement angle of 90 degree, the erosion rates of the two more ductile Stellite alloys, alloy D and alloy E, are barely influenced by the sand velocity.



(a)



(b)

Figure 4-20: Comparison of erosion rates for different sand velocities;
 (a) at 30 degree impingement angle and (b) at 90 degree impingement angle.

4.3.4 Erosion rate expression in volume loss

Erosion rate can be expressed in mass loss, as demonstrated above, or another representation that can be used is the ratio of the volume loss of target material to the mass of erodent particle used, given as

$$\text{Erosion rate, } ER \left(\frac{\text{m}^3}{\text{g}} \right) = \frac{\text{Specimen volume loss (m}^3\text{)}}{\text{Mass of sand used (g)}} \quad (18)$$

The material densities of the five alloys being studied are given in Table 4-5.

Table 4-5: Target material densities (kg/m³)

Alloy	Material Density (kg/m ³)
Alloy A	8387
Alloy B	9720
Alloy C	8387
Alloy D	8400
Alloy E	8420

These alloys have density values between 8380 ~ 8430 (kg/m³) except alloy B whose density is higher, about 9720 (kg/m³). Table 4-6 summarizes the erosion rate, ER in (m³/g), of the five Stellite alloys.

Table 4-6: Erosion rates, ER expressed in volume loss, (m³/g) × 10⁻¹¹

Alloy	ER at 84 m/s and 30 degree	ER at 84 m/s and 90 degree	ER at 98 m/s and 30 degree	ER at 98 m/s and 90 degree
Alloy A	2.38	1.43	3.88	2.62
Alloy B	2.54	2.14	3.58	3.06
Alloy C	3.18	2.07	4.34	2.98
Alloy D	3.49	2.86	5.04	3.21
Alloy E	3.96	2.54	4.48	2.65

This new expression of erosion rate has no difference from the mass loss expression in nature; it would generally not affect the discussion on the erosion behavior of the Stellite alloys. Since these alloys have a similar material density except alloy B, the trends of their erosion rate in the two expressions would be similar. The only difference is for alloy B which has higher material density. For the same mass loss, higher material density leads to a less volume loss. This difference slightly changed the trends, for example, at 98 m/s sand velocity and 30 degree impingement angle, in the mass loss expression (Figure 4-17) alloy B has higher erosion rate than alloy A while in the volume loss expression (Table 4-6), the reverse is observed.

4.4 Eroded Surface Analysis

4.4.1 Erosion at 30 degree impingement angle

In order to better understand the erosion rate results and explore the erosion behavior/mechanisms of Stellite alloys, the eroded surfaces were examined using SEM. The images of the eroded surface morphologies of each specimen tested at 98 m/s sand velocity and 30 degree impingement angle are provided in Figure 4-21 to Figure 4-25.

The investigation of erosion mechanisms of materials was initially with the purpose of understanding the material removal process responsible for erosion degradation [25]. Two main material removal mechanisms have been suggested, which are the cutting and extensive/repeated deformation of the target material [30]. The chip cutting mechanism explains erosion under small angles while the material removal process occurring during normal impingements is related to plastic distortion of the surface [30]. Regarding the alloys tested in this research, the morphologies of the eroded

surfaces in Figure 4-21 to Figure 4-25 show that the general feature of materials under erosion by repeated sand impact creates a crater in the target surface, as seen in the images at low magnification. Due to the inclined angle (30 degree) to the target surface, the crater is nearly in a shape of an ellipse. Furthermore, although the chip cutting mechanism may be predominant for these alloys, plastic deformation was also involved. This can be observed in the images at high magnification. A considerable amount of overhanging lip was formed in the surfaces due to repeated cutting by the sand particles. In the meanwhile, obvious plastic flow that squeezed the lips can be observed. This plastic deformation feature is also characterized by the layered rings as observed in the eroded surfaces at low magnification, formed from accumulated plastic deformation due to repeated sand impact. The overhanging lips were vulnerable, and were broken down and eventually removed from the surface by the continuous sand impact because they were brittle and laminar. In the meanwhile, the accumulated plastic deformation caused the delamination of the sub-surface layer. Comparing the eroded surface morphology between the five alloys, plastic deformation behavior is more evident on the surfaces of alloy D and alloy E that contain lower C content and are more ductile. Compared to the other alloys, the distribution of the lips on the surface of alloy A looks more uniform and more dispersed, which implies less plastic deformation occurring in this surface. This is because alloy A contains higher C content thus larger volume fraction of carbides, which renders this alloy more brittle. The eroded surface of alloy B has a similar morphology to that of alloy A, which may also be attributed to the larger amount of carbides owing to the high W content and medium C content.

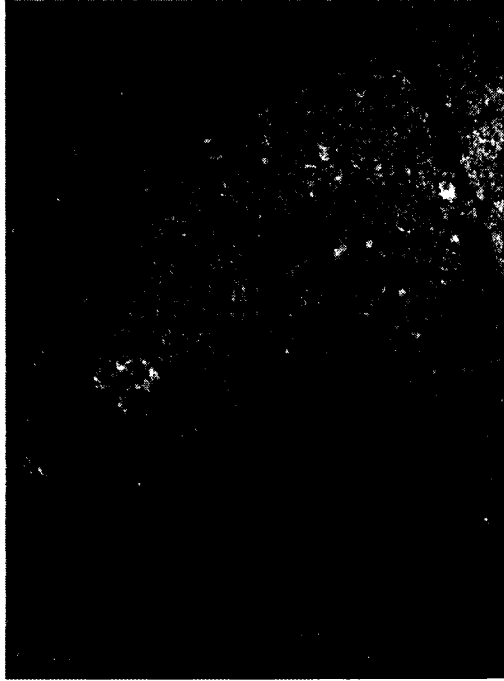


(a)



(b)

Figure 4-21: SEM images of eroded surface of alloy A tested at 98 m/s sand velocity and 30 degree impingement angle: (a) at low magnification and (b) at high magnification.



(a)

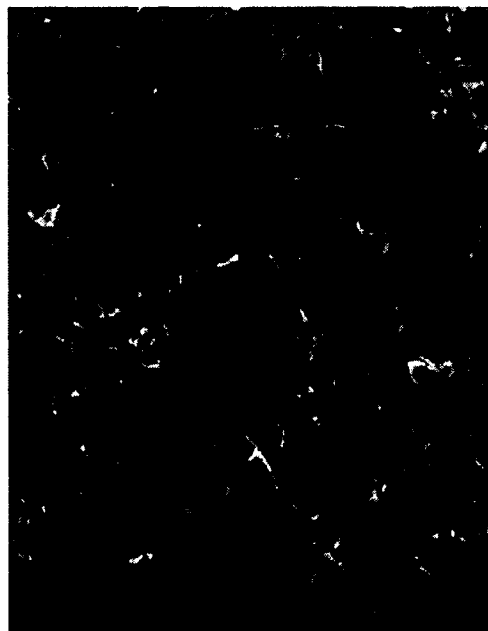


(b)

Figure 4-22: SEM images of eroded surface of alloy B tested at 98 m/s sand velocity and 30 degree impingement angle: (a) at low magnification and (b) at high magnification.

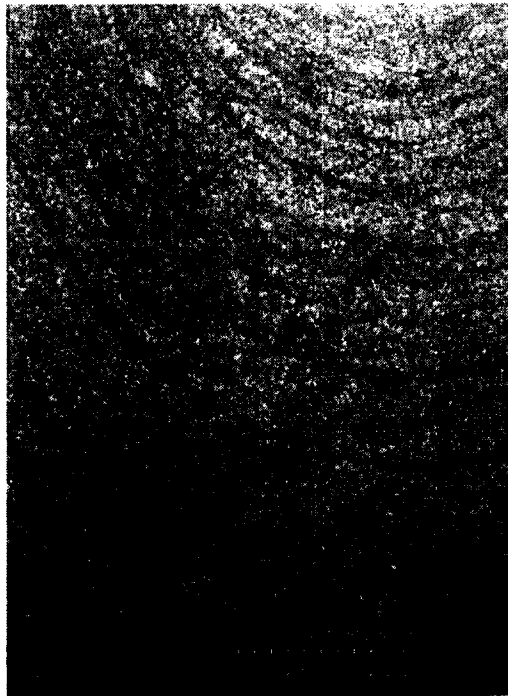


(a)



(b)

Figure 4-23: SEM images of eroded surface of alloy C tested at 98 m/s sand velocity and 30 degree impingement angle: (a) at low magnification and (b) at high magnification.

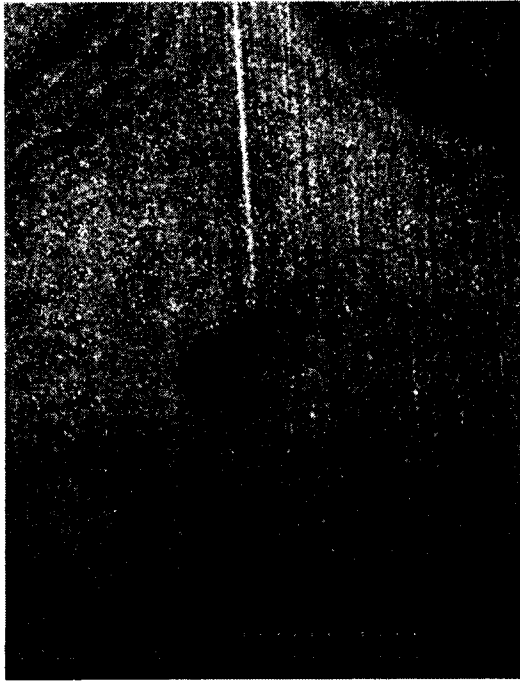


(a)

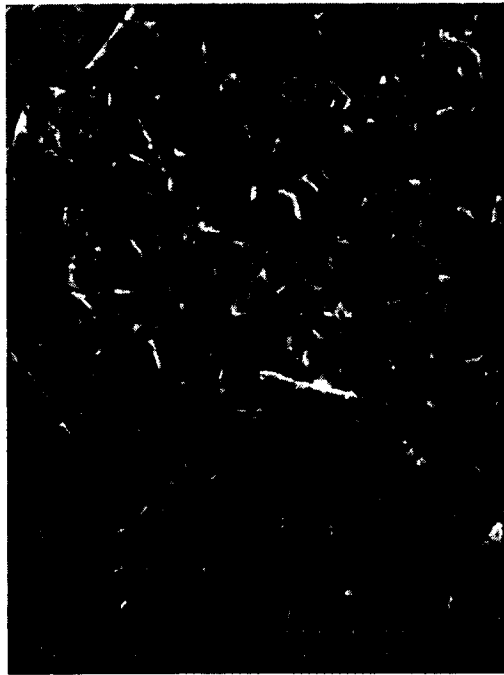


(b)

Figure 4-24: SEM images of eroded surface of alloy D tested at 98 m/s sand velocity and at 30 degree impingement angle: (a) at low magnification and (b) at high magnification.



(a)

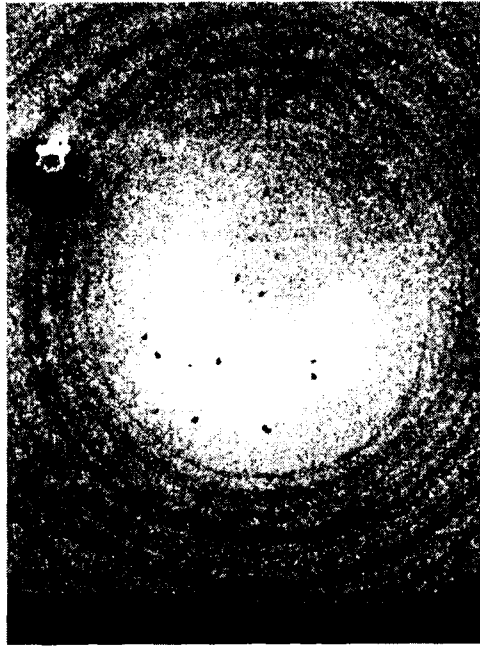


(b)

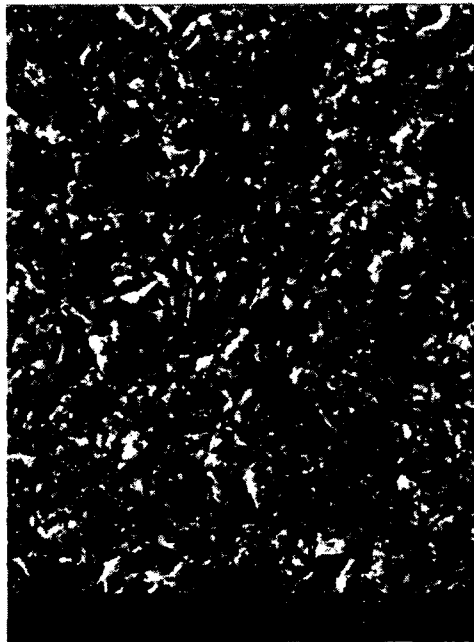
Figure 4-25: SEM images of eroded surface of alloy E tested at 98 m/s sand velocity and at 30 degree impingement angle: (a) at low magnification and (b) at high magnification.

4.4.2 Erosion at 90 degree impingement angle

The images of the eroded surface morphologies of each specimen tested at 98 m/s sand velocity and 90 degree impingement angle are provided in Figure 4-26 to Figure 4-30. Since the sand impact was normal to the target surface when the impingement angle was 90 degree, the craters formed in the eroded surfaces had roughly a circular shape, as seen in the images at low magnification. Again, layered rings are observed in the eroded surfaces of all the five alloys, which indicate that plastic deformation had occurred. Compared to the case of 30 degree impingement angle, the overhanging lips generated by the sand cutting in the surfaces eroded at 90 degree impingement angle are relatively short, as seen in the images at high magnification. There is a noticeable difference in the appearance of the eroded surface of alloy B between the two impingement angle cases; at 90 degree impingement angle the surface is less rugged and most of the lips were smashed. This observation can be attributed to the microstructure of alloy B. Since this alloy contains a large amount of primary $(W,Co)_6C$ carbide and minor eutectic Cr_7C_3 carbide, this alloy is more brittle. At 90 degree angle erosion, the normal impact force of the sand on the target surface was higher than that at 30 degree angle erosion, which would break the brittle lips, leading to higher erosion loss.



(a)

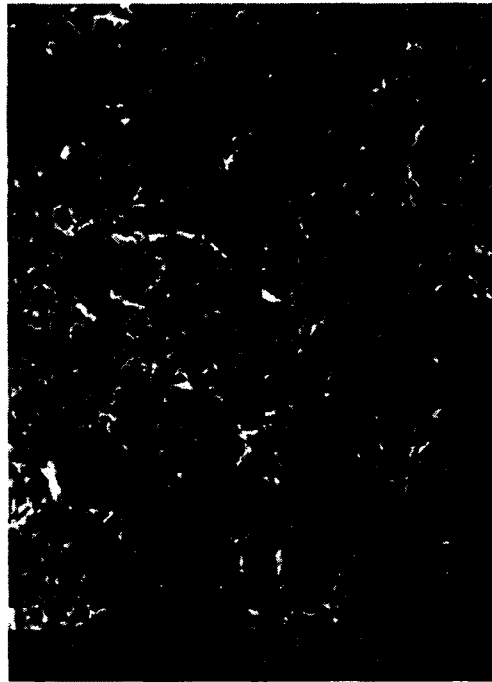


(b)

Figure 4-26: SEM images of eroded surface of alloy A tested at 98 m/s sand velocity and 90 degree impingement angle: (a) at low magnification and (b) at high magnification.



(a)



(b)

Figure 4-27: SEM images of eroded surface of alloy B tested at 98 m/s sand velocity and 90 degree impingement angle: (a) at low magnification and (b) at high magnification.

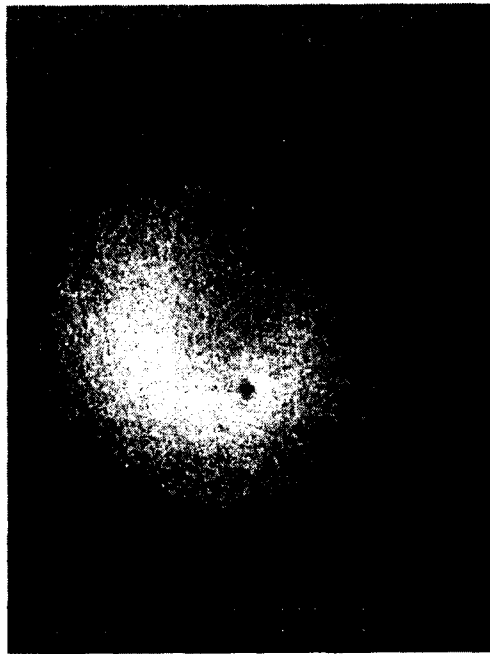


(a)

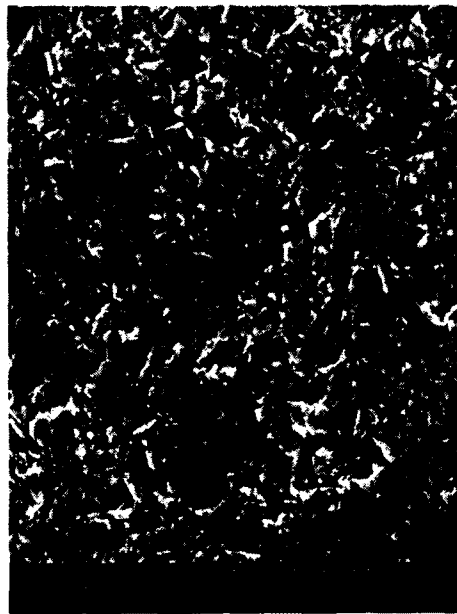


(b)

Figure 4-28: SEM images of eroded surface of alloy C tested at 98 m/s sand velocity and 90 degree impingement angle: (a) at low magnification and (b) at high magnification.



(a)



(b)

Figure 4-29: SEM images of eroded surface of alloy D tested at 98 m/s sand velocity and 90 degree impingement angle: (a) at low magnification and (b) at high magnification.



(a)



(b)

Figure 4-30: SEM images of eroded surface of alloy E tested at 98 m/s sand velocity and 90 degree impingement angle: (a) at low magnification and (b) at high magnification.

5 Chapter: Analytical Modeling of Erosion

5.1 Model Development Details

5.1.1 Background of model development

Erosion resistance of materials can be evaluated experimentally. However, due to the high capital cost and long duration involved in erosion testing, experimental data of material erosion are very limited, therefore physics-based and statistically-based erosion models have been developed to predict and identify the erosion resistance/mechanisms of metals in order to save cost and time [[7], [25]]. These models would also be used to predict the service lives of materials in erosive environments. In the present research, five Stellite alloys were studied under erosion test at two different sand impact velocities and at two different impingement angles. However, in industrial practice, a range of Stellite alloys are employed in various erosive environments; and it is impossible to obtain erosion data for all these alloys experimentally due to the high costs and time [7]. To this end, an erosion model for Stellite alloys was developed in this research, based on the experimental erosion data on the five Stellite alloys selected. This model was then utilized to predict the erosion rates of other Stellite alloys in various erosion conditions. It is known from literature review that up to date, no general, practical, predictive equations for the actual erosion degradation of a variety of material types have yet been developed, due to the large number of impact parameters encountered [[7], [15]]. Therefore, one of the main focuses in the model development of this research was to improve an existing erosion model — the S-K model by incorporating the particle impact angle in the formulation.

5.1.2 S-K model concepts

As mentioned earlier in Chapter 2, the erosion model selected for the analytical modeling of the present research is the S-K model [6]. The form of the erosion rate w , is given in equation (16), i.e,

$$w = K V^A D^B \quad (16)$$

where w is erosion wear per erodent particle; V is the particle impact velocity; D is the particle diameter; A is the velocity exponent; and B is the diameter exponent; could be used for both single particle erosion and multiple particle erosion [6]. The velocity exponent A in equation (16) was observed to lie in the range of 2.3 to 2.9 while the diameter exponent B was observed to take values of about 3 [6]. The velocity exponent could go as high as 3 occasionally [6]. As the erodent particles flow across the material surface, fragmentation occurs, which could result in secondary damage as proposed by Tilly and Sage to address the high exponent observed [51]. Table 5-1 gives values of A , and B for some typical ductile materials limited to an impact velocity of 1000 ft/s.

The S-K model was proposed to closely correlate the predicted erosion rate with their experimental data [6]. 6061-T0 aluminum specimens with an area of 0.5 in² and a thickness of 0.125 in were used for their investigations [6]. Three different types of erodent particles steel, glass shot and SiC grit, were used [6]. The tests were conducted at impact velocities of 396, 460, 760, 960 and 1190 ft/s and at impact angles of 20 degree and 90 degree, respectively [6]. In order to accelerate the abrasive particles, compressed nitrogen gas contained in a firing barrel was used as the propellant and the specimen was positioned six inches away from the firing barrel [6]. The specimen was weighed before

and after testing to determine the mass loss [6]. Table 5-2 gives a detail description of the erodent particles.

Table 5-1: Summary of particle velocity exponents and diameter exponents [6]

Test type	Impact angle	<i>A</i>	<i>B</i>
Air blast, 60 mesh SiC grit on steel, Cu, Al	20 degree	2.36	N/A
Air blast, 180 mesh SiC grit on steel	20 degree	2.36-2.69	N/A
Air blast, SiC > 100 μm on steel, Cu, Al	30 degree	3	N/A
Air blast, 60 mesh SiC on many metals	20 degree	2.05-2.44	2
Air blast, SiC > 100 μm on aluminum	20 degree	2.05-2.45	3
Air blast, SiC grit on steel, Cu, Al	20 degree	2.9	3
Whirling arm, quartz grit > 125 μm on 11% Cr-steel aluminum, etc.	90 degree	2.3	3
Whirling arm, 125-150 μm glass shot on aluminum	90 degree	2.4	N/A

Table 5-2: Properties of erodent particles [6].

Material	Manufacturer	Average diameter (in)	Average weight (g)	Micro-hardness (kg/mm ²)
Silicon carbide grit	Carborundum Co.	0.1	0.0214	2400
Steel shot	Pangborn Corporation	0.91	0.0538	700
Glass shot	Braun Hel sungen Apparaturbau	0.118	0.0298	725

After testing, the velocity and diameter exponents were found to range between 2.3 and 3.0 in both cases of single and multiple impacts [6]. At the impingement of 20 degree, the values of these exponents were higher than those at 90 degree [6]. They also used the S-K model to compare big single particle (roughly 2500 μm in diameter) erosion to the conventional multiple small particle erosion and found that the amount of material removed is approximately comparable for both cases [6].

5.1.3 Original S-K model formulation

During their model development process, Meyer's relation was assumed to remain valid for low velocity and normal impact [6]. By computing the total energy in the system, a theoretical velocity indentation relation was derived [6]. The kinetic energy (KE) of a spherical particle travelling with velocity V , diameter D , and mass density, ρ_p and colliding at 90 degree to a surface, was given by [6]:

$$KE = \frac{1}{2} \left[\frac{3}{4} \pi \left(\frac{D}{2} \right)^3 \right] \rho_p V^2 \quad (19)$$

The work done W , by the indenting sphere to reach a penetration depth q , measured normal from the surface (x -direction) was given by [6]:

$$W = \int_0^q F dx \quad (20)$$

Utilizing Meyer's relation to substitute for F in equation (21), the following was obtained [6]:

$$W = \int_0^q a \delta^n dx \quad (21)$$

where δ is the rim diameter at penetration x .

Using Pythagoras theorem, the penetration depth x was related to the instantaneous rim diameter δ , to obtain [6]:

$$2x = D - \sqrt{(D^2 - \delta^2)} \quad (22)$$

where D is particle diameter. Equating the work done during the indentation process to the maximum value of the kinetic energy and also making use of equation (23) in equation (22) give:

$$\frac{\pi}{12} D^3 \rho_p V^2 = \frac{1}{2} \int_0^d \frac{a \delta^{n+1}}{(D^2 - \delta^2)^{\frac{1}{2}}} d\delta \quad (23)$$

where d is the final value of δ .

The following two trigonometric substitutions

$$\delta = D \sin \theta \quad (25)$$

and

$$d = D \sin \theta_1 \quad (24)$$

were used to simplify expression (24) to obtain [6]:

$$\frac{\pi}{12} \frac{\rho_p V^2}{D^{n-2}} = \frac{1}{2} \int_0^{\theta_1} a \sin^{n+1} \theta d\theta \quad (25)$$

The same substitutions in equation (25) and equation (26) were employed in equation (23), to obtain an expression for the maximum value of x (q) as follows [6]:

$$\frac{2q}{D} = 1 - \cos \theta_1 \quad (26)$$

The parameter θ_1 , in equations (27) and (28), relates the particle penetration to the particle hardness [6].

For simplicity, the value of n was set to 2 in equation (27) because they observed the erosion rates of both the annealed and the work-hardened materials to be close to each other [6]. The more readily available values from Vickers diamond pyramid hardness test, H_v , were used to replace a , instead of trying to first determine the value of a for each material [6]. This was also in accordance with the fact that the Meyer's, Brinell, and Vickers hardness values were similar for values of d/D less than 0.6 [6]. The Meyer's hardness (HM) was defined as [6]:

$$HM = \frac{F}{\pi \left(\frac{d^2}{4} \right)} \quad (27)$$

The quantity a , in the Meyer's relation, takes the following form after substituting the value of n as 2 [6]:

$$a = \frac{F}{d^2} = \frac{\pi}{4} HM \approx \frac{\pi}{4} H_v \quad (28)$$

This new relation for a , was substituted in equation (27) and then integrated fully to obtain [6]:

$$V \left(\frac{\rho_p}{H_v} \right)^{\frac{1}{2}} = 1.23 \left[\int_0^{\theta_1} \sin^3 \theta \, d\theta \right]^{\frac{1}{2}} = 1.23 \left[\frac{1}{3} (2 - 3\cos\theta_1 + \cos^3\theta_1) \right]^{\frac{1}{2}} \quad (29)$$

Making use of equation (28) in equation (31) yielded [6]:

$$V \left(\frac{\rho_p}{H_v} \right)^{\frac{1}{2}} = 1.23 \left[\frac{1}{3} \left(2 - 3 \left(1 - \frac{2q}{D} \right) + \left(1 - \frac{2q}{D} \right)^3 \right) \right]^{\frac{1}{2}} \quad (30)$$

When all other parameters were kept constant, Sheldon and Kanhere went further and generated plots of $2q/D$ versus $V(\rho_p/H_v)^{\frac{1}{2}}$ for values of $2q/D$ less than 1 using

equation (32); and obtained a linear relationship between q and V [6]. Figure 5-1 shows the logarithmic plot of their findings.

Finally, the cube of the penetration depth q was proposed to be proportional to the material removal per particle w or per gram of particles of the same size [6].

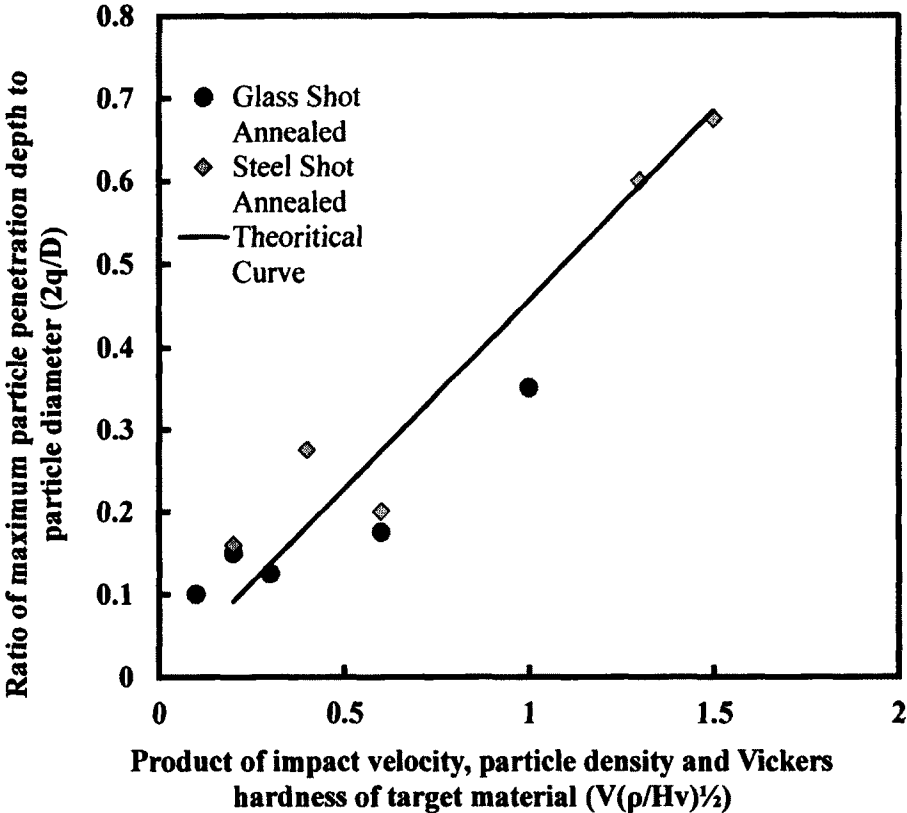


Figure 5-1: Logarithmic plot comparison of the hardness penetration theory with approximate average for normal impact test results [6].

5.2 Implementation of S-K Model

5.2.1 Test of S-K model

The S-K model under investigation is as follows [6]:

$$w \sim q^3 = \frac{D^3 V^3 \rho_p^{\frac{3}{2}}}{H_V^{\frac{3}{2}}} \quad (31)$$

where w is the volume of material removed per gram of particle, also known as the erosion rate (m^3/g); D is the particle diameter (m); V is the impact velocity (m/s); ρ_p is the particle density (kg/m^3); and H_V is the Vickers hardness of the target material (Pa). It should be noted that the H_V hardness values are measured in (kg/mm^2) but must first be multiplied by gravity, g ($9.81 \text{ m}/\text{s}^2$), converting them to (Pa) before using them in the above erosion equation [6].

Using alloy C, where D is $50 \times 10^{-6} \text{ m}$, V is $84 \text{ m}/\text{s}$, ρ_p is $3890 \text{ kg}/\text{m}^3$, and H_V is $3.87 \times 10^9 \text{ Pa}$ as an example and upon inserting these values into equation (33) a value of $7.48 \times 10^{-17} \text{ m}^3/\text{g}$ is obtained for w . Utilizing the above S-K model given in equation (33), the predicted erosion rates in Table 5-3 for the five Stellite alloys being studied were obtained for particle impact velocities of $84 \text{ m}/\text{s}$ and $98 \text{ m}/\text{s}$.

Table 5-3: Predicted erosion rates by the S-K model

Alloy	Particle Diameter (μm)	Density Particle (kg/m ³)	Vickers Hardness, HV (GPa)	Volume loss at 84 m/s (m ³ /g) × 10 ⁻¹⁷	Volume loss at 98 m/s (m ³ /g) × 10 ⁻¹⁷
Alloy A	50	3890	4.36	6.25	9.93
Alloy B	50	3890	6.16	3.72	5.90
Alloy C	50	3890	3.87	7.48	11.9
Alloy D	50	3890	3.95	7.23	11.5
Alloy E	50	3890	3.70	8.00	12.7

5.2.2 Verification of S-K model

The experimental data of erosion rates are in units of mass loss of target material per gram of erodent particle (μg/g). In order to convert the experimental erosion rates from mass loss of target material per gram of erodent particle (μg/g) to volume loss of target material per gram of erodent particle (m³/g), the following steps are taken:

Firstly, divide the erosion rate in units of (μg/g) by one thousand (1000) to get the erosion rate in units of (kg/g), as given in Table 5-4.

Table 5-4: Experimental erosion rates, ER, (kg/g) × 10⁻⁹

Alloy	ER at 84 m/s and 30 degree	ER at 84 m/s and 90 degree	ER at 98 m/s and 30 degree	ER at 98 m/s and 90 degree
Alloy A	200	120	330	220
Alloy B	240	210	350	300
Alloy C	270	180	360	250
Alloy D	290	240	430	270
Alloy E	330	210	380	230

Secondly, the results in Table 5-4 are further divided by the respective densities in units of (kg/m³) of the target materials accordingly to obtain the required erosion rate in units of (m³/g).

For example, using alloy C at a particle impact velocity of 98 m/s and an impact angle of 90 degree where ER is 250×10^{-9} (kg/g) and its density of 8387 (kg/m³) yields an erosion rate of 2.98×10^{-11} m³/g.

After applying this same methodology to the other alloys, the results in Table 5-5 can be obtained.

Table 5-5: Experimental erosion rates in volume loss, ER, (m³/g) $\times 10^{-11}$

Alloy	ER at 84 m/s and 30 degree	ER at 84 m/s and 90 degree	ER at 98 m/s and 30 degree	ER at 98 m/s and 90 degree
Alloy A	2.38	1.43	3.88	2.62
Alloy B	2.54	2.14	3.58	3.06
Alloy C	3.18	2.07	4.34	2.98
Alloy D	3.49	2.86	5.04	3.21
Alloy E	3.96	2.54	4.48	2.65

The experimental erosion rates are in the order of (10^{-11} (m³/g)) while the predicted erosion rates from the S-K model are in the order of (10^{-17} (m³/g)) as can be seen in Table 5-3 and Table 5-5. Before proceeding, the predicted erosion rates were multiplied by a factor of (10^6) to correct for the difference in order. This could be accounted for by the fact that the S-K model was developed and then verified with aluminum as the target surface while the alloys under investigation are Stellite alloys [6]. Aluminum and Stellite alloys fall under two different categories with aluminum being more ductile than Stellite alloys [1].

Thus, the appropriate erosion model equation to be used for comparison is a slightly modified version of the S-K model in equation (33) [6] and is as follows:

$$w = \frac{C_1 D^3 V^3 \rho_p^{\frac{3}{2}}}{H_v^{\frac{3}{2}}} \quad (32)$$

where C_1 is a constant known as is the order correction factor with a value of 1×10^6 . The new predicted erosion rates from the S-K model are given in Table 5-6.

As can be seen in Table 5-6, at both 84 m/s and 98 m/s sand velocities, the S-K model predicts that alloy B has the lowest erosion rate with an approximate value of $3.72 \times 10^{-11} \text{ m}^3/\text{g}$ and $5.90 \times 10^{-11} \text{ m}^3/\text{g}$ respectively while alloy E has the highest erosion rate with an approximate value of $8.00 \times 10^{-11} \text{ m}^3/\text{g}$ and $12.7 \times 10^{-11} \text{ m}^3/\text{g}$ respectively.

Table 5-6: Predicted erosion rates from S-K model after applying an order correction factor

Alloy	Volume loss at 84 m/s (m^3/g) $\times 10^{-11}$	Volume loss at 98 m/s (m^3/g) $\times 10^{-11}$
Alloy A	6.25	9.93
Alloy B	3.72	5.90
Alloy C	7.48	11.9
Alloy D	7.23	11.5
Alloy E	8.00	12.7

To perceive a visual comparison between the S-K model results and the experimental data, the erosion rates from the S-K model and from the erosion test are plotted together in Figure 5-2 and Figure 5-3.

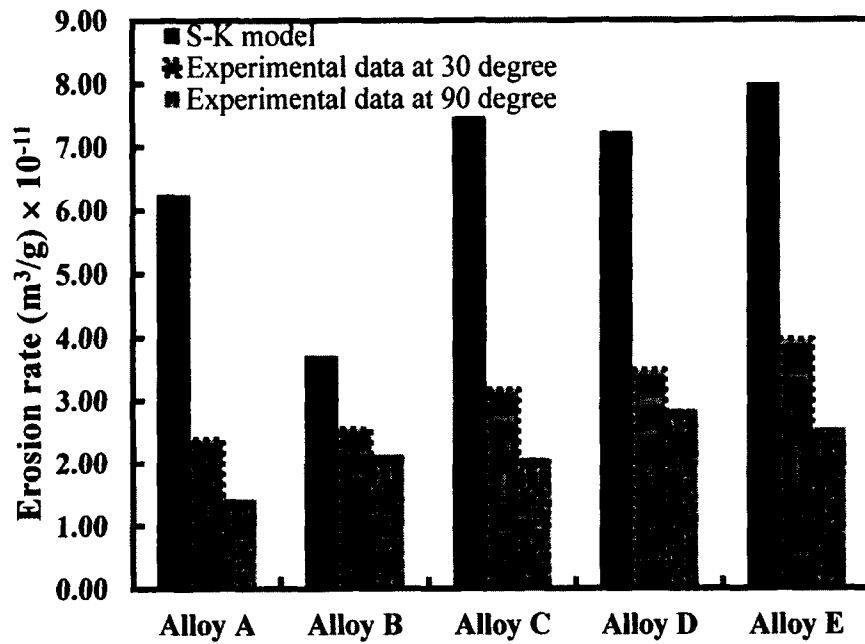


Figure 5-2: Comparison of Erosion rates at sand impact velocity of 84 m/s.

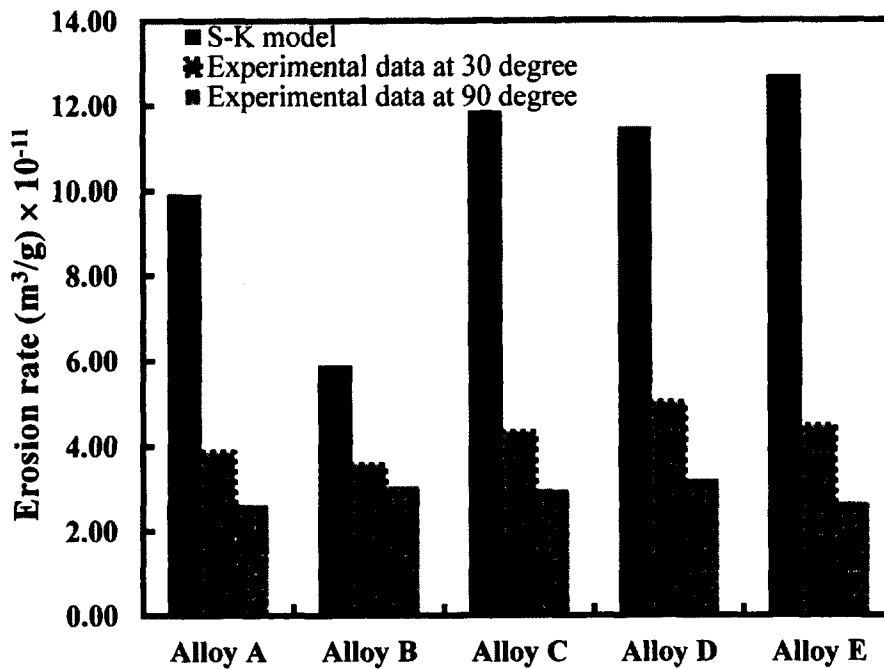


Figure 5-3: Comparison of erosion rates at sand impact velocity of 98 m/s.

From the comparison in Figure 5-2 and Figure 5-3, it is observed that the predicted values of erosion rate from the S-K model do not best fit the experimental erosion rates of the alloys under investigation. All the predicted values are higher than the experimental measurements. Moreover, the proposed S-K model does not account for the impingement angle and thus calls for modification [6].

5.3 Modification of the S-K Model

5.3.1 Statistical formulation

As demonstrated in Figure 5-2 and Figure 5-3, the S-K model over estimates the erosion rate when compared to the experimental data. Moreover, it is ambiguous as to what impingement angle the model tries to use in predicting the erosion rate [6].

In the S-K model, the erosion rate, w , is described as a function of particle diameter D , particle velocity, V , particle density, ρ_p , and target material hardness, HV , that is, w is given as a function of four variables, $w(D, V, \rho_p, HV)$ [6]. This function for the erosion rate is independent of particle impact angle, α . Therefore, the first modification for the model is to include the impingement angle. The modified model contains a new erosion rate function, w_1 , of five variables, that is, $w_1(D, V, \rho_p, HV, \alpha)$.

Checking each variable in w_1 and considering the actual physics or mechanisms occurring during the erosion process, it might be customary to assume that a change in the particle impact angle would most likely affect the normal and tangential components of the particle impact velocity on the target material [15]. This tends to affect the erosion mechanism occurring at each impact angle [[8], [13], [15]]. The other three variables, that is, particle diameter, particle density and target material hardness could be assumed

independent of particle impact angle for the purpose of this analysis. Therefore, the modified particle impact velocity will be expressed as a function of particle impact angle and the “originally set” impact velocity from now forth. That is V_1 is a function of two variables, $V_1(V, \alpha)$, expressed as:

$$V_1 = V * K \quad (33)$$

where V_1 is the modified particle impact velocity (m/s); V is the originally set particle impact velocity (m/s); and K is a dimensionless function of α , $K(\alpha)$, and is called the angle correction factor. After working through numerous fitting algorithms of the experimental data in MATLAB and comparing these results to the values of w obtained from equation (34) for each alloy, the proposed form of K for these alloys under investigation is found to take the following form;

$$K = X^b \quad (34)$$

where

$$X = X(\alpha) = a * \left(\sin\left(\frac{\alpha}{2}\right) \right)^{\frac{1}{3}} \quad (35)$$

where α is the particle impact angle (degree); a is a constant referred to as the shifting coefficient; and b is another constant called the shifting exponent. It should be noted that both the shifting coefficient and shifting exponent are target material-dependent, but the variation within Stellite alloys is very small. This suggested form of K is used to predict the erosion rate in (m^3/g) at various particle impact angles at a given particle impact velocity for a specific Stellite alloy.

5.3.2 Determination of constants

The compacted form of the modified model suitable for these alloys is an improved version of the S-K model in equation (33) [6] and is given as:

$$w_1 = \frac{C_1 D^3 (V * K)^3 \rho_p^{\frac{3}{2}}}{H_v^{\frac{3}{2}}} \quad (36)$$

Substituting equations (36) and (37) into equation (38) yields the following expression:

$$w_1 = \frac{C_1 D^3 \left(V * \left(a * \left(\sin \left(\frac{\alpha}{2} \right) \right)^{\frac{1}{3}} \right)^b \right)^3 \rho_p^{\frac{3}{2}}}{H_v^{\frac{3}{2}}} \quad (37)$$

Equation (39) has four new parameters compared to the original S-K model in equation (33) [6]. To determine the two constants, a and b , in equation (39) for a given alloy, an iteration process using MATLAB has been taken. Taking alloy C as an example, C_1 is 1×10^6 , D is 50×10^{-6} m, V is 84 m/s, ρ_p is 3890 kg/m^3 , H_v is 3.87×10^9 Pa, α is 30 degree and α is 90 degree, respectively, inserting these values into equation (39) and making trials on the values of a and b towards the experimental erosion rates of $3.18 \times 10^{-11} \text{ m}^3/\text{g}$ for 30 degree impingement angle and $2.07 \times 10^{-11} \text{ m}^3/\text{g}$ for 90 degree impingement angle in Table 5-5 for w_1 , the values of a and b were determined such that the w_1 values from equation (39) reached the experimental erosion rates with an error less than 5%. With this fitting process, for alloy C eroded at 84 m/s sand velocity, the values of a and b were determined to be 3.235 and -0.3917, respectively. Using equation (39) one may predict the erosion rates for alloy C at any particle impact angle.

Table 5-7 provides a summary of the values of a and b and the erosion rates predicted from equation (39) using the values of a and b for each alloy under investigation. It is found that although the values of a and b vary from alloy to alloy these values are close to each other within the Stellite alloy family. Also, it is noticed that the values of a and b vary insignificantly with the sand impact velocity.

Therefore, the significance of this modified model can be summarized as:

- (1) For the five Stellite alloys being studied in this research, with this model at the two sand impact velocities used in the erosion test, the erosion rates at particle impingement angles between 30 degree and 90 degree can be approximately predicted.
- (2) For these alloys, using this model at any sand impact velocity, the erosion rates at particle impingement angles between 30 degree and 90 degree can be estimated.
- (3) For any new Stellite alloy having a similar chemical composition to one of the five alloys, the erosion rates at particle impingement angles between 30 degree and 90 degree can be estimated using this model at any sand impact velocities.

Table 5-7: Values of constants and predicted erosion rates from the modified model

At particle impact velocity of 84 m/s				
Alloy	Coefficient <i>a</i>	Exponent <i>b</i>	Predicted <i>ER</i> Value (m ³ /g) × 10 ⁻¹¹ for 30 degree	Predicted <i>ER</i> Value (m ³ /g) × 10 ⁻¹¹ for 90 degree
Alloy A	3.56	-0.413	2.26	1.50
Alloy B	3.5	-0.15	2.59	2.23
Alloy C	3.235	-0.3917	3.20	2.16
Alloy D	3.452	-0.2893	3.65	2.73
Alloy E	2.95	-0.3833	3.87	2.63
At particle impact velocity of 98 m/s				
Alloy A	3.5	-0.391	3.87	2.62
Alloy B	3.45	-0.204	3.64	2.97
Alloy C	3.75	-0.3867	4.32	2.93
Alloy D	3.23	-0.3917	4.92	3.32
Alloy E	3.67	-0.4277	4.27	2.78

6 Chapter: Discussion on Results and Correlations

6.1 Chemical Composition

6.1.1 Effects on microstructure

Chemical composition, fabrication process, heat treatment, cold and hot work, altogether determine the microstructure of a material, and hence control the physical/mechanical properties of its products [[6],[22],[32]]. Carbon is a very important element, making the carbide volume fraction in Stellite alloys a critical parameter [1]. Among the five alloys studied in this research, alloy D and alloy E contain considerably less carbon, so that they are solution-strengthened alloys. In their microstructures, as shown in Figure 3-22 and Figure 3-25, there are very small amounts of carbides, but it should be noted that there is a certain amount of intermetallic compounds of Co_3Mo and CoMo_6 in these alloys due to the high Mo content, which increase the hardness but decrease the ductility of the alloys. On the contrary, alloy A contains a very high content of carbon, thus a large amount of carbides, in the form of primary Cr_7C_3 , as seen in its microstructure in Figure 3-12. In addition to carbon, other alloying elements such as Cr, W and Mo also play important role in the microstructures of Stellite alloys. For example, tungsten mostly enhances the strength of Stellite alloys and when tungsten is present in large amounts, it contributes to $(\text{W},\text{Co})_6\text{C}$ carbide formation, as demonstrated in the microstructure of alloy B in Figure 3-15, which would improve the hardness and erosion resistance of the alloy. Molybdenum in alloy D and alloy E also enhances the strength of these alloys; it also increases corrosion resistance and when in excess it forms two inter-metallic compounds of Co_3Mo and CoMo_6 , as demonstrated in the microstructures of alloy D and alloy E in Figure 3-22 and Figure 3-25. Chromium is the indispensable

element in Stellite alloys. The five alloys under investigation all contain a large amount of chromium (22 ~ 30 wt%) which provides corrosion and oxidation resistance and also forms chromium carbides for erosion resistance. At room temperature, nickel in alloy A, alloy C, alloy D and alloy E stabilizes the fcc form of the matrix which increases machinability of these alloys [[1],[4]].

6.1.2 Relationship between microstructure and hardness

The overall (macro-) hardness test was performed for each alloy being studied in this research. Both the Rockwell C (HRC) hardness values and Vickers hardness (HV) values for this group of Stellite alloys were measured and the results are presented in Table 6-1. The solid solutions of Stellite alloys are much softer than the carbide phases. The two common types of carbides encountered in Stellite alloys are Cr_7C_3 and $(\text{W},\text{Co})_6\text{C}$. As demonstrated in the indentation test results in Table 6-1, the overall hardness of each alloy is mainly controlled by the volume fraction of carbides but also by the amount of the intermetallic compounds of Co_3Mo and CoMo_6 in its microstructure. Definitely, the more carbides or Co_3Mo and CoMo_6 in the microstructure, the harder the alloy is. For example, alloy A with the highest carbon content in its chemical composition would be expected to be harder than alloy E with the lowest carbon content in its chemical composition. This is confirmed with the hardness values in Table 6-1. However as mentioned earlier, the addition of tungsten or molybdenum tungsten enhances the strength of Stellite alloys [1]. Tungsten of 32 wt% in alloy B renders this alloy to be harder than alloy A and molybdenum of 11.8 wt% in alloy D promotes this alloy to be harder than alloy C, as demonstrated in Table 6-1. The increase in hardness for these

alloys is attributed to the formation of $(W,Co)_6C$ carbide or intermetallic compounds of Co_3Mo and $CoMo_6$.

Furthermore, since the hardness of the aluminum particles is approximately twice that of the alloys as seen in Table 6-1, the erosion rate would be independent of the erodent particle hardness [15].

Table 6-1: Hardness values of Stellite alloys

Alloy	HRC	HV (kg/mm^2)	HV (GPa)
Alloy A	44.72	444.2	4.36
Alloy B	56.8	628.4	6.16
Alloy C	40.18	394.2	3.87
Alloy D	41	403	3.95
Alloy E	38.46	377	3.70
Aluminum oxide	N/A	1175	N/A

6.2 Correlations of Experimental Results

6.2.1 Erosion resistance versus microstructure

It is evident that the erosion resistance of Stellite alloys is affected strongly by their microstructures. On the other hand, the erosion resistance of these alloys is also influenced by the erosion condition, for example, the particle impact angle and velocity. Reviewing the erosion test data in Figure 4-15, at 84 m/s sand impact velocity and at 30 degree impingement angle, the erosion rate of Stellite alloys is inversely proportional to the carbide volume fraction and the amount of intermetallic compounds. Since the material damage under erosion is caused by cutting and extensive/repeated deformation of the target material [31], the presence of carbides and intermetallic compounds can resist both actions. However, at 90 degree impingement angle, the erosion rate does not

follow this trend, as illustrated in Figure 4-16. Also the erosion rate for all the alloys decreases at this angle.

For metallic materials, which are relatively ductile compared to ceramics or glass [8], erosion rate initially increases with the particle impact angle until reaching the critical angle around 30 degree and then starts to decrease, as reported by previous research [7]. At a small impact angle, the impact of particles generates tensile plastic strain at the sub-surface of the target material due to shearing action, which is similar to the mechanism of materials under sliding wear [[3],[4]]. With the repeated impact of particles plastic deformation is accumulated. When the accumulated strain reaches the material limit, the material breaks down at the sub-surface, leading to material removal thus erosion damage [[13],[33]]. On the contrary, at 90 degree impingement angle, particles impact the target surface normally, causing deformation of the surface layer. The normal impact generates compressive stress/strain in the surface layer. In general, ductile materials have higher compressive strength than tensile strength, while the opposite is exhibited by brittle materials [1]. This can explain the curves in Figure 2-2 [7]; the erosion rate of brittle materials are more sensitive to the increase in particle impact angle than ductile materials. At the 90 degree impingement angle erosion when the compressive strain of the surface layer reaches the material limit, the layer spalls off from the material surface, adding to the erosion loss. Stellite alloys are known to possess better compressive strength than tensile strength [4]; therefore they exhibited higher erosion resistance at 90 degree impingement angle than at 30 degree impingement angle. As illustrated in Figure 4-16 and Figure 4-18, alloy B and alloy D exhibited higher erosion rate than the other alloys at 90 degree impingement angle. Referring to the

microstructures in Figure 3-15 and Figure 3-22 and hardness values in Table 6-1, alloy B contains a very large volume fraction of carbides (Cr_7C_3 and $(\text{W},\text{Co})_6\text{C}$) and alloy D contains a large amount of intermetallic compounds (Co_3Mo and CoMo_6), which render these alloys relatively brittle compared to the other alloys. Under the normal impact load from the sand, high stress concentration was induced in the target surface, causing more cracking and fracture in these alloys than in the others, leading to higher erosion loss.

From Figure 4-20, the erosion rate of all the alloys increased with the particle impact velocity. It is also noted that the difference of erosion rate between the alloys at the higher velocity became less; that is, the erosion-resistant effect of carbides and intermetallic compounds at high particle impact velocities was less significant. The reason for this may be strain hardening of the Co solid solutions. Higher particle impact velocity promoted the strain hardening thus enhancing the erosion resistance of the solid solutions. This can be demonstrated more clearly in Figure 4-20(b); alloy D and alloy E are low-carbon Stellite alloys and Co solid solution proportion in these alloy is relatively large compared with the other alloys. At 90 degree impingement angle, high particle impact velocity expedited the impingement of the particles on the target surface and thus enhanced the strain hardening of the solid solution. The increased erosion resistance of the solid solution would contribute to the increase in the overall erosion resistance of the alloy.

6.2.2 Erosion resistance versus hardness

Hardness is used quite often in the field of wear resistance as a qualitative indicator for judging alloys, coatings, hardfacings and overlays [[4],[10],[39]]. It is generally accepted that the harder the material, the greater the wear resistance, for most materials [4]. In sliding wear hardness plays a predominant role in controlling the wear resistance of Stellite alloys at room temperature [52]. However, this hardness effect does not apply entirely for erosive wear. Relating the erosion rate data in Figure 4-15 to Figure 4-18 to the hardness data in Table 6-1, it was found that in a general trend the erosion resistance of Stellite alloys increased with hardness, but other factors may also play an important role. For example, as shown in Table 6-1, alloy B is the hardest among the alloys discussed and alloy D is harder than alloy C, but alloy B exhibited higher erosion rate than alloy A and alloy D exhibited higher erosion rate than alloy C. This abnormal effect can be more obviously observed in the erosion test at 90 degree impingement angle and at 98 m/s sand velocity. In these cases, alloy B exhibited the highest erosion rate and alloy D is the next highest. To explore the erosion mechanism of these alloys, one may consult their microstructures again. As discussed in Chapter 3, in addition to Cr_7C_3 carbide, there is also a large amount of $(\text{W},\text{Co})_6\text{C}$ carbide in alloy B due to its high W content, which increases the hardness of this alloy. Similarly, although alloy D has much lower C content than alloy C, this alloy contains a large amount of Co_3Mo and CoMo_6 intermetallic compound, which are hard and brittle. Considering the erosion process, as the hard sand particles impacted on the target surface, they cut and deformed the material, forming overhanging lips in the surface, as seen in the SEM images of the eroded surfaces in Chapter 4. Since alloy B and alloy D are harder, the

cutting of them by the sand particles was more difficult, thus the overhanging lips formed in their surfaces would be smaller in size. Under continuous impact of the particles, these lips were more easily broken down because of the small size and brittleness, especially at 90 degree impingement angle and at 98 m/s sand velocity. Normal impact and intense impingement of the particles on the surface aggravated the breaking of the lips, adding to the erosion loss. This characteristic of erosion damage can be observed in the eroded surface in Figure 4-27. On the other hand, the higher hardness of alloy B and alloy D is attributed to the large amounts of carbides and intermetallic compounds in their microstructures, which make them more brittle and more vulnerable under the continuous particle impact.

In summary, although hardness is known as a major factor that governs the wear resistance of materials, it is definitely not the unique factor that determines the erosion performance. Extensive studies have been reported in literature showing that erosion is essentially a complicated process involving multiple factors and these factors may all affect the erosion of a material differently [15]. As observed on the experimental results in the present research, the sequence of the hardness values does not correspond to the trend of the erosion rate. This reconfirms the conclusion by other investigators that material hardness is not the unique controlling factor in erosion damage of materials [15].

6.3 Modeling of Erosion

6.3.1 Error analysis of the modified S-K model

The S-K model developed by Sheldon and Kanhere [6] considers single particle impact on a 6061-TO aluminum surface. However, it has been proven to be applicable for

multiple particle impact on a Stellite alloy surface after a certain modification. The significant deficiency of the S-K model is the lack of particle impingement angle [6], while this factor definitely affects the erosion rate, as demonstrated by the erosion tests in the present research. After an extensive investigation in different mathematical functions, the functions given by equations (36) and (37) were selected to be incorporated in the S-K model thus accounting for the impingement angle, which introduced one other variable (impingement angle, α) and two coefficients, a and b , in the new equation (39). As described in Chapter 5, the coefficients a and b can be determined by fitting the experimental data of erosion rate to equation (39). The strategy of this fitting was in two aspects: (1) Find the values of a and b which best fit the experimental erosion rate for a given Stellite alloy tested at a given particle impact velocity. (2) These values of a and b must be invariant with the two impingement angles 30 degree and 90 degree used in the erosion tests.

In the iteration process using MATLAB, the percent error, ε , for the erosion rate was calculated as follows;

$$\varepsilon (\%) = \frac{|P - T|}{T} * 100 \quad (38)$$

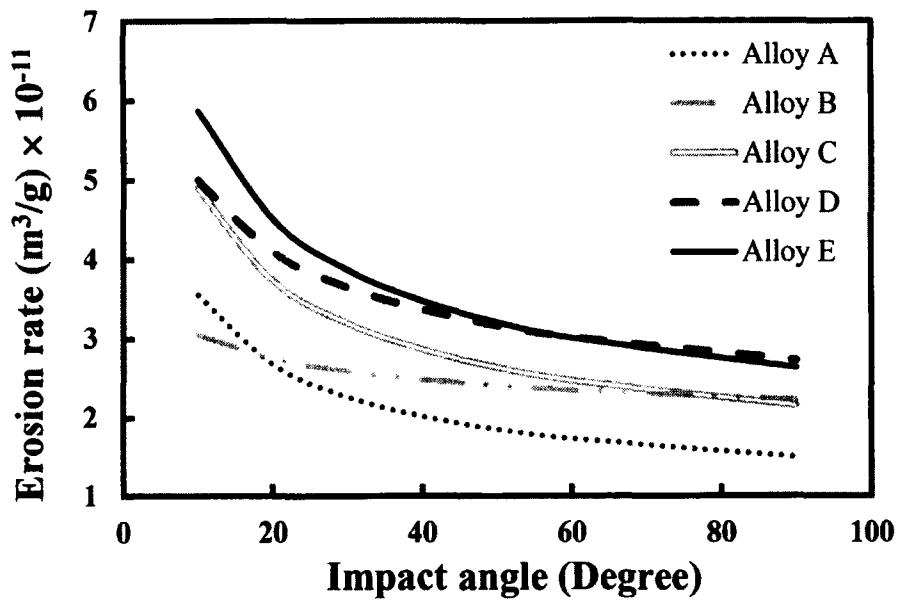
where P is the predicted value; and T is the experimental or the true value. For most engineering applications, a 5% error is generally acceptable, that is, working within a 95% confidence interval [7]. The final errors, ε , achieved in determining the values of a and b for all the five Stellite alloys in the two particle impact velocity cases, are presented in Table 6-2. It is shown that all the errors are within the set error limit of 5%.

Table 6-2: Error analysis for the modified S-K model

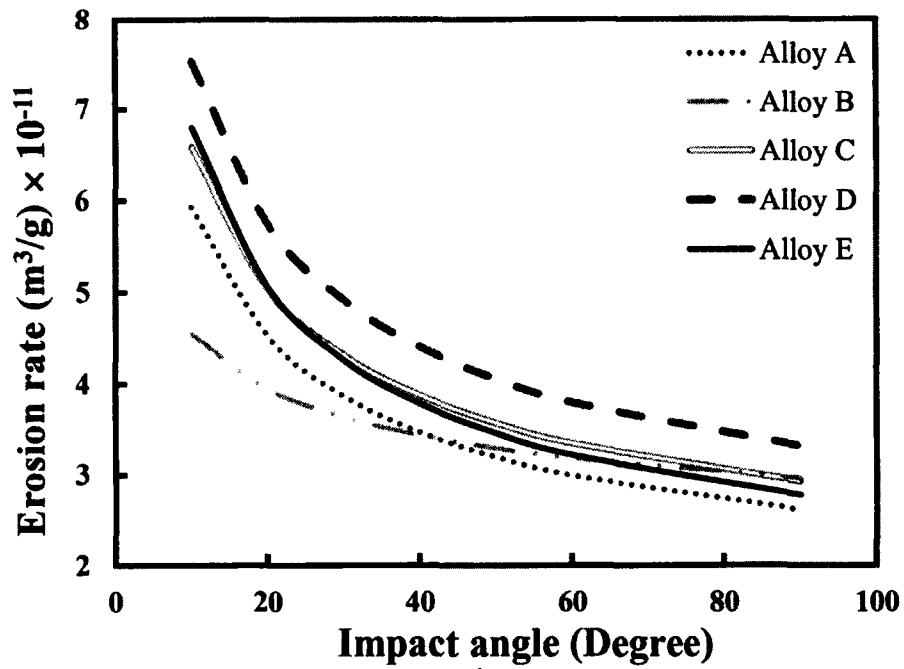
Particle impact velocity of 84 m/s						
	30 Degree			90 Degree		
Alloy	Experimental Value (m ³ /g) × 10 ⁻¹¹	S-K model Value (m ³ /g) × 10 ⁻¹¹	% Error ε	Experimental Value (m ³ /g) × 10 ⁻¹¹	S-K model Value (m ³ /g) × 10 ⁻¹¹	% Error ε
Alloy A	2.38	2.27	4.8126	1.43	1.50	4.8215
Alloy B	2.54	2.59	2.1331	2.14	2.23	4.2087
Alloy C	3.18	3.20	0.4397	2.07	2.16	4.052
Alloy D	3.49	3.65	4.6805	2.86	2.73	4.5382
Alloy E	3.96	3.87	2.4121	2.54	2.63	3.734
Particle impact velocity of 98 m/s						
Alloy A	3.88	3.87	0.0842	2.62	2.62	0
Alloy B	3.58	3.64	1.6837	3.06	2.97	2.8992
Alloy C	4.34	4.32	0.5004	2.98	2.93	1.5745
Alloy D	5.04	4.92	2.4626	3.21	3.32	3.2189
Alloy E	4.48	4.27	4.7662	2.65	2.78	4.5964

6.3.2 Prediction of erosion rate

In order to further test and understand the modified S-K model, for the five Stellite alloys, at the particle impact velocities of 84 m/s and 98 m/s, respectively, the erosion rates at various particle impingement angles between 10 to 90 degrees were predicted using the modified S-K model; the results are illustrated in Figure 6-1.



(a)



(b)

Figure 6-1: Predicted erosion rates using the modified S-K model; (a) at 84 m/s particle impact velocity and (b) at 98 m/s particle impact velocity.

It is shown that for the two particle impact velocities, the erosion rates of all the alloys decreased with the impingement angle. However, according to the experimental findings of previous studies [7], these alloys should behave differently at particle impingement angles smaller and larger than the “critical impingement angle” that may be around 30 degree. As described in Figure 2-2, for metallic materials, at small impingement angles, erosion rate increases with the increase in impingement angle until the angle reaches the “critical impingement angle” and thereafter the erosion rate decreases with impingement angle [7]. The deviation of the predicted erosion rates from the experimental observation is caused by the fact that the modified S-K model was developed by fitting the experimental data at 30 degree impingement angle and 90 degree impingement angle using a statistics method. Therefore, this model has a deficiency in predicting the erosion rate of Stellite alloys at impingement angles less than 30 degree. In particular, the erosion behaviour of these alloys changes significantly at impingement angles around 30 degree.

6.3.3 Experimental errors

As discussed above, the modified S-K model was developed based on the experimental erosion data of this research. However, as often encountered in all experiments, errors are unavoidable. In the present erosion test, for each testing condition, at least five data points were obtained, as shown in the tables in the Appendix. The values used in the modified S-K model are the averages of the erosion rates obtained in each testing condition. Definitely, these averages would vary with the number of specimens tested, and the change of the averages would affect the values of the

coefficients a and b in the modified S-K model. Therefore, the erosion rates predicted by the modified S-K model depend on the accuracy of the erosion experiments from which the erosion rates were obtained for determination of the coefficients a and b . There could be many error sources involved in the data collection. Some of these include systematic error; measurement error; human error, etc.

7 Chapter: Conclusions and Further Work

7.1 Conclusions

Five Stellite alloys were selected to investigate their solid-particle erosion behavior in this research. These alloys are currently employed or are potential materials for erosion resistance applications. They contain carbon varying between 0.25 ~ 1.6 wt%, that is, they are classified into low-carbon, and medium-carbon Stellite alloys. For the main alloying element, chromium, these alloys have a content between 22 ~ 30 wt%. For the other two important alloying elements, they have a tungsten content between 0 ~ 32 wt% and molybdenum content between 0 ~ 11.8 wt%. The hardness and erosion resistance under solid-particle impact of these alloys was investigated at room temperature and a modified erosion model that can approximately predict the erosion rate of Stellite alloys at particle impingement angles between 30 degree and 90 degree for a given particle impact velocity, was developed. The relationships between chemical composition, microstructure, hardness and erosion resistance of these alloys were discussed. The damage mechanisms of Stellite alloys under solid-particle erosion were studied, incorporating the analysis of eroded surfaces using SEM. The error analysis of the modified erosion model was made and the limitation of the model was further explained. In summary, the following conclusions can be derived from this research:

1. The carbon content of Stellite alloys is one of the main parameters controlling their erosion resistance. Carbon is a very important element, making the carbide volume fraction in Stellite alloys a critical parameter. Tungsten and molybdenum enhance the strength of Stellite alloys. When these alloying elements are present in large

quantities, they participate in the formation of carbides and intermetallics respectively.

Increase of both tungsten content and molybdenum content enhances the performance of Stellite alloys in erosive environments.

2. The damage of Stellite alloys under solid-particle erosion involves two mechanisms. One is the cutting of the material, which causes overhanging lips; and the other is the plastic deformation of the materials, which results in the removal of the surface layer as proposed by Bitter (1963). At 30 degree impingement angle, the material damage is mainly controlled by the tensile plastic deformation of the sub-surface layer due to the shearing effect, while at 90 degree impingement angle, the material damage is mostly caused by concentrated compressive stress induced in the surface layer due to the normal impact load.
3. The erosion rates of Stellite alloys at the impingement angle of 30 degree were higher than those at the impingement angle of 90 degree, because Stellite alloys have higher compressive strength than tensile strength. Also, the erosion rate of Stellite alloys increased with the particle impact velocity.
4. The hardness of Stellite alloys plays an important role in affecting their erosion resistance. In general, the alloy that is harder would be more erosion resistant. However, abnormal effect of hardness on the erosion resistance of Stellite alloys was observed. Since the harder surface is more resistant to deformation and cutting, the size of the overhanging lips formed in the surface would be smaller, therefore, they are more vulnerable under continuous particle impact. On the other hand, harder Stellite alloys normally contain a larger volume fraction of carbides or/and intermetallics, which make them more brittle. Under continuous particle impact in the erosion

process, in particular, at 90 degree impingement angle and at higher particle impact velocity, the surface was less resistant to concentrated compressive stress, leading to more cracking and fracture.

5. An erosion model, known as S-K model, originally developed by Sheldon and Kanhere (1972) for both single-particle erosion and multiple-particle erosion has been modified and then supported with testing data. The significant contribution of the present research to the improvement on the S-K model is that the modified S-K model has taken into account the effect of particle impingement angle on the erosion rate by introducing a new angle variable, accompanied with two other coefficients.
6. The modified S-K model was finalized by determining the two coefficients by fitting the experimental erosion data. Using this modified S-K model, for the five Stellite alloys studied in this research, the erosion rates at particle impingement angles between 30 degree and 90 degree, at the two particle impact velocities can be approximately predicted. Since the two coefficients vary rarely within the five alloys and also with the particle impact velocity, for any new Stellite alloy having a similar chemical composition to one of the tested alloys, the erosion rates at particle impingement angles between 30 degree and 90 degree can be roughly estimated using this model at any sand impact velocity.
7. As the data used for fitting the modified S-K model were obtained from the erosion test at 30 degree and 90 degree impingement angles, this model has the limitation in predicting the erosion rates at particle impingement angles less than 30 degree. In addition, since the modified S-K model was obtained by fitting the experimental

erosion data, the accuracy of the erosion experiment affects directly the predicted value of the erosion rate using the model.

7.2 Future Work

1. In order to improve the modified S-K model, for a given Stellite alloy, erosion test will be conducted at more particle impingement angles, in particular, at the angles less than 30 degree, and at more particle impact velocities.
2. To verify the applicability of the modified S-K model, erosion test will be performed on more Stellite alloys that cover a wide range of chemical compositions.
3. Because of the concept of “critical impingement angle” encountered in the field of erosion, more erosion tests will be conducted on each Stellite alloy at varying particle impingement angles around 30 degree in order to find out the critical impingement angle.
4. Furthermore, temperature influences the performance of Stellite alloys significantly, therefore, the erosion behavior of Stellite alloys at elevated temperatures will be investigated.

References

- [1] J. R. Davis, "*Nickel, Cobalt, and Their Alloys*," ASM International, Materials Park, 2000, p 362-406.
- [2] W. Betteridge, "*Cobalt and Its Alloys*," Halsted Press, Chichester, 1982, p. 41-54.
- [3] M. F. Amateau, D. W. Nicholson and W. A. Glaeser, "*Survey of Materials for High-Temperature Bearing and Sliding Applications*," *Wear*, Vol. 7, 1964, p. 385-418.
- [4] C. Opris, R. Liu, M. Yao and X. Wu, "*Development of Stellite alloy composites with sintering/HIPing technique for wear-resistant applications*," *Materials and Design*, Vol. 28, 2007, p. 581-591.
- [5] J. W. Edington and I. G. Wright, "*Study of Particle Erosion Damage in Haynes Stellite 6B I: Scanning Electron Microscopy of eroded Surfaces*," *Wear*, Vol. 48, 1978, p. 131-144.
- [6] G. L. Sheldon and A. Kanhere, "*An Investigation of Impingement Erosion Using Sing Particles*," *Wear*, Vol. 21, 1972, p. 195-209.
- [7] S. Kamran, K. Chen, P. Patnaik, S. Yun and Y. Han, "*Current Status of Modeling Erosion and Erosion-Corrosion for Alloys and Protective Coatings*," NRC Protected A, Vol. II, 2011, LTR-SMPL-2010-0223.
- [8] Y. I. Oka, S. Mihara and T. Yoshida, "*Impact-Angle Dependence and Estimation of Erosion Damage to Ceramic Materials Caused by Solid Particle Impact*," *Wear*, Vol. 267, 2009, p. 129-135.
- [9] A. K. Cousens and I. M. Hutchings, "*Influence of Erodent Particle Shape on the Erosion of Mild Steel*," Proc. 6th Int. Conf. on Erosion by Liquid and Solid Impact

(Eds. Field J.E. and Corney N.S.) Cavendish Laboratory, Cambridge University, September 1983, Cambridge, UK.

- [10] A. V. Reddy and G. Sundararajan, "*Erosion Behavior of Ductile Materials with a Spherical Non-Friable erodent,*" *Wear*, Vol. 111, 1986, p. 313-323.
- [11] W. A. Glaeser, R. C. Erickson, K. F. Dufrane and J. W. Kannel, "Tribology: The Science of Combatting Wear," Battelle, Columbus, Ohio, 1994.
- [12] I. M. Hutchings, "*Mechanical and Metallurgical Aspects of the Erosion of Metals,*" Proc. Conf. on Corrosion/Erosion of Coal Conversion System Materials (Ed. Levy A.V.) NACE, Houston, 1979, p. 393.
- [13] G. Sundararajan and P. G. Shewmon, "*A New Model for the Erosion of Metals at Normal Incidence,*" *Wear*, Vol. 84, 1983, p. 257-258.
- [14] J. E. Goodwin, W. Sage and G. P. Tilly, "*Study of Erosion by Solid Particles,*" Proc. Inst. of Mech. Engg. (London), Vol. 184, 1969, p. 279-292.
- [15] G. Sundararajan and M. Roy, "*Review of Solid Particle Erosion Behaviour of Metallic Materials at Room and Elevated Temperatures,*" *Tribology International*, Vol. 30, No. 5, 1997, p. 339-359.
- [16] J. E. Montgomery and J.M. Clarke SAE Summer Meetings, New York, 1962, paper 538A.
- [17] C. D. Wood and P. W. Espenschade, "*Mechanisms of Dust Erosion,*" SAE Summer Meetings, New York, 1964, paper 880A.
- [18] G. L. Sheldon and I. Finnie, "*The Mechanism of Material Removal in The Erosive Cutting of Brittle Materials,*" *Trans. ASME*, Vol. 88B, 1966, p. 393-400.

- [19] M. Liebhard and A.V. Levy, "*The Effects of Erodent Particle Characteristics on the Erosion of Metals*," Proc. Int. Conf. on Wear of Materials, (Eds. Ludema K.C. and Bayer R.G.) ASME, 1991, p. 245.
- [20] A. V. Levy, "*Solid particle erosion and erosion-corrosion of Materials*," ASM International, Materials Park Ohio, USA, 1995.
- [21] M. Roy, Y. Tirupataiah and G. Sundararajan, "*The Effect of Particle Shape on the Erosion of Cu and its Alloys*," Material Science and Engineering, Vol. 165A, 1993, p. 51-63.
- [22] L. P. McCabe, G. Sargent and H. Conrad, "*Effect of Microstructure on the Erosion of Steel by Solid Particles*," Wear, Vol. 105, 1985, p. 257-277.
- [23] A. V. Levy, "*The Role of Plasticity in Erosion*," Proc. 5th Int. Conf. on Erosion by Liquid and Solid Impact, Cambridge, Cambs., Cavendish Laboratory, Cambridge University, September 1979, Cambridge, paper 39.
- [24] J. P. Tu, J. Pan, M. Matsumura and H. Fukunaga, "*The Solid Particle Erosion Behaviour of $Al_{18}B_4O_{33}$ Whisker-reinforced AC4C Al Alloy Matrix Composites*," Wear, Vol. 223, 1998, p. 22-30.
- [25] I. Finnie, "*Some Reflections on the Past and Future of Erosion*," Wear, Vol. 186-187, 1995, p. 1-10.
- [26] I. Finnie, "*Erosion of Surfaces by Solid Particles*," Wear, Vol. 3, 1960, p. 87-103.
- [27] I. Finnie, "*The Mechanism of Erosion in Ductile Materials*," Proc. of the Third US National Congress of Applied Mechanics, Hagthornthwaite, R.M., Ed., ASME, New York, 1958, p. 70-82.

- [28] G. P. Tilly, "*Sand Erosion of Metals and Plastics: A Brief Review*," *Wear*, Vol. 14, 1969, p. 241-248.
- [29] G. P. Tilly, "*A Two Stage Mechanism of Ductile Erosion*," *Wear*, Vol. 26, 1973, p. 87-96.
- [30] J. G. A. Bitter, "*A Study of Erosion Phenomena*," Part I and Part II, *Wear*, Vol. 6, 1963, p. 5-12 and p. 169-190.
- [31] J. H. Neilson and A. Gilchrist, "*Erosion by a Stream of Solid Particles*," *Wear*, Vol. 11, 1968a, p. 111-122.
- [32] I. M. Hutchings and R. E. Winter, "*Particle Erosion of Ductile Metals: A Mechanism of Material Removal*," *Wear*, Vol. 27, 1974, p. 121-128.
- [33] I. M. Hutchings, "*A Model for the Erosion of Metals by Spherical Particles at Normal Incidence*," *Wear*, Vol. 70, 1981, p. 269-281.
- [34] Y. I. Oka, K. Okamura and T. Yoshida, "*Practical Estimation of Erosion Damage Caused by Solid Particle Impact: Part 1: Effects of Impact Parameters on a Predictive Equation*," *Wear*, Vol. 259, p. 95-101.
- [35] G. Sundararajan, "*The Solid Particle Erosion of Metallic Materials: The Rationalization of the Influence of Material Variables*," *Wear*, Vol. 186-187, 1995, p. 129-144.
- [36] S. Abdelrahman and M. M. Stack, "*Some Reflections on a Model to Predict the Erosion Rate of the Passive Film on Pure Metals*," ASAT-13, 2009, ASAT-13-MS-16.

- [37] Y. Tirapataiah, B. Venkataraman and G. Sundararajan , "*The Nature of the Elastic Rebound of a Hard Ball Impacting on Ductile, Metallic Target Materials,*" *Material Science and Engineering: A*, Vol. 124(2), 1990, p. 133-140.
- [38] M. Roy, K. K. Ray and G. Sundararajan, "*An Analysis of the Transition from Metal Erosion to Oxide Erosion,*" *Wear*, Vol. 217(2), 1998, p. 312-320.
- [39] A. Frenk and J. D. Wagnière, "*Laser cladding with cobalt-based hardfacing,*" *J. Phys. IV France, 1(C7)*, 1991, p. 65-68.
- [40] C. J. Heathcock, A. Ball and B. E. Protheroe, "*Cavitation Erosion of Cobalt-based Stellite Alloys, Cemented Carbides and Surface-treated Low Alloy Steels,*" *Wear* 74(1), 1981, p. 11-26.
- [41] J. J. Kim, J. H. Jhung, S. J. Cho and K. J. Yoon, "*Solid Particle Erosion of Inconel 625 at Elevated Temperatures,*" *J. Mater. Sci. Lett.*, Vol. 19(9), 2000, 759.
- [42] S. Chinnadurai and S. Bahadur, "*High Temperature Erosion of Haynes and Waspaloy: Effect of Temperature and Erosion Mechanisms,*" *Wear*, Vol. 186-187(1), 1995, p. 299-305.
- [43] S. Majumdar and A. Sarajedini, "*Review of Solid Particle Erosion of Engineering Materials,*" American Society of Mechanical Engineers, Pressure Vessels and Piping Division (Publication) PVP, 139, 1988, p. 79.
- [44] M. Yan, Z. Fan and M. J. Bevis, "*The Erosion Behaviour of Inconel 718 in Molten A380 Alloy,*" *Scripta Materialia*, 40(11), 1999, p. 1255.
- [45] D. J. Stephenson, "*Predicting the High Temperature Erosion Behaviour of Materials used in Gas Turbines,*" *Corr. Sci.*, 29(6), 1989, p. 647.

- [46] P. K. Sapra, S. Singh and S. Prakash, "*Erosion-Corrosion Behaviour of Ni-based Superalloy Superni-600 in the Real Service Environment of the Boiler,*" *Inter. J. Micro. Mater. Proper.*, 5(6), 2010, p. 536.
- [47] W. Tabakoff, "*Erosion Resistance of Superalloys and Different Coatings Exposed to Particulate Flows at High Temperature,*" *Surf. Coat. Technol.*, 120-121, 1999, p. 542.
- [48] W. Tabakoff and V. Shanov, "*Erosion Rate Testing at High Temperature for Turbomachinery use,*" *Surf. Coat. Technol.*, 76-77(1), 1995, p. 75.
- [49] C. T. Kang, S. L. Chang, N. Birks and F. S. Pettit, "*Erosion-Corrosion of Coatings and Superalloys in High Velocity Hot Gases,*" *Transactions of the Japan Institute of Metals, Supplement*, 24, 1982, p. 87.
- [50] K. Natesan and Y. Y. Liu, "*Erosion-Corrosion of Materials at Elevated Temperatures,*" *Mater. Sci. Eng. A (Structural Materials: Properties, Microstructure and Processing)*, A120-121, 1989, p. 571.
- [51] G. P. Tilly and W. Sage, "*The Interaction of Particle and Material Behavior in Erosion Processes,*" *Wear*, Vol. 16, 1970, p. 447-465.
- [52] S. Kapoor, "*High-Temperature Hardness and Tribological Properties of Stellite Alloys,*" Master's Thesis, Department of Mechanical & Aerospace Engineering, Carleton University, 2011.

Appendix: Experimental Data Sheets

Table A- 1: Test data at 84 m/s sand velocity for alloy A

Temperature 20°C	Velocity 84 m/s	Angle 30 deg	Nozzle Distance 5 mm	Erodent Particle (Al ₂ O ₃)	Test Duration 10 min		
Sample Number	Sand Mass	Sand Used	Sample Mass	Sample Mass	Vibrator Voltage	Powder Flow Rate	Erosion rate
	<i>W</i> (kg)	(g)	<i>S</i> (g)	Loss (µg)	<i>V</i>	(g/min)	ER (µg/g)
3	34.896	11	49.66	2180.00	5.50	1.10	200
3	34.878	7	49.65	1280.00	5.50	0.70	180
3	34.866	12	49.65	2026.67	5.50	1.20	170
4	34.131	10	49.63	1760.00	4.50	1.00	180
4	34.111	11	49.62	2220.00	4.50	1.10	200
4	34.099	12	49.62	3240.00	4.50	1.20	270
Average		11		2117.78		1.1	200
STD DEVIATION		1.9		649.90		0.19	37
Temperature 20°C	Velocity 84 m/s	Angle 90 deg	Nozzle Distance 5 mm	Erodent Particle (Al ₂ O ₃)	Test Duration 10 min		
Sample Number	Sand Mass	Sand Used	Sample Mass	Sample Mass	Vibrator Voltage	Powder Flow Rate	Erosion rate
	<i>W</i> (kg)	(g)	<i>S</i> (g)	Loss (µg)	<i>V</i>	(g/min)	ER (µg/g)
2	34.384	6	49.65	486.67	5.50	0.60	81
2	34.38	4	49.65	440.00	5.50	0.40	110
2	34.373	7	49.65	806.67	5.50	0.70	120
2	34.366	7	49.64	1026.67	5.50	0.70	150
6	34.358	11	49.62	1600.00	4.50	1.10	150
Average		7		872.00		0.70	120
STD DEVIATION		2.6		472.57		0.25	27

Table A- 2: Test data at 98 m/s sand velocity for alloy A

Temperature 20°C	Velocity 98 m/s	Angle 30 deg	Nozzle Distance 5 mm	Erodent Particle (Al ₂ O ₃)	Test Duration 10 min		
Sample Number	Sand Mass	Sand Used	Sample Mass	Sample Mass	Vibrator Voltage	Powder Flow Rate	Erosion rate
	<i>W</i> (kg)	(g)	<i>S</i> (g)	Loss (µg)	<i>V</i>	(g/min)	ER (µg/g)
3	34.666	12	49.65	3146.67	3.75	1.20	260
3	34.644	15	49.64	4186.67	3.75	1.50	280
4	34.184	10	49.64	3880.00	4.50	1.00	390
4	34.194	11	49.64	3913.33	4.50	1.10	360
4	34.168	16	49.63	4266.67	4.50	1.60	270
7	34.164	11	49.66	4393.33	4.50	1.10	400
Average		13		3964.44		1.3	330
STD DEVIATION		2.4		447.92		0.24	63
Temperature 20°C	Velocity 98 m/s	Angle 90 deg	Nozzle Distance 5 mm	Erodent Particle (Al ₂ O ₃)	Test Duration 10 min		
Sample Number	Sand Mass	Sand Used	Sample Mass	Sample Mass	Vibrator Voltage	Powder Flow Rate	Erosion rate
	<i>W</i> (kg)	(g)	<i>S</i> (g)	Loss (µg)	<i>V</i>	(g/min)	ER (µg/g)
2	34.299	5	49.64	1060.00	5.50	0.50	210
2	34.279	9	49.63	1600.00	5.50	0.90	180
2	34.26	19	49.63	3773.33	5.50	1.90	200
5	34.635	12	49.64	2793.33	4.50	1.20	230
5	34.625	10	49.64	2826.67	4.50	1.00	280
6	34.409	10	49.62	2146.67	4.50	1.00	220
Average		11		2366.67		1.1	220
STD DEVIATION		4.6		971.18		0.46	36

Table A- 3: Test data at 84 m/s sand velocity for alloy B

Temperature 20°C	Velocity 84 m/s	Angle 30 deg	Nozzle Distance 5 mm	Erodent Particle (Al ₂ O ₃)	Test Duration 10 min		
Sample Number	Sand Mass	Sand Used	Sample Mass	Sample Mass	Vibrator Voltage	Powder Flow Rate	Erosion rate
	<i>W</i> (kg)	(g)	<i>S</i> (g)	Loss (μg)	<i>V</i>	(g/min)	ER (μg/g)
2	34.027	8	77.03	1650.00	4.75	0.80	200
2	34.016	11	77.02	3116.67	4.75	1.10	280
2	34.006	10	77.02	2516.67	4.75	1.00	250
3	34.588	12	78.28	3133.33	4.75	1.20	260
3	34.571	17	78.28	3450.00	4.75	1.70	200
3	34.562	9	78.28	2333.33	4.75	0.90	260
6	34.328	11	76.98	2866.67	4.50	1.10	260
Average		11		2723.81		1.11	240
STD DEVIATION		2.9		608.04		0.29	30
Temperature 20°C	Velocity 84 m/s	Angle 90 deg	Nozzle Distance 5 mm	Erodent Particle (Al ₂ O ₃)	Test Duration 10 min		
Sample Number	Sand Mass	Sand Used	Sample Mass	Sample Mass	Vibrator Voltage	Powder Flow Rate	Erosion rate
	<i>W</i> (kg)	(g)	<i>S</i> (g)	Loss (μg)	<i>V</i>	(g/min)	ER (μg/g)
1	34.257	3	75.53	800.00	5.50	0.30	270
1	34.251	6	75.53	1233.33	5.50	0.60	200
4	34.604	9	78.02	1833.33	4.50	0.90	200
4	34.594	10	78.02	1783.33	4.50	1.00	180
4	34.585	9	78.02	2166.67	4.50	0.90	240
4	34.572	13	78.01	2250.00	4.50	1.30	170
5	34.397	12	77.67	2233.33	4.50	1.20	190
Average		8.9		1757.14		0.89	210
STD DEVIATION		3.4		552.93		0.34	34

Table A- 4: Test data at 98 m/s sand velocity for alloy B

Temperature 20°C	Velocity 98 m/s	Angle 30 deg	Nozzle Distance 5 mm	Erodent Particle (Al ₂ O ₃)	Test Duration 10 min		
Sample Number	Sand Mass	Sand Used	Sample Mass	Sample Mass	Vibrator Voltage	Powder Flow Rate	Erosion rate
	<i>W</i> (kg)	(g)	<i>S</i> (g)	Loss (μg)	<i>V</i>	(g/min)	ER (μg/g)
2	34.715	13	77.01	4100.00	3.75	1.30	320
3	34.382	14	78.27	4850.00	4.50	1.40	350
3	34.368	14	78.27	4200.00	4.50	1.40	300
3	34.357	11	78.26	4016.67	4.50	1.10	370
3	34.343	14	78.26	5116.67	4.50	1.40	370
6	34.209	11	76.97	4366.67	4.50	1.10	400
Average		13		4441.67		1.3	350
STD DEVIATION		1.5		443.57		0.15	36
Temperature 20°C	Velocity 98 m/s	Angle 90 deg	Nozzle Distance 5 mm	Erodent Particle (Al ₂ O ₃)	Test Duration 10 min		
Sample Number	Sand Mass	Sand Used	Sample Mass	Sample Mass	Vibrator Voltage	Powder Flow Rate	Erosion rate
	<i>W</i> (kg)	(g)	<i>S</i> (g)	Loss (μg)	<i>V</i>	(g/min)	ER (μg/g)
4	34.852	8	78.03	1966.67	5.50	0.80	250
1	34.497	7	75.49	2416.67	5.00	0.70	350
1	34.509	7	75.50	1816.67	5.00	0.70	260
4	34.83	11	78.03	3833.33	5.50	1.10	350
1	34.516	11	75.50	2500.00	5.00	1.10	230
5	34.43	11	77.68	3916.67	4.50	1.10	360
Average		9.2		2741.67		0.92	300
STD DEVIATION		2.0		915.71		0.20	59

Table A- 5: Test data at 84 m/s sand velocity for alloy C

Temperature 20°C	Velocity 84 m/s	Angle 30 deg	Nozzle Distance 5 mm	Erodent Particle (Al ₂ O ₃)	Test Duration 10 min		
Sample Number	Sand Mass	Sand Used	Sample Mass	Sample Mass	Vibrator Voltage	Powder Flow Rate	Erosion rate
	<i>W</i> (kg)	(g)	<i>S</i> (g)	Loss (μg)	<i>V</i>	(g/min)	ER (μg/g)
4	34.986	10	68.27	2650.00	5.00	1.00	270
4	34.961	10	68.26	2116.67	4.75	1.00	210
5	34.439	6	67.60	1733.33	4.75	0.60	290
5	34.422	9	67.60	2283.33	4.75	0.90	250
8	34.318	10	67.99	3150.00	4.50	1.00	320
Average		9		2386.67		0.90	270
STD DEVIATION		1.7		539.08		0.17	39
Temperature 20°C	Velocity 84 m/s	Angle 90 deg	Nozzle Distance 5 mm	Erodent Particle (Al ₂ O ₃)	Test Duration 10 min		
Sample Number	Sand Mass	Sand Used	Sample Mass	Sample Mass	Vibrator Voltage	Powder Flow Rate	Erosion rate
	<i>W</i> (kg)	(g)	<i>S</i> (g)	Loss (μg)	<i>V</i>	(g/min)	ER (μg/g)
1	33.961	11	68.32	1700.00	5.00	1.10	160
1	35.242	5	68.31	1133.33	5.00	0.50	230
6	34.561	11	67.96	1450.00	4.50	1.10	130
6	34.551	10	67.96	1883.33	4.50	1.00	190
6	34.539	12	67.95	1983.33	4.50	1.20	170
6	34.53	9	67.95	1583.33	5.00	0.90	180
Average		9.7		1622.22		0.97	180
STD DEVIATION		2.5		308.16		0.25	32

Table A- 6: Test data at 98 m/s sand velocity for alloy C

Temperature 20°C	Velocity 98 m/s	Angle 30 deg	Nozzle Distance 5 mm	Erodent Particle (Al ₂ O ₃)	Test Duration 10 min		
Sample Number	Sand Mass	Sand Used	Sample Mass	Sample Mass	Vibrator Voltage	Powder Flow Rate	Erosion rate
	<i>W</i> (kg)	(g)	<i>S</i> (g)	Loss (µg)	<i>V</i>	(g/min)	ER (µg/g)
4	34.71	5	68.26	1850.00	3.75	0.50	370
4	34.687	10	68.26	3133.33	3.75	1.00	310
4	34.678	9	68.25	2716.67	3.75	0.90	300
5	34.229	11	67.59	4450.00	4.00	1.10	410
5	34.218	11	67.58	4333.33	3.75	1.10	390
5	34.205	13	67.58	4666.67	3.75	1.30	360
8	34.175	11	67.99	4483.33	3.75	1.10	410
Average		10		3661.90		1.00	360
STD DEVIATION		2.5		1096.36		0.25	43
Temperature 20°C	Velocity 98 m/s	Angle 90 deg	Nozzle Distance 5 mm	Erodent Particle (Al ₂ O ₃)	Test Duration 10 min		
Sample Number	Sand Mass	Sand Used	Sample Mass	Sample Mass	Vibrator Voltage	Powder Flow Rate	Erosion rate
	<i>W</i> (kg)	(g)	<i>S</i> (g)	Loss (µg)	<i>V</i>	(g/min)	ER (µg/g)
6	34.699	10	67.97	2050.00	4.90	1.00	210
6	34.687	12	67.96	2700.00	4.90	1.20	230
6	34.679	8	67.96	2383.33	4.90	0.80	300
6	34.67	9	67.96	2366.67	4.75	0.90	260
7	34.419	11	67.95	2833.33	4.90	1.10	260
Average		10		2466.67		1.00	250
STD DEVIATION		1.6		308.00		0.16	36

Table A- 7: Test data at 84 m/s sand velocity for alloy D

Temperature 20°C	Velocity 84 m/s	Angle 30 deg	Nozzle Distance 5 mm	Erodent Particle (Al ₂ O ₃)	Test Duration 10 min		
Sample Number	Sand Mass	Sand Used	Sample Mass	Sample Mass	Vibrator Voltage	Powder Flow Rate	Erosion rate
	<i>W</i> (kg)	(g)	<i>S</i> (g)	Loss (µg)	<i>V</i>	(g/min)	ER (µg/g)
3	34.952	9	75.85	2783.33	4.75	0.90	310
3	34.942	10	75.84	2650.00	4.60	1.00	270
3	34.907	4	75.84	1016.67	4.50	0.40	250
4	34.543	9	75.73	2283.33	4.50	0.90	250
4	34.522	10	75.72	3250.00	4.50	1.00	330
8	34.349	9	66.97	3150.00	4.50	0.90	350
Average		8.5		2522.22		0.85	290
STD DEVIATION		2.3		816.34		0.23	41
Temperature 20°C	Velocity 84 m/s	Angle 90 deg	Nozzle Distance 5 mm	Erodent Particle (Al ₂ O ₃)	Test Duration 10 min		
Sample Number	Sand Mass	Sand Used	Sample Mass	Sample Mass	Vibrator Voltage	Powder Flow Rate	Erosion rate
	<i>W</i> (kg)	(g)	<i>S</i> (g)	Loss (µg)	<i>V</i>	(g/min)	ER (µg/g)
1	34.326	9	75.66	2300.00	5.50	0.90	260
1	34.316	10	75.65	2166.67	5.50	1.00	220
1	34.308	8	75.65	2216.67	5.40	0.80	280
1	34.3	8	75.65	2316.67	5.40	0.80	290
7	34.387	10	65.24	1616.67	4.50	1.00	160
Average		9		2123.33		0.90	240
STD DEVIATION		1.0		289.78		0.10	52

Table A- 8: Test data at 98 m/s sand velocity for alloy D

Temperature 20°C	Velocity 98 m/s	Angle 30 deg	Nozzle Distance 5 mm	Erodent Particle (Al ₂ O ₃)	Test Duration 10 min		
Sample Number	Sand Mass	Sand Used	Sample Mass	Sample Mass	Vibrator Voltage	Powder Flow Rate	Erosion rate
	<i>W</i> (kg)	(g)	<i>S</i> (g)	Loss (µg)	<i>V</i>	(g/min)	ER (µg/g)
4	34.283	12	75.72	4883.33	4.50	1.20	410
4	34.273	10	75.71	4783.33	4.50	1.00	480
9	34.297	11	65.78	4916.67	4.50	1.10	450
9	34.254	10	65.77	3966.67	4.50	1.00	400
9	34.229	12	65.77	4933.33	4.50	1.20	410
8	34.197	12	66.96	4816.67	4.50	1.20	400
Average		11		4716.67		1.1	430
STD DEVIATION		1.0		371.93		0.10	32
Temperature 20°C	Velocity 98 m/s	Angle 90 deg	Nozzle Distance 5 mm	Erodent Particle (Al ₂ O ₃)	Test Duration 10 min		
Sample Number	Sand Mass	Sand Used	Sample Mass	Sample Mass	Vibrator Voltage	Powder Flow Rate	Erosion rate
	<i>W</i> (kg)	(g)	<i>S</i> (g)	Loss (µg)	<i>V</i>	(g/min)	ER (µg/g)
5	34.807	12	67.06	2916.67	5.50	1.20	240
5	34.796	11	67.06	2883.33	5.00	1.10	260
5	34.784	12	67.06	3083.33	5.25	1.20	260
5	34.773	11	67.06	3466.67	5.25	1.10	320
7	34.454	11	65.24	3000.00	4.50	1.10	270
Average		11		3070.00		1.1	270
STD DEVIATION		0.55		234.93		0.05	27

Table A- 9: Test data at 84 m/s sand velocity for alloy E

Temperature 20°C	Velocity 84 m/s	Angle 30 deg	Nozzle Distance 5 mm	Erodent Particle (Al ₂ O ₃)	Test Duration 10 min		
Sample Number	Sand Mass	Sand Used	Sample Mass	Sample Mass	Vibrator Voltage	Powder Flow Rate	Erosion rate
	<i>W</i> (kg)	(g)	<i>S</i> (g)	Loss (μg)	<i>V</i>	(g/min)	ER (μg/g)
2	35.059	7	63.24	2166.67	4.00	0.70	310
2	35.052	7	63.24	2700.00	3.75	0.70	390
3	34.488	11	62.29	3366.67	4.50	1.10	310
3	34.464	10	62.29	3316.67	4.50	1.00	330
3	34.458	6	62.29	2100.00	4.50	0.60	350
6	34.339	10	61.62	3200.00	4.50	1.00	320
Average		8.5		2808.33		0.85	330
STD DEVIATION		2.1		574.24		0.21	30
Temperature 20°C	Velocity 84 m/s	Angle 90 deg	Nozzle Distance 5 mm	Erodent Particle (Al ₂ O ₃)	Test Duration 10 min		
Sample Number	Sand Mass	Sand Used	Sample Mass	Sample Mass	Vibrator Voltage	Powder Flow Rate	Erosion rate
	<i>W</i> (kg)	(g)	<i>S</i> (g)	Loss (μg)	<i>V</i>	(g/min)	ER (μg/g)
1	34.36	7	62.73	1733.33	5.00	0.70	250
1	34.352	8	62.73	1600.00	5.25	0.80	200
1	34.343	9	62.73	1833.33	5.25	0.90	200
1	34.335	8	62.72	1883.33	5.50	0.80	240
5	34.378	9	63.54	1633.33	4.50	0.90	180
Average		8.2		1736.67		0.82	210
STD DEVIATION		0.84		122.70		0.08	27

Table A- 10: Test data at 98 m/s sand velocity for alloy E

Temperature 20°C	Velocity 98 m/s	Angle 30 deg	Nozzle Distance 5 mm	Erodent Particle (Al ₂ O ₃)	Test Duration 10 min		
Sample Number	Sand Mass	Sand Used	Sample Mass	Sample Mass	Vibrator Voltage	Powder Flow Rate	Erosion rate
	<i>W</i> (kg)	(g)	<i>S</i> (g)	Loss (μg)	<i>V</i>	(g/min)	ER (μg/g)
3	34.33	13	62.28	4283.33	4.00	1.30	330
3	34.319	11	62.28	4666.67	3.75	1.10	420
3	34.307	12	62.27	3716.67	3.75	1.20	310
3	34.295	12	62.27	4483.33	3.75	1.20	370
7	34.286	11	63.13	4650.00	5.50	1.10	420
7	34.264	13	63.12	4600.00	5.00	1.30	350
7	34.241	13	63.12	4933.33	5.25	1.30	380
6	34.186	11	61.61	4683.33	4.00	1.10	430
Average		12		4502.08		1.20	380
STD DEVIATION		0.93		366.93		0.09	45
Temperature 20°C	Velocity 98 m/s	Angle 90 deg	Nozzle Distance 5 mm	Erodent Particle (Al ₂ O ₃)	Test Duration 10 min		
Sample Number	Sand Mass	Sand Used	Sample Mass	Sample Mass	Vibrator Voltage	Powder Flow Rate	Erosion rate
	<i>W</i> (kg)	(g)	<i>S</i> (g)	Loss (μg)	<i>V</i>	(g/min)	ER (μg/g)
1	34.19	7	62.70	1416.67	4.50	0.70	200
4	34.746	12	63.20	2400.00	5.00	1.20	200
4	34.736	10	63.19	2433.33	5.00	1.00	240
4	34.721	15	63.19	3033.33	4.75	1.50	200
4	34.709	12	63.19	3350.00	4.50	1.20	280
5	34.441	13	63.54	2783.33	4.50	1.30	210
Average		12		2569.44		1.2	230
STD DEVIATION		2.7		670.27		0.27	32